Development of a New Approach to Biophysical Separations Using Dielectrophoresis

by

Paul Vernon Jones

A Dissertation Presented in Partial Fulfillment
of the Requirements for the Degree
Doctor of Philosophy

Approved April 2015 by the
Graduate Supervisory Committee:

Mark Hayes, Chair
Alexandra Ros
Pierre Herckes

ARIZONA STATE UNIVERSITY

May 2015

ABSTRACT

Biological fluids contain information-rich mixtures of biochemicals and particles such as cells, proteins, and viruses. Selective and sensitive analysis of these fluids can enable clinicians to accurately diagnose a wide range of pathologies. Fluid samples such as these present an intriguing challenge to researchers; they are packed with potentially vital information, but notoriously difficult to analyze. Rapid and inexpensive analysis of blood and other bodily fluids is a topic gaining substantial attention in both science and medicine. Current limitations to many analyses include long culture times, expensive reagents, and the need for specialized laboratory facilities and personnel. Improving these tests and overcoming their limitations would allow faster and more widespread testing for disease and pathogens, potentially providing a significant advantage for healthcare in many settings.

Both gradient separation techniques and dielectrophoresis can solve some of the difficulties presented by complex biological samples, thanks to selective capture, isolation, and concentration of analytes. By merging dielectrophoresis with a gradient separation-based approach, gradient insulator dielectrophoresis (g-iDEP) promises benefits in the form of rapid and specific separation of extremely similar bioparticles. High-resolution capture can be achieved by exploiting variations in the characteristic physical properties of cells and other bioparticles.

Novel implementation and application of the technique has demonstrated the isolation and concentration of blood cells from a complex biological sample, differentiation of bacterial strains within a single species, and separation of antibiotic-resistant and antibiotic-susceptible bacteria. Furthermore, this approach allows

simultaneous concentration of analyte, facilitating detection and downstream analysis. A theoretical description of the resolving capabilities of g-iDEP was also developed. This theory explores the relationship between experimental parameters and resolution. Results indicate the possibility of differentiating particles with dielectrophoretic mobilities that differ by as little as one part in 10^8, or electrophoretic mobilities differing by as little as one part in 10^5. These results indicate the potential g-iDEP holds in terms of both separatory power and the possibility for diagnostic applications.

To my family, for making this possible

ACKNOWLEDGMENTS

I deeply appreciate the support and coaching of my advisor. Dr. Mark Hayes is not only a gifted scientist; he is a visionary, outdoorsman, philosopher, raconteur, and most importantly, a teacher. He challenged and encouraged me through a period of dynamic personal and intellectual development. I also appreciate the contributions of my supervisory committee members, Dr. Alexandra Ros and Dr. Pierre Herckes. Their time and attention have markedly improved the quality and coherence of my work.

How can one claim credit for an achievement when riding upon others' shoulders? I could not have completed this dissertation without a significant amount of help from many remarkable people. First, I am thankful for my beautiful and fantastic wife, who has supported me throughout this journey. I can't imagine a better companion. Over the years we have shared many adventures. I am thankful for my three boys. Without choice, they have endured years of paucity so I could tilt at academic windmills. Their enthusiasm and wonder have continually rekindled my own love for science. I owe my parents more than I can express—from them came every good thing with which I've somehow been instilled. My mother taught me the self-perpetuating joys of creating, learning, and exploring. My father introduced me to the wonders of the natural world. He taught me that science does not constrain the universe—instead it reveals a cosmos even more strange, complex, and illimitable than I ever imagined. I am grateful for my older brother, John. His intelligence and work ethic have always been inspiring. My sister, Leslie, has a special gift for kindness and good advice. Together, their friendship and support have been inspiring and invaluable. I am also thankful for my life-long friend

Mark Perkins, for acting as co-conspirator in many unforgettable adventures and expeditions.

I could not have successfully navigated graduate school without the help of many newfound friends. I have been fortunate to participate in a research group brimming with talented and caring people. Thanks to Dr. Sarah Staton, I lacked nothing in terms of guidance and instruction through the first two years of graduate school. Dr. Noah Weiss inspired me with his enthusiasm and astute questions, regardless of the subject. Dr. Josemar Castillo was a kindred spirit, who provided much-needed encouragement and positivity. Dr. Stacy Kenyon's friendship and encouragement helped pull me through the last few years of graduate school. Shannon Huey and Claire Crowther consistently provided invaluable assistance with research, brainstorming, and last-minute proof-reading. Thanks to Ryan Yanashima for many entertaining conversations and for her expertise in microfabrication. Paige Davis and Alexa DeMichele provided much-needed laboratory assistance and laughter. I would also like to thank my other collaborators for helping move this work forward, including Dr. Prasun Mahanti and LaKeta Kemp. Many others helped in significant ways, and deserve more credit than this space allows. These include all my other friends and family members, and other members of the Hayes Research Group. I would not be where I am today without help from all of these people.

I would like add special thanks to my dad for investing countless hours of scientific, linguistic, and mathematical expertise. His ready comprehension of the project and brilliant insights contributed significantly to the development of this work.

TABLE OF CONTENTS

Page

CHAPTER Page

Page

APPENDIX

LIST OF TABLES

LIST OF FIGURES

Figure Page

CHAPTER 1

INTRODUCTION

1.1 Ubiquity and value of bioparticles

Who has not paused at some point to watch the hypnotic whorl of dust through sunlight? Perhaps for some, those glittering flecks swirling through the air have birthed awareness that there are hidden parts of this world—things that we cannot see at first glance. The world is rife with microscopic biological material—cells and cell fragments, proteins and DNA—they suffuse the air and blanket every surface. They range in size from a few nanometers up to tens or hundreds of micrometers (Fig. 1.1). These particles offer a potential treasure-trove of information about us as well as our surroundings.

Consider, for a moment, the human body. Current estimates place the number of cells in a typical body around 30-40 trillion [1]. Most of these cells contain a galaxy of smaller particles: billions of proteins, an entire genome, and countless small molecules. A healthy circulatory system pumps trillions of blood cells through the body's vasculature each minute [2]. If it were possible to plumb the physical and chemical properties of even a single leukocyte, that little orb might betray all manner of secrets about its parent organism's health and history. Blood plasma also contains proteins, hormones, carbohydrates, and lipids, all of which fluctuate in response to diet, exercise, infection, and disease [3]. Also worthy of consideration are the myriad non-human hitchhikers that live and die upon the terrain of our bodies. The average human plays host to more than 10^{14} bacterial cells [4]. Partly because bacterial cells are much smaller than eukaryotes, they outnumber their host's human cells by a factor of ten to one. These cells comprise a

complex symbiotic ecosystem—a microbiological community where the population and demographics are tied inextricably with the health and habits of the human host [5-7].

The potential value of information presented by bioparticles is staggering. However, the complexity of the particles themselves, as well as the complexity of heterogeneous biological samples, present significant challenges [8]. States of disease and health in the parent organism may be linked to subtle, even molecular changes in target bioparticles. A target strain of bacteria may coexist in samples with thousands of other variants. The relative abundance of each variant within the sample may span many orders of magnitude. In these scenarios, separation of targets by traditional methods may be impossible.

How then, is an interested scientist or clinician to harvest these sheaves of cryptic particle-borne information? Unraveling complex biological systems and obtaining pertinent information depend upon the availability and use of specific and selective tools. Differentiation and isolation of specific analytes have long served as foundational goals of separation science and analytical chemistry. Much of the recent innovation in these fields is driven by a desire for rapid and specific analysis of complex biological samples. Traditional microbiological approaches often lack the specificity required for interrogating complex and heterogeneous samples [9]. Some clinical protocols may require multiple days for culturing, only to glean a meager positive or negative result to a narrow query. Some analytical approaches may offer more rapid results, but must often be performed upon already-pure or relatively homogeneous samples. These serve as just two examples of the many challenges faced by bioparticle analysis.

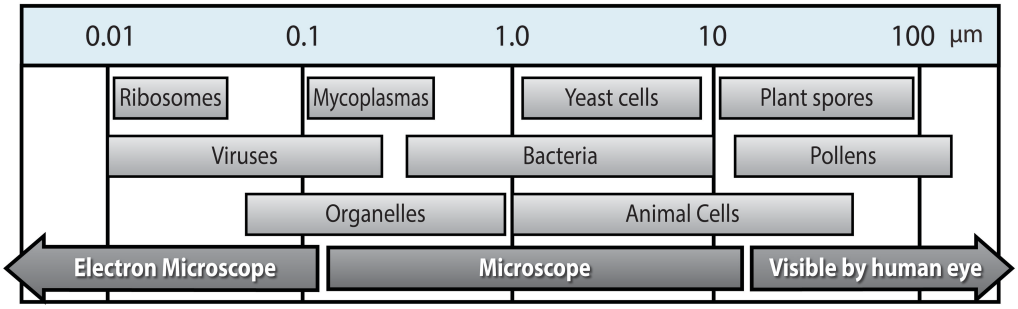

Figure 1.1. A comparison of the typical sizes of common biological particles. These sizes are compared to typical modes of particle visualization. Adapted with permission from reference [10].

1.2 Bioparticle analysis and clinical applications

Clinicians rely upon bioparticulate analysis for a wide array of medical tests: blood cell counts are used to diagnose infections and blood disorders; the presence of rare circulating proteins can indicate damage to the heart or other organs; wounds are swabbed and cultured to test for the presence of certain bacteria. Developments in modern healthcare technology have increasingly prioritized the growth of personalized medicine [11]. Both practitioners and patients prioritize individualized and data-driven diagnosis and treatment. The reliance upon and desire for information is on the rise. Bioanalytes represent a vital potential source of that information.

Some common procedures have persisted for decades, despite the emergence of newer rapid-analysis technologies. The peripheral blood smear and selective culturing serve as two examples of technologically archaic analytical tests which are still widely used. Traditional clinical tests such as these are hampered by the necessity of experienced technicians, long handling times, and the resulting impracticality of high-throughput testing. State-of-the-art diagnostics often involve instrumentation- and technology-heavy solutions, such as flow cytometry, rapid PCR variants, or mass spectrometry. Each of

these approaches may improve accuracy and throughput, but typically require sophisticated laboratory facilities, expensive equipment, and trained specialists. Furthermore, they often require the use of already pure, pre-cultured, or low-complexity samples. This requirement is at odds with the nature of most biological samples obtained by swabbing, aspirating, or phlebotomizing.

Many nascent bioanalytical technologies aim to improve upon existing methods by decreasing the steps required to obtain results, integrating multiple diagnostic tests, and enabling new clinical tests, all while simultaneously reducing costs and processing time, and increasing portability. Microfluidic and lab-on-a-chip devices offer the tantalizing possibility of comprehensive analysis performed at a patient's bedside.

1.3 Relevant classes of bioparticles and associated challenges

Proteins are the workhorses of molecular biology. Their presence within fluids or tissues can provide vital information about biological systems [12]. Proteins are polymeric macromolecules, typically composed of 20 to 20,000 amino acid monomers. Protein classes, functions, and roles are far too numerous to list here. The human genome encodes approximately 20,000 to 25,000 protein sequences [13]. But post-translational modifications, glycosylation, and protein folding increase the diversity and complexity of an organism's proteome by multiple orders of magnitude.

Viruses are small pathogens capable of replicating within the cells of a larger organism. Structurally, they consist of nucleic acid (either DNA or RNA) within a protein capsid and a lipid envelope. Viruses present an interesting analytical target due to their role in a multitude of diseases. Their occurrence within complex body fluids, as well as their potentially low abundance, presents significant challenges. Many analytical

approaches to virus detection utilize direct binding with antibodies in extremely sensitive immunoassays. While both sensitive and selective, immunoassay-based tactics are still limited by factors such as long analysis times, expensive reagents and equipment, and low throughput.

Cells are the smallest functional living units of biology. All cells can be grouped into two basic categories: prokaryotes and eukaryotes. These categories, however, are populated with uncounted varieties. Individual eukaryotic cells offer troves of information regarding their parent organism's genetics and epigenetics, biological processes, pathogenesis, and disease states. Prokaryotic cells (both commensal and pathogenic) can also offer important information about their host organism. The average human gut, for instance, contains 10^{14} prokaryotic cells, consisting of 500-1000 individual species and even more strains and varieties. Many may remain unidentified, resistant to laboratory culturing [14, 15].

Cell separation or differentiation according to unique phenotypes is fundamental to biology and medicine. Many clinical problems require isolation or identification of one cell type amongst a dense suspension of others.

The methods used for identification vary depending on both the nature of the sample and the desired outcome. Bulk techniques such as centrifugation and cell sorting are commonly used for basic diagnostics, sample preparation, or high-throughput applications.

1.4 An approach based on separation science

Fundamental to all analytical chemistry is the selective transport and redistribution of material through space [16]. Displacement is usually driven by a force or

gradient acting upon analyte. For example, applying an electric potential across space will propel charged particles through their surrounding medium. Centrifugation causes particles to sediment at different rates. Separation techniques vary widely in terms of both forces used and strategic implementation of those forces. The common thread is that the impelling forces behind transport exploit structural, electrical, and molecular differences among analytes to achieve separation and differentiation. The success of all such attempts depends upon the ability to selectively apply force to the analyte in question. A few of the properties commonly interrogated in this manner include size, mass, density, charge, and molecular interactions.

In some cases where the intrinsic properties of a particle are difficult to probe, chemical labels can be added and then exploited for analyte manipulation [17]. Such labels may include proteins, DNA or RNA, fluorophores, or chromophores. Multi-step techniques and superposed-force separations have opened additional doors to chemical and particle analysis. Introduction of new techniques and refinement of existing ones have enabled the manipulation and analysis of a staggering array of materials, with often mind-boggling selectivity. Differentiations of molecular enantiomers, protein isoforms, DNA molecules differing by a single base-pair, and different types of cells have all become relatively routine.

Despite all the progress, analytical separations still face limitations when the probing mechanisms are insufficiently selective, when labeling is insufficient or impractical, or when mixed samples contain interfering species or present insurmountably complex analyte matrices. Biological samples and those of natural origin are especially problematic.

1.5 Continuous, discontinuous, and steady-state separations

Past treatments of separation science have categorized separations as continuous, discontinuous, or steady-state/equilibrium gradients (Fig. 1.2) [16]. A continuous gradient separation scheme is characterized by uniform force-induced transport along the length of the separation apparatus. Both electrophoresis and chromatography are examples of this paradigm. Species are introduced to one end of a contained medium and travel in one direction. Separation occurs as a result of differing rates of transport through the field and medium. Discontinuous separation schemes are characterized by the presence of an immiscible multi-phase system, or a physical barrier such as a semi-permeable membrane. These barriers or membranes permit passage of certain chemical or particulate species, while impeding or halting others. Filtration, osmosis, and phasic extractions are examples of discontinuous separations. Lastly, steady-state or equilibrium gradient separations are characterized by force-displacement minima along the separatory axis. These minima cause analyte to collect in a particular region based on its characteristic properties. Included in this category are methods such as isoelectric focusing and isopycnic sedimentation.

With continuous separations, analyte undergoes unidirectional transport, driven by a spatially invariant force. In these cases, diffusion and other sources of dispersion usually contribute to continuous band-broadening, which dilutes analyte. Dispersive effects can compromise the detection and downstream analysis of bioanalytes, which are already low in abundance or co-occur with similar analytes. In comparison, steady-state separations produce a concentrating force that counterbalances dispersion. The forces acting upon analyte, and thus their resulting net velocity, vary across space, such that

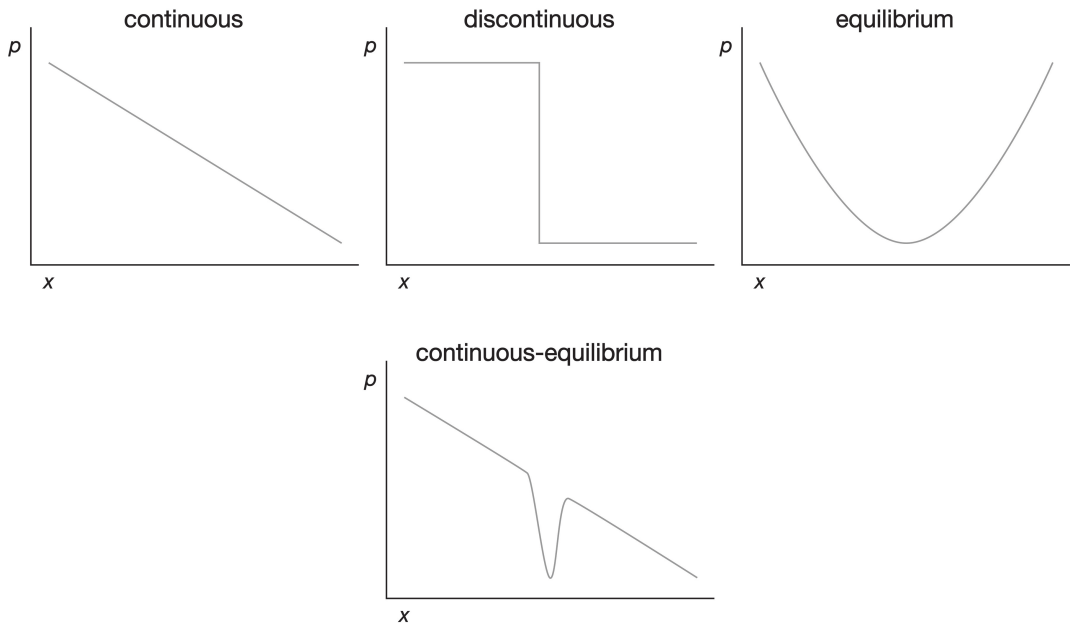

Figure 1.2. Plots showing potential energy (p) gradients for force-induced transport of analyte along a separatory axis (x). (Top) Three common categories include continuous, discontinuous, and equilibrium gradients. (Bottom) The work described within this dissertation explores a new category of separation profile, termed a continuous-equilibrium gradient.

a net zero velocity occurs in certain locations. In a traditional steady-state separation such as isoelectric focusing, analyte is transported to its distinct force minimum from all areas of the separation medium. This often results in simultaneous isolation and concentration of analyte above initial levels.

Presented and explored within this dissertation is a unique superposition of continuous and steady-state separations, achieved through the application of electrophoretic, electroosmotic, and dielectrophoretic forces within a microchannel. This approach uniquely combines advantages of both continuous and steady-state separation schemes. The ability to capture and concentrate analyte from a continuous flow of

particles offers distinct advantages when working with low-abundance bioanalytes and complex samples, particularly those of natural origin.

1.6 Electrokinetic forces and gradient insulator-based dielectrophoresis (g-iDEP)

This dissertation primarily focuses upon a unique and specific application of electrokinetic forces within a microfluidic channel. A brief introduction to these forces is provided here, but Chapter 2 offers more comprehensive detail.

For hundreds of years, scientists have avidly investigated the manipulation of small particles within aqueous media. Hydrodynamics, optics, electromagnetics, and even ultrasound have all been utilized for trapping and moving small particles and cells. Some of these approaches are old, and some are new, but all have been well trod.

Within the past sixty years, the unique and rather complicated phenomenon of dielectrophoresis (DEP) has emerged as an important electrokinetic force, capable of manipulating and controlling a wide array of particles and cells [18]. Dielectrophoretic force is produced when spatially inhomogeneous electric fields act upon permanent or field-induced dipoles. The force induced depends upon complex interacting variables, such as particle size, structure, and dielectric properties [19]. Even between similarly-sized particles these properties can vary dramatically. Dielectrophoresis can act upon charged and net-neutral species alike, and pairs easily with other electrokinetic forces such as electrophoresis (EP) and electroosmotic flow (EOF).

In a large part, the limited number of effective tools for manipulating bioparticles has driven the interest in DEP. New microfluidic strategies using DEP have created a crowded and burgeoning niche for environmental, biological, and medical applications of the technique [20-23]. Dielectrophoresis, applied on a microfluidic scale, presents unique

advantages over alternatives for particle manipulation. General advantages afforded by microfluidic platforms often include lower costs, rapid response times, compatibility with small sample sizes, and device portability.

Insulator-based dielectrophoresis (iDEP) represents a common microfluidic implementation of DEP forces. Insulating features create field non-uniformities that, in turn, induce DEP force. Various implementations of iDEP have been demonstrated, using features such as glass beads, curved or rectangular hurdles, serpentine channels and arrays of uniformly-sized geometric features within a channel [24-27]. Many applications of iDEP result in bifurcation of a sample population, based upon the particles' characteristic dielectrophoretic mobility (μ_{DEP}). Typically, particles with a μ_{DEP} greater than a certain cutoff value are trapped or diverted, while all those with a μ_{DEP} less than that cutoff pass the insulating features unhindered.

In 2007, Pysher and Hayes introduced a continuously tapered, sawtooth-edged microchannel [28]. Within this channel, aligned opposing teeth create a series of successively narrower gaps (hereafter referred to as gates) through which fluid and particles pass. Particles passing the sequentially narrower gates encounter increasing DEP force at each gate as they travel along the channel. Particles translate continuously along the channel, driven by EP and EOF, until reaching a gate that exerts sufficient DEP force to halt forward motion. This allows multiple types of particles to be isolated, concentrated, and resolved within the spatial domain of a single channel as well as the temporal domain of a single experimental run.

This work introduced a new type of analytical separation, which combines aspects of both continuous gradient and equilibrium gradient separation schemes. Since this new

category of iDEP microchannel uniquely fuses a separations-based approach to DEP-based analytics, it has been termed gradient insulator-based dielectrophoresis (g-iDEP).

1.7 Dissertation Objectives

This dissertation describes the development and application of g-iDEP microchannels as a tool for high-resolution bioparticle analysis. The unique combination and superposition of electrokinetic forces within g-iDEP microchannels creates a powerful platform for bioparticle analysis. The technique is capable of processing and interrogating a broad range of biological particles; theoretically ranging in size between a few tens of nanometers up to tens of micrometers in diameter. Falling within this range, and investigated in more detail within the body of this work, are human blood cells and various types of bacteria. The technique affords not only broad applicability, but also incredible specificity. Resolution of very similar analytes has proven possible, including differentiation of serotypes of *Escherichia coli*, and separation of gentamicin-resistant and gentamicin-susceptible variants of *Staphylococcus*.

1.8 References

[1] Bianconi, E., Piovesan, A., Facchin, F., Beraudi, A., Casadei, R., Frabetti, F., Vitale, L., Pelleri, M. C., Tassani, S., Piva, F., Perez-Amodio, S., Strippoli, P., Canaider, S., *Ann Hum Biol* 2013, *40*, 463-471.

[2] Sherwood, L., *Human Physiology: From Cells to Systems*, Cengage Learning 2008.

[3] Wintrobe, M. M., Greer, J. P., *Wintrobe's Clinical Hematology*, Wolters Kluwer Health/Lippincott Williams & Wilkins 2009.

[4] Hooper, L. V., Gordon, J. I., *Science* 2001, *292*, 1115-1118.

[5] Kau, A. L., Ahern, P. P., Griffin, N. W., Goodman, A. L., Gordon, J. I., *Nature* 2011, *474*, 327-336.

[6] Eloe-Fadrosh, E. A., Rasko, D. A., *Annual review of medicine* 2013, *64*, 145-163.

[7] Grice, E. A., Segre, J. A., *Nature reviews. Microbiology* 2011, *9*, 244-253.

[8] Toner, M., Irimia, D., *Annual Review of Biomedical Engineering* 2005, *7*, 77-103.

[9] Black, J. G., *Microbiology: principles and applications*, Prentice Hall 1996.

[10] Staton, S. J. R., Chen, K. P., Taylor, T. J., Pacheco, J. R., Hayes, M. A., *Electrophoresis* 2010, *31*, 3634-3641.

[11] Weston, A. D., Hood, L., *Journal of Proteome Research* 2004, *3*, 179-196.

[12] Anderson, N. L., Anderson, N. G., *Mol. Cell. Proteomics* 2002, *1*, 845-867.

[13] Collins, F. S., Lander, E. S., Rogers, J., Waterston, R. H., Int Human Genome Sequencing, C., *Nature* 2004, *431*, 931-945.

[14] Guarner, F., Malagelada, J. R., *Lancet* 2003, *361*, 512-519.

[15] Hooper, L. V., Gordon, J. I., *Science* 2001, *292*, 1115-1118.

[16] Giddings, J. C., *Unified Separation Science*, Wiley-Interscience 1991.

[17] Sameiro, M., Goncalves, T., *Chem. Rev.* 2009, *109*, 190-212.

[18] Pethig, R., *Biomicrofluidics* 2010, *4*.

[19] Pohl, H. A., *Dielectrophoresis: The Behavior of Neutral Matter in Nonuniform Electric Fields*, Cambridge University Press 1978.

[20] Gagnon, Z. R., *Electrophoresis* 2011, *32*, 2466-2487.

[21] Yang, L., *Analytical Letters* 2012.

[22] Srivastava, S. K., Gencoglu, A., Minerick, A. R., *Analytical and Bioanalytical Chemistry* 2011, *399*, 301-321.

[23] Çetin, B., Li, D., *Electrophoresis* 2011, *32*, 2410-2427.

[24] Suehiro, J., Zhou, G., Imamura, M., Hara, M., *Ieee Transactions on Industry Applications* 2003, pp. 1514-1521.

[25] Ying, L., White, S., Bruckbauer, A., Meadows, L., Korchev, Y., Klenerman, D., *Biophysical Journal* 2004, *86*, 1018-1027.

[26] Kang, Y., Li, D., Kalams, S. A., Eid, J. E., *Biomed Microdevices* 2007, *10*, 243-249.

[27] Zhu, J., Tzeng, T.-R. J., Hu, G., Xuan, X., *Microfluidics and Nanofluidics* 2009, *7*, 751-756.

[28] Pysher, M. D., Hayes, M. A., *Analytical Chemistry* 2007, *79*, 4552-4557.

CHAPTER 2

OVERVIEW OF DIELECTROPHORETIC TECHNIQUES

2.1 Principles of electrokinetic effects

Electromagnetism gives shape and form to all matter. The chemical conglomerations that comprise this planet, its patina of life, and all of humanity, spring from the abstruse dance of electrons upon their nucleonic tethers. Every atom consists of both positive and negative charges: electrons and protons constrained together by Coulomb forces. Atomic number and charge, in concert with electron wave mechanics, govern the physical and chemical properties of matter. From DNA to proteins to cells, biological material in all shapes and sizes is composed of electrostatically-interacting atoms, molecules, polymers, and other higher-order structures. Even if it is net-neutral, every particle possesses a unique distribution of charge. The electrostatic diversity of all matter presents a valuable mode of manipulation and separation.

Electromagnetic force is one of the fundamental forces of the universe. It consists of both electric and magnetic components, but within the context of this dissertation only the electric component will be introduced and discussed. Accordingly, an abbreviated form of Lorentz's law [1], where $\boldsymbol{B}$ (the magnetic field) is set to zero, states that an electric field ($\boldsymbol{E}$) will exert force ($\boldsymbol{F}$) upon any particle possessing net charge (q). In its simplest form, this force occurs within a uniform electric field.

$$\boldsymbol{F} = q\boldsymbol{E} \tag{1}$$

In an analogous manner, electric force acts upon permanent or field-induced dipoles within a spatially non-uniform electric field [2]:

$$\boldsymbol{F} = (\boldsymbol{p} \cdot \boldsymbol{\nabla})\boldsymbol{E} \tag{2}$$

For Eq. 2, $\boldsymbol{p}$ is the dipole moment vector and $\boldsymbol{\nabla}$ is the gradient operator.

Considered together, these two equations describe the effects that uniform or non-uniform electric fields can exert upon any particles with either net charge (Eq. 1) or polarizable character (Eq. 2). And as described above, this includes nearly all material of biologic origin. Furthermore, any two hypothetical particles will experience a different magnitude of force based upon their unique distribution of charge and dipolar characteristics. With strategic generation of electric fields, these differences can be exploited to selectively manipulate, separate, and isolate the particles.

2.2 Electrophoresis and electroosmosis

Electrophoresis may represent the oldest form of material transport resulting from the application of external fields. In 600 B.C. a Greek philosopher, Thales of Miletus, observed that amber attracted motes of dust and straw after being rubbed [3]. This may have seemed magical at the time. It wasn't until two and a half millennia later, after the invention of the voltaic battery, that comprehension of this phenomenon began to evolve. While exploring the interaction between wet soil and "galvanic electricity," Ferdinand Frederic Reuss observed the migration of clay particles through a tube filled with conductive medium [4].

In the case of a charged particle of radius r suspended in a fluid of viscosity η within a uniform electric field (Fig. 2.1), the forces acting upon the particle include the Lorentz force (Eq. 1), and Stokes' drag ($f * v$). Inertial restraint can be neglected due to its small value and rapid decay with time. When the field is applied, a terminal velocity is achieved when the Lorentz force is equal to the Stokes' drag. This yields the following equation for electrophoretic velocity, ($\boldsymbol{v}_{EP}$), where $f = 6\pi r\eta$:

$$\boldsymbol{v}_{\mathrm{EP}} = \frac{\boldsymbol{F}_{\mathrm{EP}}}{f} = \frac{q\boldsymbol{E}}{6\pi r\eta} \tag{3}$$

Particle velocity is described in terms of the particle's electrophoretic mobility (μ_{EP})—a term that combines the effects of the forces described above:

$$\boldsymbol{v}_{\mathrm{EP}} = \mu_{\mathrm{EP}}\boldsymbol{E} \tag{4}$$

$$\mu_{\mathrm{EP}} = \frac{q}{6\pi r\eta} \tag{5}$$

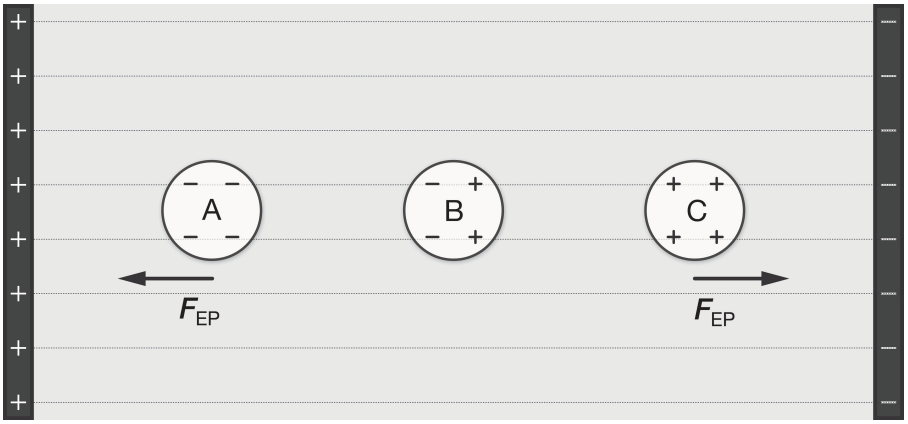

Figure 2.1. Illustration of electrophoretic force. Within a uniform electric field, small particles with non-zero net charge (A and C) experience force directed toward opposite electric potential. Particles with zero net charge (B) experience zero net force.

Reuss was first to observe another phenomenon in his soil-based experiments: electroosmotic flow. When he generated an electric field through a water-filled bed of quartz sand, the water moved through the sand. The water level began to rise in one of the terminal fluid reservoirs. Electroosmotic flow occurs in narrow channels with charged interfacial surfaces. The charged surface attracts a double layer of counter ions from the solution. The inner layer of counter ions (closest to the sidewall) is stationary, while the outer layer of more diffuse counter ions is free to electrophorese through the solution. Bulk transport of fluid within the channel results from the viscous drag of the migrating

ions in the diffuse or outer layer. As with the relationship shown for electrophoretic velocity in Eq. 5, electroosmotic velocity ($\boldsymbol{v}_{EO}$) is proportional to electric field strength and is described in terms of electroosmotic mobility (μ_{EO}).

The net electrokinetic velocity ($\boldsymbol{v}_{EK}$) of a fluid-suspended particle contained within narrow channels possessing surface charge therefore results from both electrophoretic and electroosmotic components:

$$\boldsymbol{v}_{EK} = \mu_{EK}\boldsymbol{E} = \boldsymbol{v}_{EP} + \boldsymbol{v}_{EO} = (\mu_{EP} + \mu_{EO})\boldsymbol{E} \quad (6)$$

Considered together, these two forces enable transport of net-neutral particles as well as those with positive or negative charge.

2.3 Dielectrophoresis

Dielectrophoretic force arises when spatially varying electric fields act upon permanent or field-induced dipoles (Eq. 2). The phenomenon was first explored and then formalized by H. A. Pohl in the mid-twentieth century [2]. Polarization effects within both the particle and its surrounding medium lead to a buildup of interfacial charge and contribute to the formation of a dipole moment. Because the two ends of the particle dipole occupy different regions in a non-uniform electric field, they experience differing magnitudes of force. This causes the polarized dipole to move either towards or away from regions of higher field strength (Fig. 2.2).

In its simplest form, dielectrophoretic force ($\boldsymbol{F}_{DEP}$) is expressed for a small, spherical particle of radius r, which is composed of a homogeneous and isotropic dielectric material [5]. The absolute permittivity of the surrounding medium is represented by ε_m. The Clausius-Mossotti factor (f_{CM}) is a mathematical expression relating the absolute permittivities of two dielectrics: the particle (ε_p) and the surrounding

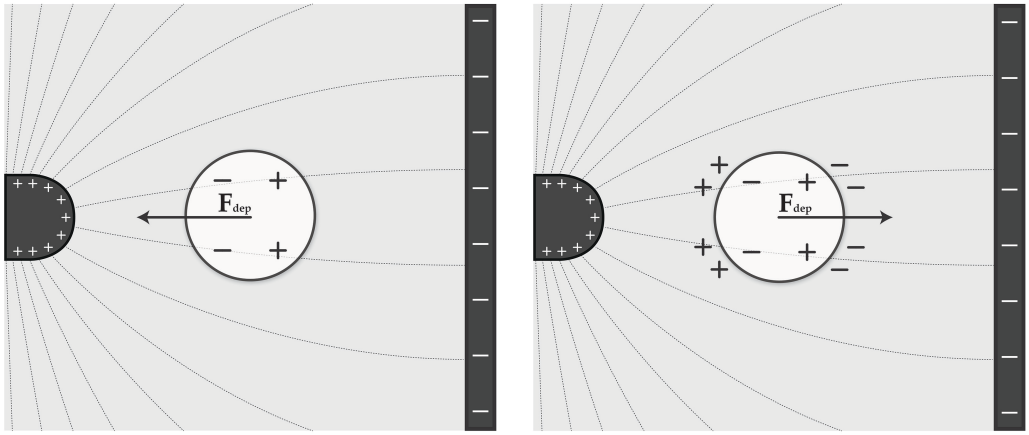

Figure 2.2. Illustration of dielectrophoretic force. Within a non-uniform electric field, polarizable particles experience a net force oriented into (left) or out of (right) areas of higher field strength. These behaviors are referred to as positive and negative DEP, respectively. Direction of DEP force is independent of field polarity. Instead, it depends upon the effective permittivity or conductivity of both the particle and the medium. In the image on the left, the particle is more polarizable than the surrounding medium. In the image on the right, the medium is more polarizable than the particle.

medium (ε_m).

$$\boldsymbol{F}_{\mathrm{DEP}} = 2\pi r^3 \varepsilon_m f_{\mathrm{CM}} \boldsymbol{\nabla}|\boldsymbol{E}|^2 \tag{7}$$

$$f_{\mathrm{CM}} = \frac{\varepsilon_p - \varepsilon_m}{\varepsilon_p + 2\varepsilon_m} \tag{8}$$

If the particle is subject to conduction losses, f_{CM} is expressed in terms of complex permittivity (ε^*) or complex conductivity (σ^*), where $i = \sqrt{-1}$ and ω is the angular frequency of the electric field.

$$\varepsilon^*{}_p = \varepsilon_p - \frac{i\sigma_p}{\omega} \tag{9}$$

$$\sigma^*{}_p = \sigma_p + i\omega\varepsilon_p \tag{10}$$

Accordingly, f_{CM} can be expressed as a complex function, using either permittivities or conductivities.

$$f^*_{\mathrm{CM}} = \frac{\varepsilon^*_p - \varepsilon^*_m}{\varepsilon^*_p + 2\varepsilon^*_m} \quad \text{or} \quad f^*_{\mathrm{CM}} = \frac{\sigma^*_p - \sigma^*_m}{\sigma^*_p + 2\sigma^*_m} \tag{11}$$

The work presented within this dissertation utilizes exclusively DC fields. Under these conditions, the angular frequency is zero, and thus DEP force depends upon the conductive properties of both the particle and the surrounding medium. The Clausius-Mossotti factor is therefore expressed in terms of simple conductivity:

$$f_{\mathrm{CM}} = \frac{\sigma_p - \sigma_m}{\sigma_p + 2\sigma_m} \tag{12}$$

The direction of a particle's travel due to dielectrophoresis depends upon the relative magnitudes of the particle and medium conductivities. Particles with higher conductivity than that of the medium will move toward regions of higher field strength (this behavior is termed "positive DEP"), and particles with conductivity less than that of the medium move toward regions of lower field strength (termed "negative DEP"). The direction of the resulting force vector relative to the field is reflected in the sign of f_{CM}, and it is from this convention that the aforementioned directional phrases derive.

Dielectrophoretic velocity and mobility are expressed in a manner similar to Eqs. 3, 4, and 5:

$$\boldsymbol{\nu}_{\mathrm{DEP}} = \frac{\boldsymbol{F}_{\mathrm{DEP}}}{f} = \frac{r^2 \varepsilon_m f_{\mathrm{CM}} \boldsymbol{\nabla}|\boldsymbol{E}|^2}{3\eta} = \mu_{\mathrm{DEP}} \boldsymbol{\nabla}|\boldsymbol{E}|^2 \tag{13}$$

$$\mu_{\mathrm{DEP}} = \frac{r^2 \varepsilon_m f_{\mathrm{CM}}}{3\eta} \tag{14}$$

A few noteworthy issues are brought to light by these equations. Each of these identifies an important distinction between dielectrophoresis and electrophoresis. First, dielectrophoretic force acts upon neutral as well as charged species. Second, it is independent of the sign of the electric field. It occurs in both AC and DC fields. Third,

the force is proportional to particle volume. As a result, it is more prominent with larger particles. It has been demonstrated on a molecular level, but only with carefully engineered systems. Fourth, dielectrophoresis requires strongly divergent fields for observable effects. Considered together, these unique aspects of dielectrophoresis open new avenues for particle transport that are not accessible by electrophoresis alone. Dielectrophoretic force can occur in concert with other electrokinetic forces; together they provide a richly-equipped toolkit for bioparticle separations.

Since dielectrophoretic force requires large field gradients, it is a highly localized phenomenon and usually occurs over small length scales. As a result, dielectrophoretic experiments often involve trapping or capturing analyte, rather than observing differential rates of transport across a distance (as often occurs in implementations of electrophoresis). Without bulk motion of analyte or fluid, only small regions of space can be interrogated using dielectrophoretic force. This limitation can be addressed by driving particles past or through dielectrophoretic action zones using electrophoresis and electroosmosis.

In order to immobilize a particle within a dielectrophoretic capture zone, the force arising from dielectrophoresis must equal or exceed all other translational forces. For this discussion, we will focus on electromotive forces, assuming that the primary contributions to particle motion within the channel are dielectrophoresis and bulk electrokinetic transport. This motion is referred to as flux (***J***)—the mass-transport rate of particles through a unit cross-section of the channel. For a dilute system with particle concentration c, the flux driven by a DC electric field can be described by the following expression:

$$\boldsymbol{J} = \frac{c}{f}[\boldsymbol{F}_{\mathrm{EK}} + \boldsymbol{F}_{\mathrm{DEP}}] \tag{15}$$

Both the electrophoretic and electroosmotic components of electrokinetic force are proportional to the electric field vector. Therefore, in the absence of other forces, all particles and fluid elements follow the electric field.

$$\boldsymbol{J} \propto \boldsymbol{E} \tag{16}$$

Consequently, the conditions required for trapping or capture are met when the following expression is true:

$$\boldsymbol{J} \cdot \boldsymbol{E} = 0 \tag{17}$$

In other words, the conditions are met when the component of particle flux along the electric field vector is zero. Complexities arise from the fact that dielectrophoretic force is not necessarily collinear with the electric field. However, since dielectrophoretic force is highly localized and tends to occur over very small length scales this simplification can serve as a reasonable approximation.

There is another implication of the localized nature of DEP: as long as the component of $\boldsymbol{F}_{\mathrm{DEP}}$ collinear with $\boldsymbol{F}_{\mathrm{EK}}$ exceeds the magnitude of $\boldsymbol{F}_{\mathrm{EK}}$, then $\boldsymbol{F}_{\mathrm{DEP}}$ will act as a kinetic hurdle and create a steady-state zone of trapped material. This is reflected by the use of an inequality in Eq. 18 and beyond.

Substituting Eq. 15 into Eq. 17 yields the following expression, which can be equivalently expressed in terms of particle mobilities and field values as shown in Eq. 3, 4, and 13:

$$\frac{c}{f}[\boldsymbol{F}_{\mathrm{EK}} + \boldsymbol{F}_{\mathrm{DEP}}] \cdot \boldsymbol{E} \;=\; c[\mu_{\mathrm{EK}}\boldsymbol{E} + \mu_{\mathrm{DEP}}\boldsymbol{\nabla}|\boldsymbol{E}|^2] \cdot \boldsymbol{E} \;\leq\; 0 \tag{18}$$

Further rearrangement yields the following two expressions for particle trapping:

$$\frac{\mu_{\mathrm{DEP}}\nabla|\boldsymbol{E}|^2\cdot\boldsymbol{E}}{\mu_{\mathrm{EK}}E^2} \geq 1 \tag{19}$$

$$\frac{\nabla|\boldsymbol{E}|^2\cdot\boldsymbol{E}}{E^2} \geq \frac{\mu_{\mathrm{EK}}}{\mu_{\mathrm{DEP}}} \tag{20}$$

The form of Eq. 20 is relevant since it describes the conditions for particle trapping in terms of a comparison between field characteristics and particle characteristics. The significance of the relationship is explored in more detail in succeeding chapters, particularly in Chapter 5.

2.4 Dielectrophoresis of biological particles

Most particles are not ideal. In the case of real-world particles, dielectrophoretic force depends upon extremely complex variables. Biological particles are especially complex entities. They often consist of multiple subdomains that all possess independent or semi-independent dielectric properties. These subdomains are never spherical, lossless, or isotropic. Living cells, for instance, consist of multiple aqueous regions separated by semipermeable membranes. The lipid membrane itself is composed of polar molecules and contains highly peripatetic membrane-bound proteins. Internal structures such as the cytoskeleton and organelles are also polarizable, semi-mobile, and likely contribute to the overall dipolar character of the cell. These physicochemical characteristics can vary significantly between biological targets, even with only slight differences in genotype.

Theoretical and numerical treatments usually approximate cells as simple spheres or ellipsoids, consisting of a thin outer membrane and an inner cytosol, each with a different conductivity. Nucleated cells can be approximated with two concentric spheres; this is a three-shell model that accounts for the outer plasma membrane, the cytosol, and

the inner nuclear membrane. These approaches are collectively referred to as multishell models [6].

A significant amount of theoretical and experimental work has developed and extended multishell models to account for the intricacies of biological cells. Such models can account for both nonspherical and anisotropic shells [7-9]. Often, multishell modeling theory is accompanied by experiments that measure the dielectrophoretic response of particles over a range of AC field frequencies. These models have helped broaden theoretical understanding of the electric properties of cells. Furthermore, they can predict expected dielectrophoretic behavior, including crossover frequency (the AC field frequency where DEP response changes from positive to negative). Multishell models prove especially informative for attempts to distinguish particles based on their AC dielectrophoretic response curve [10].

This dissertation focuses on experimental differentiation and separation of similar bioparticles by relying upon electrokinetic transport phenomena. The technique explored and presented here is compatible with the use of AC fields, but presently utilizes only DC fields. Frequency response curves and crossover frequencies provide valuable information about the dielectrophoretic behavior of bioparticles, but they do not appreciably inform experimental design for transport-based and DC dielectrophoresis. The equations developed in Chapter 5 focus on adapting separation science and resolution theory to the unique implementation of DEP explored herein.

2.5 Implementation and development of the technology

Electric fields are generated by charge and propagate (to varying degrees) through

dielectric media. All forms of matter affect and interact with electric fields in unique manners. As a result, physical materials can be engineered to create and control electric fields: conductive electrodes can deliver charge and thus create fields; aqueous dielectric media can both conduct current and propagate electric fields; insulators can shape and direct resulting fields.

Early dielectrophoretic experiments produced non-uniform fields by introducing asymmetrical arrangements of electrodes into a dielectric medium [11]. With small electrode spacing, this approach can create large field gradients. Pohl used closely spaced wire electrodes in a fluid-filled chamber to separate various types of mixed particles [12, 13]. Particles would move toward one electrode or the other, based on whether they experienced positive or negative DEP. The chamber, electrodes, and particles were observed and photographed through a microscope.

Dielectrophoretic techniques have advanced considerably since then. Photolithography and other microfabrication techniques have given researchers greater control over microelectrode geometry and positioning [14]. Typically, thin-film deposition has been used to pattern planar metallic microelectrodes on an insulating substrate (Fig. 2.3). These electrodes create field gradients, either driven by a voltage source or allowed to float in the presence of an AC field. Downscaling the size and optimizing geometry allowed formation of stronger field gradients with lower applied voltage. Early electrode designs featured castellated and interdigitated electrodes [15-18], along with polynomial designs [19, 20]. These were followed by other permutations including zipper-like designs [21] and ratchets [22]. Dielectrophoretic research flourished

as clever innovations in geometry and fabrication solved unique problems or introduced new applications of the technique.

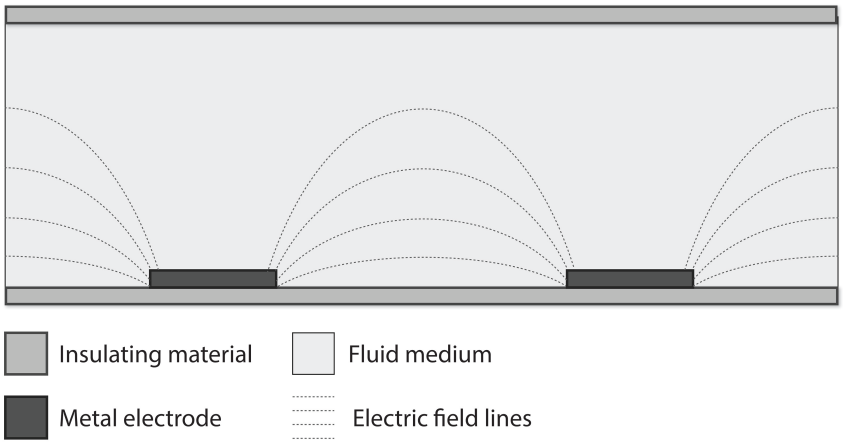

Figure 2.3. Cross-sectional view of a microelectrode DEP system. Planar metal electrodes are patterned onto an insulating substrate. The electric field is focused at the edges of the electrode, creating non-uniform fields that drive DEP.

Electrode-based DEP is a richly diverse field of research, fueled by hundreds of publications within the past few decades. However, since Pohl's earliest experiments, researchers have recognized that electrodes introduce highly variable phenomena that interfere with the system. They react electrochemically with the aqueous medium and generate bubbles, create unwanted flow, and are subject to fouling. Electrodes also violate the conditions required for electrokinetically-driven bulk transport. Electrode-based dielectrophoretic experiments often consist of closed-chamber variations (with no bulk transport), or they use dispersive pressure-driven flow.

According to Ohm's law, the voltage drop across any material is proportional to its resistance. Voltage drop is greater across materials or regions with higher resistance, and thus a stronger electric field is produced. Resistance, in turn, is inversely proportional

to the cross-sectional area of the medium; a reduced cross-section results in higher resistance, greater voltage drop, and thus higher field strength. In this manner, shaped insulators can impinge upon an electric field to create regions of higher and lower field strength. If the sides of a channel are composed of insulating material, then geometric variations in the insulating walls produce non-uniform fields. Constriction or expansion of the sidewalls or the presence of insulating obstacles in a microchannel create field gradients that can generate dielectrophoretic force (Fig. 2.4). Engineering channel geometry in this manner allows field production by electrodes housed in distal reservoirs, rather than within or proximal to the separation or capture zone. This minimizes the interference of electrode-initiated electrochemical reactions, and facilitates electrokinetic conveyance of fluid and material through the separation zone. Additional benefits afforded by insulator-based dielectrophoresis (iDEP) include simplified microfabrication and compatibility with in-channel optical analysis. While the more traditional electrode-based DEP allows large electrical gradients to form with lower voltages, the advantages presented by iDEP make this a favorable compromise.

Insulator-based dielectrophoresis is a relatively new area of research. In 1989, Masuda et al. published the first example of insulators being used specifically to create dielectrophoretic force [23]. The experiment was not overtly or exclusively focused on dielectrophoresis. It concentrated instead on a specific biological application: contactless trapping and electrofusion of pearl-chained cells. This work served as a quiet forerunner for the hundreds of research articles on iDEP that would follow over a decade later.

In 2002, Chou et al. reported using an array of constricting, insulating obstacles in a microchannel along with an AC electric field to capture single-stranded and double-

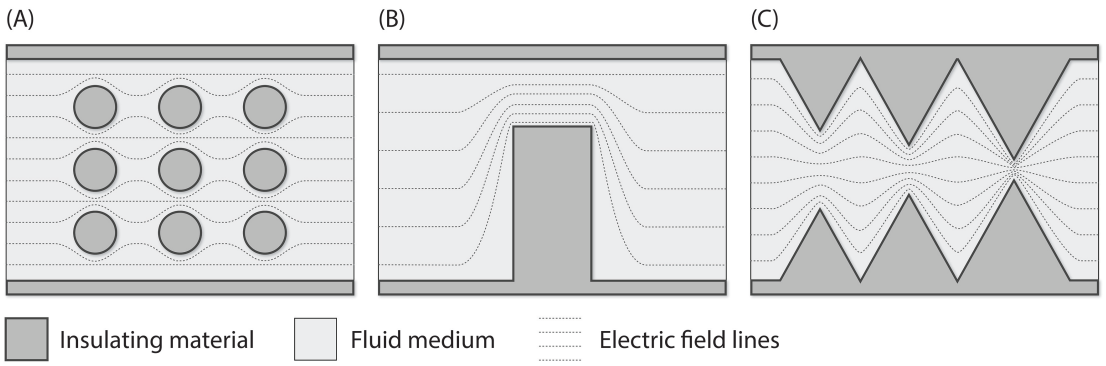

Figure 2.4. Illustration of insulating structures used to shape field gradients within a microchannel. Note that field-generating electrodes are not shown here—they are presumed to reside in distal reservoirs. Common designs include post-based arrays (A) and rectangular hurdles (B). The work presented in this dissertation utilizes an angular geometry (C) that creates intense local field gradients. In the case of channel C, varied spacing and size along the channel allow differentiated DEP forces.

stranded DNA [24]. In this case, the obstructions shape non-uniformities in the electric field and create DEP traps. This was accomplished using lower frequencies than those typically used with micro-electrode designs. A year later, Cummings and Singh described the use of insulating posts with low frequency or DC electric fields to direct particles into different flow paths based on the relative influence of dielectrophoretic and electrokinetic force [25]. They called this effect "streaming DEP." They also noted steady-state trapping and concentration of particles near the insulating posts when applying relatively large electric fields (100 V/mm). This effect they referred to as "trapping DEP." Their publication represented the first example of dielectrophoretic trapping with electrokinetically-driven bulk transport. This important innovation allowed the experimenters to deliver more sample and analyte to the dielectrophoretic capture zones. Sample was conveyed to the capture zone by the same field that induced DEP force, allowing them to "scour" significantly larger volumes of sample.

Lapizco-Encinas et al. further developed this work, using an array of uniformly sized posts contained within a straight microchannel to capture biological targets [26]. They demonstrated capture of multiple species of bacteria, as well as selective concentration of live bacteria from a mixture of both live and dead cells [27].

Various implementations of iDEP have been demonstrated over the past few years, using features such as glass beads [28], nanopipettes [29], insulating hurdles [30], and serpentine channels [31]. These methods can be used to achieve particle separation in a variety of ways. However, most can be categorized as either differential deflection or trapping. Deflection exploits the effects of streaming dielectrophoresis to divert particles into different fluid paths or streamlines based upon their electrokinetic and dielectrophoretic mobility. These approaches resemble field flow fractionation, where the relevant separatory force component acts perpendicularly to bulk transport. Enrichment of analyte populations within different streamlines is sometimes considered sufficient separation. In other devices, a more significant spatial separation is accomplished with downstream bifurcation or branching of the channel [32]. Diverted populations may be sent to different regions of a microdevice for either collection or downstream analysis. Trapping dielectrophoresis halts the forward translation of particles, based on their electrokinetic and dielectrophoretic mobility. In these cases, the relevant separatory force component acts collinearly with bulk transport (Eqs. 17 through 20). Trapping has also been accomplished using a wide variety of insulator geometries and implementations. However, it usually results in a simple bifurcation of analyte populations. Any species with a mobility ratio (Eq. 20) above a particular value will pass through the trap(s), while

those with a mobility ratio below that value will be stopped and form a concentrated band.

2.6 Introduction and application of a new DEP paradigm

Gradient insulator-based dielectrophoresis (g-iDEP) was built upon prior developments in iDEP. However, it differs from other significant contributions that have been made in this arena. Other strategies have primarily focused on trapping and sample bifurcation, or multiple-outlet diversion strategies. Each of these approaches either bifurcates a sample population, or diverts analyte into a limited number of outputs. The scheme discussed here is an amalgam of iDEP and traditional separation science. It represents a new approach combining continuous and equilibrium gradient separations.

Within g-iDEP, a combination of EK and DEP forces are used to transport, separate, and concentrate particles within a channel. This technique utilizes a continuous microchannel patterned with sequentially changing, constrictive insulating features. These constrictions, referred to as gates, create a series of DEP-inducing electric field non-uniformities. The specific geometry of the channel yields increasingly strong DEP forces along the channel. Particles traveling through the microchannel are propelled by DC field-driven EK motion. Even in their present iteration, these channels would also be compatible with the use of DC-offset AC electric fields. Since DEP forces scale differently with the channel's cross-sectional area than do EK force, unique traps are formed at each gate as they become sequentially narrower. This causes physically distinct particles to settle into discrete zones near different gates. Thus, the particles assume unique positions along the channel's separatory axis based on their electrokinetic and dielectrophoretic mobilities (Fig. 2.5). Considered together, a particle's electrophoretic

and dielectrophoretic mobilities reflect an array of properties including size, charge, polarizability, shape, and heterogeneity. Interrogating all these properties together yields a separatory scheme that can be fine-tuned for high-resolution capture and concentration of analytes. As shown in Chapter 5, this work will also allow estimation of the smallest change in electrokinetic or dielectrophoretic properties that can be uniquely differentiated by g-iDEP.

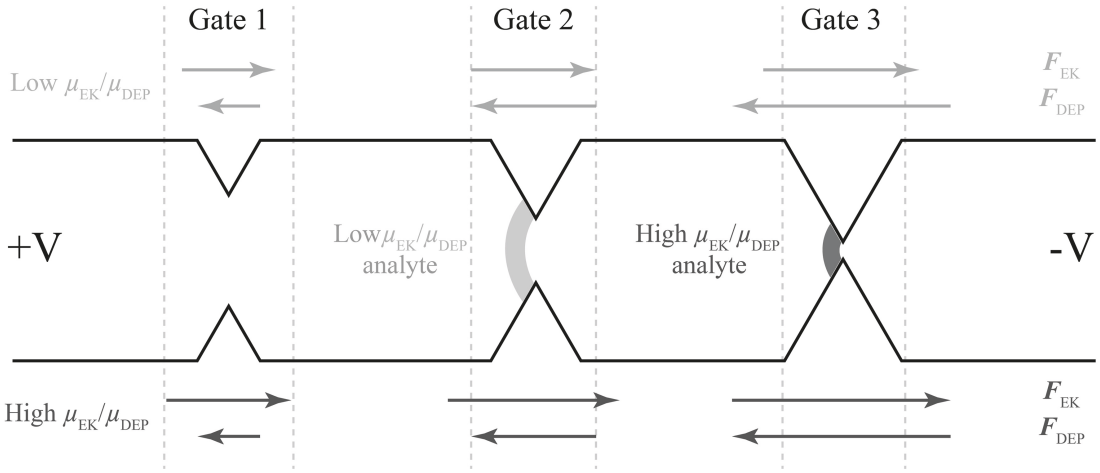

Figure 2.5. Representation of separation within a g-iDEP device. Arrows depict the component forces acting upon two distinct analytes (light and dark gray) traveling along the channel centerline. Net force acting upon particles is indicated by the vector sum of the two arrows in each pair. Analytes will form stationary concentration profiles at gates where their electrokinetic and dielectrophoretic forces are equal and opposite.

This technique is conducive for use with analytes that range from a few tens of nanometers to tens of micrometers in diameter. It is especially well suited for a large portion of bioparticulates (viruses, organelles, cells, lysosomes, vesicles, etc.). This technique employs localized, stair-stepped gradients to create multiple steady-state, focused bands of captured material. It differs significantly from true continuous

separation gradient techniques because it is directional; the analyte must be introduced from a single side of the device. There is no mechanism to refocus material once past the first focus or balance point. This is an important distinction for classification according to separation science and will affect certain operating paradigms, but the general advantages of gradient separation techniques are accessible for this strategy also. This technique has demonstrated isolation and concentration of a wide range of particles, including polystyrene spheres [33], red blood cells [34], amyloid fibrils [35], and various types of bacteria [36, 37]. Gradient insulator-based dielectrophoresis is a powerful approach for multiple simultaneous bioparticle separations because it targets a wide array of physical and chemical properties that contribute to particle polarizability.

2.7 References

[1] Chen, W. K., *The Electrical Engineering Handbook*, Elsevier Science 2004, p. 486.

[2] Pohl, H. A., *Dielectrophoresis: The Behavior of Neutral Matter in Nonuniform Electric Fields*, Cambridge University Press 1978.

[3] Ida, N., *Engineering Electromagnetics*, Springer International Publishing 2015, p. 96.

[4] Garfin, D. E., Ahuja, S., *Handbook of Isoelectric Focusing and Proteomics*, Elsevier Academic Press 2005, pp. 14-15.

[5] Pethig, R., *Biomicrofluidics* 2010, *4*, 022811.

[6] Jones, T. B., *Electromechanics of Particles*, Cambridge University Press 2005.

[7] Sancho, M., Martínez, G., Martin, C., *Journal of Electrostatics* 2003, *57*, 143-156.

[8] Vrinceanu, D., Gheorghiu, E., *Bioelectrochemistry and bioenergetics* 1996, *40*, 167-170.

[9] Sukhorukov, V. L., Meedt, G., Kurschner, M., Zimmermann, U., *Journal of Electrostatics* 2001, *50*, 191-204.

[10] Huang, Y., Holzel, R., Pethig, R., Wang, X. B., *Physics in Medicine and Biology* 1992, *37*, 1499-1517.

[11] Pohl, H. A., Hawk, I., *Science* 1966, *152*, 647-649.

[12] Pohl, H. A., Crane, J. S., *Biophysical Journal* 1971, *11*, 711-727.

[13] Crane, J. S., Pohl, H. A., *Journal of the Electrochemical Society* 1968, *115*, 584-586.

[14] Mack, C., *Fundamental Principles of Optical Lithography*, John Wiley & Sons 2011.

[15] Pethig, R., Huang, Y., Wang, X. B., *Journal of Physics D: ...* 1992.

[16] Price, J. A., Burt, J. P., Pethig, R., *Biochimica et biophysica acta* 1988, *964*, 221-230.

[17] Becker, F., Wang, X., *Journal of Physics D: Applied Physics* 1994.

[18] Washizu, M., Nanba, T., Masuda, S., *Ieee Transactions on Industry Applications* 1990, *26*, 352-358.

[19] Washizu, M., *Journal of Electrostatics* 1993, *29*, 177-188.

[20] Huang, Y., Pethig, R., *Measurement Science and Technology* 1991, *2*, 1142.

[21] Hoettges, K. F., Hughes, M. P., Cotton, A., Hopkins, N. A., McDonnell, M. B., *IEEE engineering in medicine and biology magazine : the quarterly magazine of the Engineering in Medicine & Biology Society* 2003, *22*, 68-74.

[22] Gonzalez, C. F., Remcho, V. T., *Journal of Chromatography A* 2009, *1216*, 9063-9070.

[23] Masuda, S., Washizu, M., Nanba, T., *Ieee Transactions on Industry Applications* 1989, *25*, 732-737.

[24] Chou, C. F., Tegenfeldt, J. O., Bakajin, O., Chan, S. S., Cox, E. C., Darnton, N., Duke, T., Austin, R. H., *Biophysical Journal* 2002, *83*, 2170-2179.

[25] Cummings, E., Singh, A., *Analytical Chemistry* 2003, *75*, 4724-4731.

[26] Lapizco-Encinas, B., Simmons, B., Cummings, E., Fintschenko, Y., *Electrophoresis* 2004, *25*, 1695-1704.

[27] Lapizco-Encinas, B., Simmons, B., Cummings, E., Fintschenko, Y., *Analytical Chemistry* 2004, *76*, 1571-1579.

[28] Suehiro, J., Zhou, G., Imamura, M., Hara, M., *Ieee Transactions on Industry Applications* 2003, pp. 1514-1521.

[29] Ying, L., White, S., Bruckbauer, A., Meadows, L., Korchev, Y., Klenerman, D., *Biophysical Journal* 2004, *86*, 1018-1027.

[30] Kang, Y., Li, D., Kalams, S. A., Eid, J. E., *Biomed Microdevices* 2008, *10*, 243-249.

[31] Zhu, J., Tzeng, T.-R. J., Hu, G., Xuan, X., *Microfluidics and Nanofluidics* 2009, *7*, 751-756.

[32] Srivastava, S. K., Baylon-Cardiel, J. L., Lapizco-Encinas, B. H., Minerick, A. R., *Journal of Chromatography A* 2011, *1218*, 1780-1789.

[33] Staton, S. J. R., Chen, K. P., Taylor, T. J., Pacheco, J. R., Hayes, M. A., *Electrophoresis* 2010, *31*, 3634-3641.

[34] Jones, P. V., Staton, S. J. R., Hayes, M. A., *Analytical and Bioanalytical Chemistry* 2011, *401*, 2103-2111.

[35] Staton, S. J. R., Jones, P. V., Ku, G., Gilman, S. D., Kheterpal, I., Hayes, M. A., *Analyst* 2012, *137*, 3227.

[36] Pysher, M. D., Hayes, M. A., *Analytical Chemistry* 2007, *79*, 4552-4557.

[37] Jones, P. V., DeMichele, A. F., Kemp, L., Hayes, M. A., *Analytical and Bioanalytical Chemistry* 2014, *406*, 183-192.

CHAPTER 3

BLOOD CELL CAPTURE IN A SAWTOOTH DIELECTROPHORETIC MICROCHANNEL

3.1 Introduction

Along with all vertebrates and many invertebrates, humans rely on blood for life. Blood is a rich, heterogeneous, and complex fluid that fulfills many indispensable physiologic roles, far beyond the realm of simple oxygen delivery. The circulatory system continuously delivers key nutrients to distant tissues of the body, while simultaneously removing metabolic byproducts to prevent toxic buildup. In addition, it acts as a rapid transit system for a variety of cells and chemical messengers.

Human blood is composed of two primary constituents: plasma and cells. Both of these contain diverse subgroupings of materials. The plasma is an aqueous medium, composed of 90 percent water. Proteins contribute another six to eight percent of total, the most abundant being albumins, globulins, and fibrinogen [1]. Other solutes include a variety of ions and small molecules, such as cofactors, hormones, lipids, carbohydrates, and amino acids. Blood cells are typically classified as erythrocytes, leukocytes, or thrombocytes. Erythrocytes, or red blood cells (RBCs), constitute the vast bulk of total cell volume within blood, making up roughly 45 percent of total blood volume and accounting for more than 99 percent of all blood cells. RBC populations are relatively homogeneous within a single individual, but their physical characteristics can vary with blood type, cell age, and disease state [2]. Pathologies that affect red blood cells include genetic disorders such as anemia and spherocytosis, as well as parasitic infections such as malaria [3].

The complex heterogeneity of blood and its compositional variation in response to the physiologic state of the organism make it a rich source of information. Clinicians rely on blood tests for accurate diagnosis of a wide array of diseases. Interestingly, some analytical procedures, such as the peripheral blood smear, have persisted unchanged for decades. These methods, while technologically archaic, can still yield valuable and accurate results. Their chief limitations arise from the need for experienced technologists or hematologists and the difficulty of evaluating a large number of samples from multiple individuals. Culturing or assays are often used to detect pathogens, but such approaches are time-consuming and expensive. State-of-the-art diagnostic solutions usually involve flow-cytometry, which improves the accuracy and throughput of hematologic tests, but requires sophisticated laboratory facilities, expensive equipment, and trained specialists [4].

Emergent bioanalytical technologies are designed to improve upon existing methods by decreasing the time from sample collection to analysis, integrating multiple diagnostic vectors, and producing new statistically significant clinical findings, while reducing costs and processing times and increasing portability. So-called lab-on-a-chip devices offer the possibility of comprehensive analysis performed at the patient's bedside: a prospect that would likely have a profound impact on the practice of medicine, especially in low-resource settings.

Electrokinetic approaches have proven extremely versatile in microfluidic applications, including separations [5]. Dielectrophoresis (DEP), in particular, provides several key benefits over other traditional separation schemes. Centrifugation, for example, can separate bioparticles based on their size and mass, but separation of

particles with relatively small size differences may require high speeds and long run-times [6]. Beyond the separation capabilities of centrifugation, similarly sized bioparticles often differ radically in their structure, deformability, and polarizability. Dielectrophoretic forces can uniquely couple with these physical traits, allowing sorting and capture based on far more than size or density alone [7]. For instance, using DEP, seemingly similar cells can be differentiated based on subtle distinctions such as antigen type on erythrocytes, or living versus dead bacteria [8, 9].

Much of the recent focus on dielectrophoretic bioseparations has emphasized the use of AC fields, attributable to known advantages such as frequency-dependent electrokinetics. Innovative researchers have studied a variety of phenomena at micro- or nano-scopic dimensions, including DEP, electrorotation, and dielectric levitation [10-12]. Both novel and informative, many of these techniques enable analysis of small, even single-cell samples [13]. However, these devices often leave unsolved the problems of sample dilution, continuous high-throughput testing, or truly diverse and complex biological samples.

The research presented here utilized insulating sawtooth shapes along the edge of a microchannel to create electric field variations. To investigate the application of a potentially inexpensive and portable DC insulator-gradient DEP platform for blood-based diagnostics, whole blood samples were tested within such a device. Red blood cells were successfully and reproducibly captured within a spatially confined section of the sawtooth microchannel. Some cells were observed to pass through these sections, supporting the existence of subpopulations with lower ratio of dielectrophoretic mobility (μ_{DEP}) to electrophoretic mobility (μ_{EP}) than captured cells. Future modifications to

insulator geometry may enable differentiated isolation of such subpopulations. Although this possibility is underscored by recent papers which describe dielectrophoretic characterization of RBCs based on cell age [14] and ABO antigen type [8], such efforts have all revolved around the use of electrode-based DEP. This work marks the first attempt to capture and isolate RBCs using DC-iDEP.

3.2 Materials and methods

Experiments were conducted in microfluidic devices constructed from glass and polydimethylsiloxane (PDMS). Blood cells suspended in isotonic phosphate buffer were introduced into the channel from one end. External platinum electrodes connected to a high-voltage power supply were inserted into access reservoirs at each end of the microchannel and used to apply a DC potential (ΔV_{global}) across the entire device (Fig. 3.1). RBCs and other materials were transported and captured within the channel.

3.2.1 Microdevice Fabrication

Microfluidic devices were fabricated using adaptations of standard soft lithographic techniques [15]. Microchannel templates were created on Si wafers with AZ P4620 positive photoresist (AZ Electronic Materials, Branchburg, NJ) and contrast enhancement material CEM388SS (Shin-Etsu MicroSi, Inc., Phoenix, AZ) [7]. The resist was exposed via contact photolithography with a photomask designed and created using AutoCAD (Autodesk, Inc., San Rafael, CA). PDMS (Sylgard 184, Dow/Corning, Midland, MI) was poured over the template and allowed to cure for one hour at 70° C. Afterwards, 2-mm diameter access holes were punched through the PDMS to access reservoirs at each end of the microchannel. The imprinted PDMS surface was oxidized using a handheld corona discharge emitter (Electro-Technic Products, Inc., Chicago, IL)

set to 50 kV. The PDMS slab was then contact-sealed to a glass coverplate, which had previously been triple-washed with an Alconox solution, rinsed with 18 MΩ water and 100% isopropyl alcohol, then dried for six hours at 450° C.

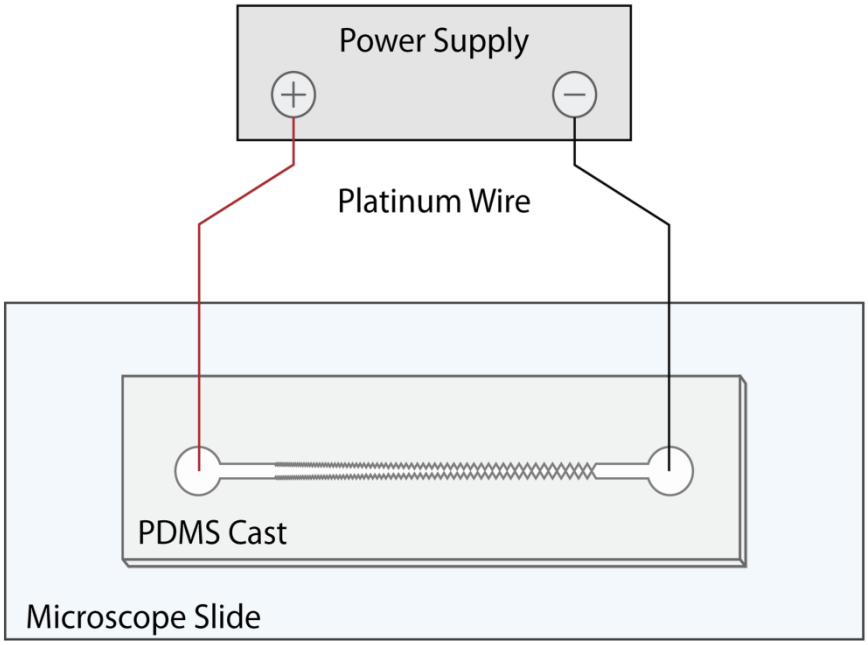

Figure 3.1. Schematic of the apparatus used in these experiments. A high-voltage, DC power supply was used to generate field potentials within the microchannel. Platinum wires were inserted into access reservoirs punched through the PDMS cast. A microscope slide or a glass plate was used to seal the channel, following oxygen plasma treatment of the PDMS surface.

The microchannel geometry was composed of successively larger, equilateral triangular units lining each side of the channel [16]. The apex of each triangle coincided with another on the opposite side, forming sequentially narrower gaps, or gates, along a gradually converging sawtooth pattern. The smallest triangles consisted of 6 µm sides and a 5.2 µm height. The side-length of the triangles increased by 40 µm after every sixth repeat. This yielded an overall design with an initial gate width of 945 µm and a final

gate width of 27 μm. The whole channel length was 4.1 cm with an average depth of 14 ±1 μm.

3.2.2 Sample Preparation

Fresh, whole blood was obtained from a human donor by venipuncture or capillary blood draw. Samples obtained via venipuncture were collected in vacutainers containing 1.8 mg/mL K_2EDTA and stored in a refrigerator at 4°C for up to 4 days. Samples obtained via fingerstick were collected in a microcentrifuge tube containing 1 mL isotonic sodium phosphate buffer with EDTA. Samples obtained in this manner were used within a few hours of collection. In certain experiments, diluted whole blood was used for analysis. In others, the sample was centrifuged and cells were washed with additional phosphate buffer to remove plasma and serum proteins.

For staining, blood cells were suspended in buffer containing 5 μM Vybrant DiO dye (Invitrogen, Inc., Carlsbad, CA) at 0.5% hematocrit. Excitation and emission wavelengths for this dye are 484 and 501 nm, respectively. The sample was incubated for 15 minutes at 37°C then centrifuged and washed three times in order to remove free dye molecules. The final cell pellet was resuspended in sodium phosphate buffer, pH 7.4, with concentrations typically between 100 and 130 mM (Fig. 3.2). Conductivities for these buffers were 12.5 and 15.5 mS/cm, respectively. Sufficient buffer was added to yield an absolute cell count of 22-56 cells/nL, based on a presumed mean corpuscular volume (MCV) of 90 fL [17]. This MCV corresponds with the typical RBC disk diameter of 6-8 μm and thickness of 2 μm.

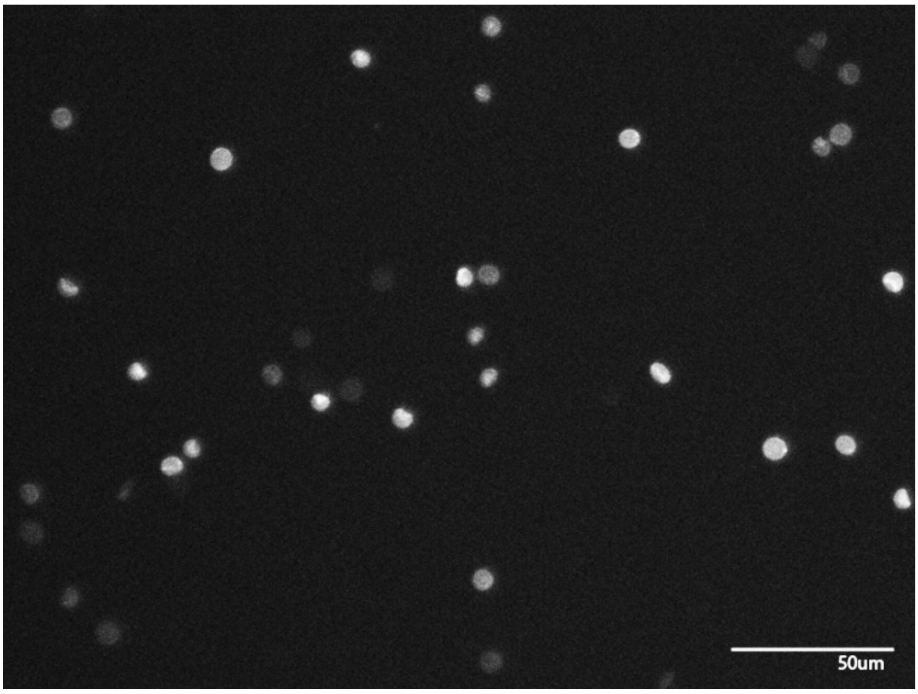

Figure 3.2. Image showing fluorescently-labeled, washed, and re-suspended RBCs. After labeling, a small aliquot of cell suspension was placed on a microscope slide with a coverslip. Cells were examined to verify successful labeling as well as cell integrity.

3.2.3 Experimental Procedure

A small amount of buffer was pipetted into the sample port on the wide-gated end of the channel, hereafter referred to as the inlet reservoir, allowing the channel to fill passively via capillarity. The device was inspected under optical magnification for uniform fluid distribution, absence of debris, and well-formed microstructures. A blood sample was then pipetted into the inlet reservoir. Once cells had entered the device hydrodynamically, achieving uniform distribution within the channel, buffer was added to the opposite access port to balance the hydrodynamic pressure. The loaded device was then situated on top of a microscope stage. Platinum electrodes (0.404 mm external diameter 99.9% purity, Alfa Aesar, Ward Hill, MA) were inserted through the access

ports into the terminal reservoirs and connected via alligator clips to a Series 225 DC power supply (Bertan High Voltage Corp., Hicksville, NY).

3.2.4 Data Collection

Experiments were observed on an Olympus IX70 inverted microscope with a ×4 or ×10 objective. Samples were illuminated with a mercury short arc lamp (H30 102 w/2, OSRAM) and an Olympus DAPI, FITC, Texas Red triple band-pass cube (Olympus, Center Valley, PA). Videos and still images were collected with a monochrome QICAM cooled CCD camera (QImaging, Inc., Surrey, BC) and Streampix III image capture software (Norpix, Inc., Montreal, QC).

3.2.5 Mathematical Modeling

Electric field characteristics in the microchannel were numerically modeled with finite element software (COMSOL, Inc., Burlington, MA). The model consisted of properly scaled 2D geometry of the main channel, excluding the device reservoirs. A 2D approximation greatly simplifies the calculations and was used since the electrical potential is presumed to vary minimally across the relatively small depth of the microchannel. The conductivity and relative permittivity of the medium were set to 1.2 S/m and 78, respectively. Additional information about software modeling is located in Appendix A.

3.2.6 Safety Considerations

All experiments were carried out in a Biosafety Level II laboratory, with approval from the Institutional Review Board for human subjects.

3.3 Results

The behaviors of several different complex biological samples associated with blood were examined using DC fields and gradient insulator dielectrophoresis (g-iDEP). Samples included diluted whole blood, washed cells, isolated RBCs, and diluted blood plasma. Capture of RBCs and other particles was investigated while varying the buffer and globally applied potential. During the course of the experiments, buffers were varied between 100 and 130 mM sodium phosphate maintained near a physiological pH of 7.4 and ΔV_{global} was varied from 200 to 700 V (49 to 171 V/cm). These buffer concentrations correspond roughly to osmolarities of 225 to 325 mOsM, thus bracketing the mean physiological value of 289 mOsM for human serum [18]. The ionic strength of the suspension buffer was varied to some extent, but significant departures from isotonicity resulted in hemolysis. Suspension in near-isotonic buffers reduces the osmotic pressure, minimizing stress and deformation of erythrocytes. A limited number of experiments were performed using buffer concentrations as low as 20 mM (σ = 0.38 mS/cm), but rapid lysing during sample preparation and experimentation restricted the range of observations.

Certain characteristic behaviors were observed in nearly all experiments (Fig. 3.3). Immediately after a DC potential was applied to the channel, particles moved towards the outlet reservoir, where the negative electrode was located. Removal of the potential caused all observable motion to cease immediately. Little or no particle capture was detected in the wider segments of the channel. Instead, cells and debris in these regions followed continuous paths towards the outlet. The pathlines traced by these particles exhibited marked similitude to the electric field lines modeled from the channel

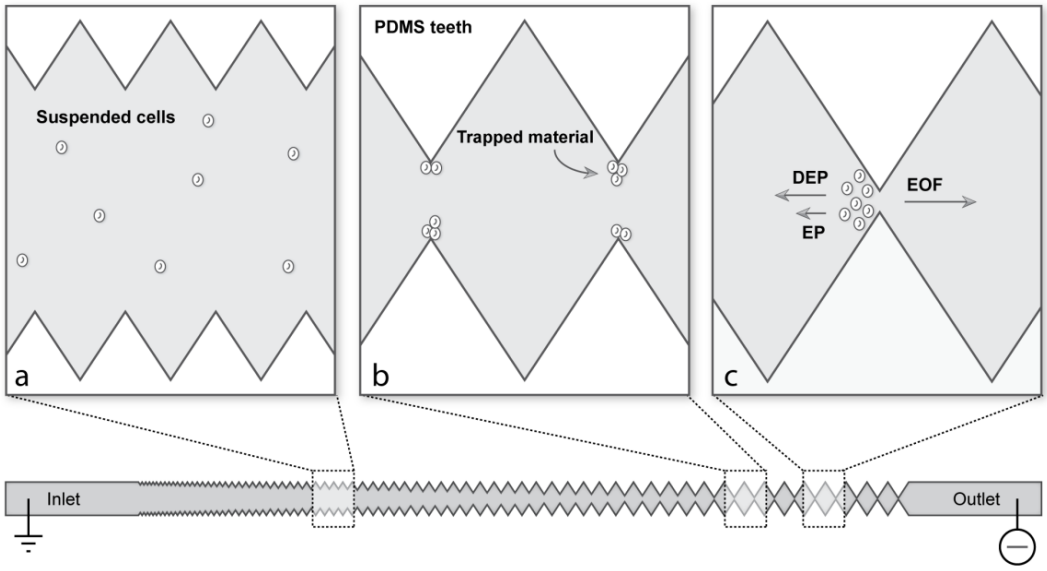

Figure 3.3. Schematic representation of the patterned microchannel. Showing unhindered passage (a), type 2 capture (b), and type 1 capture (c) of RBCs.

geometry. At narrow gates, cells and other particles appeared to divert from field pathlines and become trapped (note that Fig. 3.4 presents field contours, not field lines—lines are perpendicular to contours). In these cases particles were seen to stop both centrally, within the suspending medium, and peripherally, at or near the channel walls.

Two general types of capture were observed within the sawtooth channel (Fig. 3.5) and they are defined here for clarity of the narrative, rather than any distinct physical feature or process. Type 1 capture was observed first. In this scenario, RBCs began to collect near the channel centerline. These RBCs appeared to be whole and unfragmented, resisted bulk fluid motion, appeared to float freely in solution, and aggregation between particles was minimal. In some cases, the captured RBCs formed short pearl-chains of three to six cells axially oriented along field lines. Type 1 capture commenced immediately after application of a sufficient global potential. Collection occurred

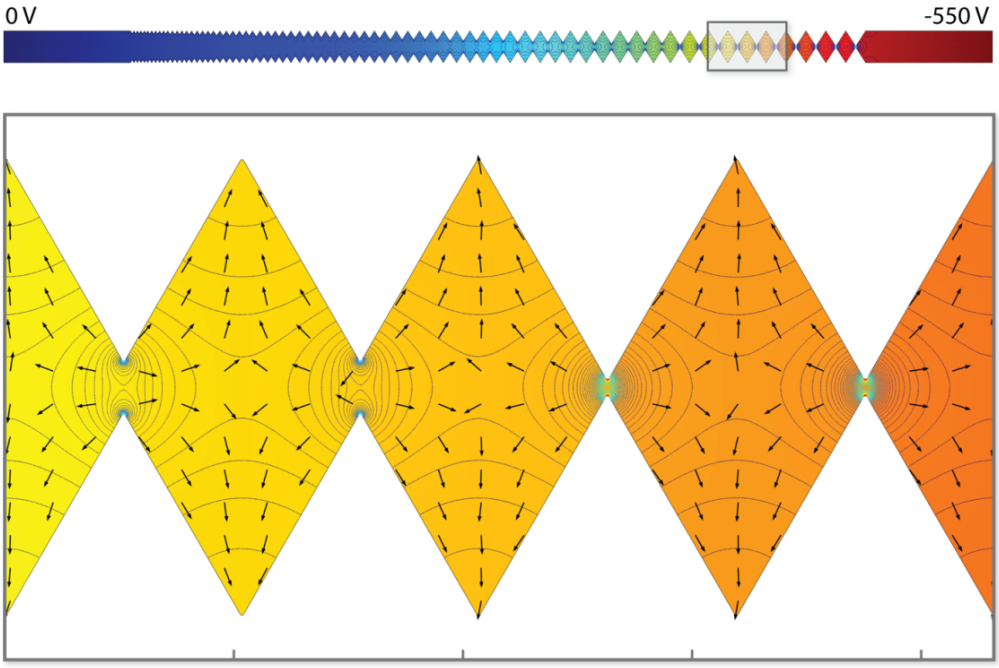

Figure 3.4. Model showing electrical field properties within the channel computed using COMSOL Multiphysics. In this representation, the solid colored surface represents the local potential, contour lines correspond to the magnitude of the electric field ($\boldsymbol{E}$), and arrows (normalized) indicate the direction of dielectrophoretic force (proportional to $\boldsymbol{\nabla}|\boldsymbol{E}|^2$) for negative DEP. Under the conditions used in these experiments, EOF was the primary driving force, causing RBCs to move from the inlet to the outlet reservoir. As particles travel through successively narrower gates, they encounter increasing DEP forces. When a particle reaches a gap with a sufficiently large gradient, the DEP overcomes the other electrokinetic forces, effectively trapping the particle at that site.

immediately upstream of the 27 μm gates, which are located nearest to the channel outlet. Type 2 capture involved smaller particles (including fragmented RBCs), which exhibited different electrokinetic behavior by collecting primarily at the apices of PDMS teeth. Particles captured in this manner exhibited a high degree of aggregation. Type 2 capture was observed only after 3-5 minutes of applied voltage. Under typical experimental conditions, this behavior was observed primarily at 90 μm gates, located upstream from the primary site of Type 1 capture.

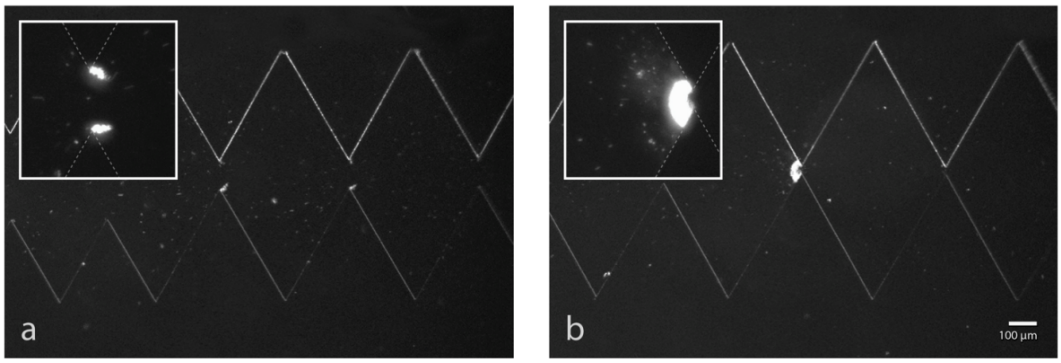

Figure 3.5. Cell capture in a narrow channel segment. (a) In Type 2 capture, material collects near the apices of the PDMS teeth while other cells and particles continue to flow unhindered from left to right. The gate width shown here is 97 µm. Inset shows a magnified view. (b) In Type 1 capture, cells are captured upstream of the gate. After several minutes of collection a plug forms and saturates the gate. Farther upstream, cells continue to flow towards the outlet, until they reach the saturation site. The gate width shown here is 27 µm. Inset shows a magnified view.

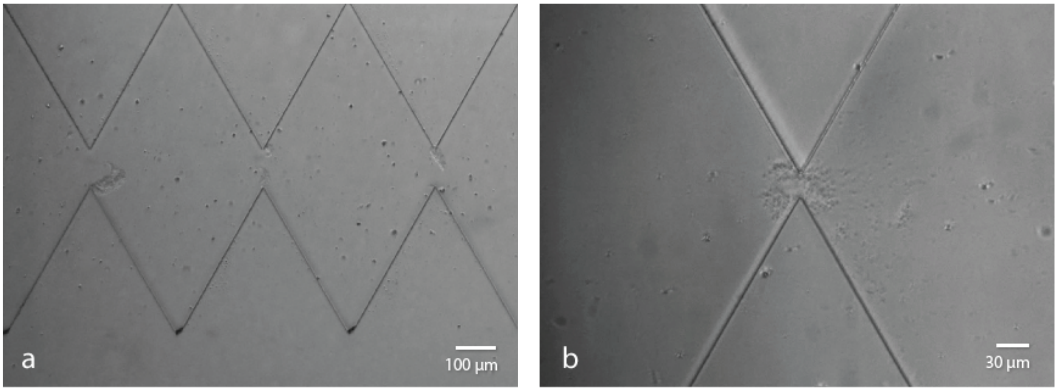

Figure 3.6. Capture of unlabeled (dye-free) cells. (a) Type 2 capture is observed with an unstained blood sample at 90-µm gates. The refractive index of cells and biomaterials differs from that of the surrounding medium, allowing visualization with simple bright field microscopy. (b) Saturation of a 27-µm gate is shown under similar conditions.

Unstained blood samples were used to determine the effect of carbocyanine dye (Vybrant DiO) on DEP capture in these samples. Bright field microscopy was used to verify that both Type 1 and Type 2 capture occurred with unstained samples, when all other factors were held constant (Fig. 3.6).

The voltage-dependence of capture was investigated by varying ΔV_{global} in multiple trials (Fig. 3.7). Capture was most evident and reproducible when ΔV_{global} ranged between 500 and 600 V. At lower potentials capture zones appeared to destabilize or shift downstream (towards the outlet). Type 1 capture of whole cells was only observed when ΔV_{global} exceeded 200 V. Below this value, no Type 1 capture was observed, and Type 2 capture shifted down-channel from the 97 μm gates to the 27 μm gates. At higher potentials RBCs were more prone to rupture and fragment.

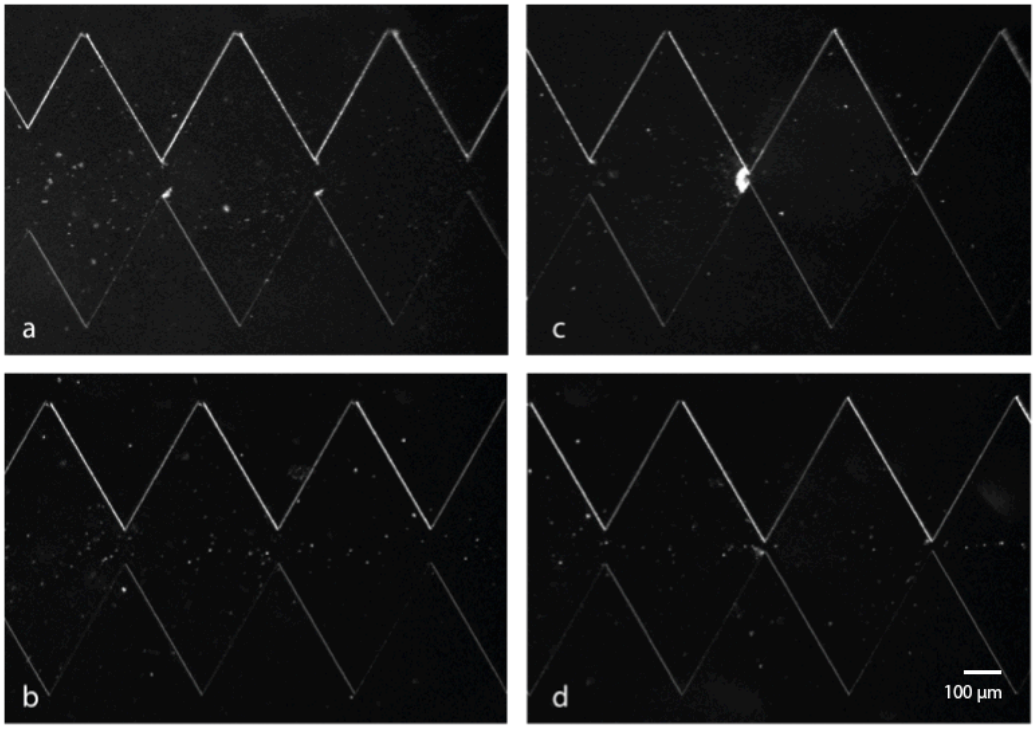

Figure 3.7. Differences in cell capture based on global potential and gate width. (a) 550 V. Type 2 capture is observed at 90-μm gates. (b) 200 V. At lower potentials, no capture is observed at 90-μm gates. (c) 550 V. Type 1 capture has caused cells to accumulate at a 27-μm gate, contributing to near-saturation of that gate. (d) 200 V. At lower potentials, no type 1 capture was observed. Type 2 capture, however, now occurs at the 27-μm gates. t = 15 min for all images.

In many experiments, the abundance of small particles moving down-channel from the inlet reservoir increased with time. After 10 to 15 minutes at high ΔV_{global}, the aggregates grew large enough to plug the first 27 μm gate. Saturation, or complete blockage in this manner, led to the rapid, non-specific accumulation of solid material at that gate. This effect was investigated further by lysing RBC samples in a hypotonic buffer solution prior to microfluidic analysis. Dynamic light scattering revealed that the mean fragment size after buffer-induced hemolysis was approximately 2.5 μm, compared to a mean diameter of 6 – 8 μm for whole RBCs. Experimental surveillance of these samples at field potentials of 500 to 600 V yielded results consistent with Type 2 capture. No Type 1 capture was observed (Fig. 3.8).

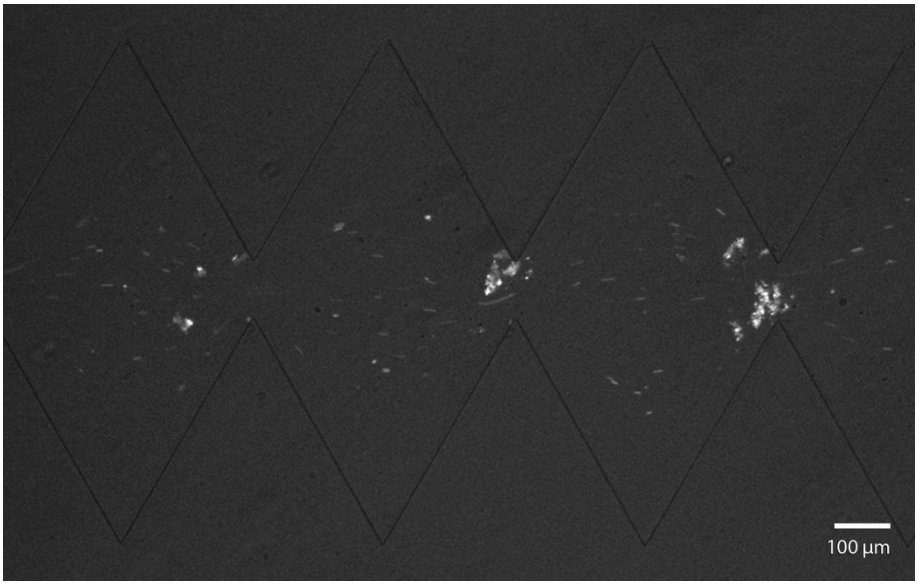

Figure 3.8. Capture of pre-lysed RBCs. Fluorescence microscopy of RBC fragments in the microchannel revealed trapping and aggregation of particles consistent with Type 2 capture. Dynamic light scattering established a mean initial particle diameter of 2.5 μm.

3.4 Discussion

The use of DC fields to drive particle motion within a shaped insulating (glass or PDMS) microstructure gives rise to complex phenomena. According to basic DEP theory as discussed in Chapter 2, three primary variables are relevant for simple spheres in a DC field: the gradient of the square of the electric field ($\boldsymbol{\nabla}|\boldsymbol{E}|^2$), the particle radius, and the conductivities of the particle (σ_p) and medium (σ_m) [19]. DEP force is proportional to the former two variables, while the sign of the resulting vector force is described by the Clausius-Mossotti relation, a mathematical term describing the relative conductivities of particle and medium. Depending on the conductivity of the particle and its surrounding medium, the DEP force will either be oriented in the direction of increasing or decreasing field strength. This describes positive dielectrophoresis (pDEP) and negative dielectrophoresis (nDEP), respectively. For small particles, EP force is proportional to a particle's net surface charge and the electric field strength. At physiological pH RBCs have a net negative charge, so EP force will be directed along field lines towards the positive electrode [20]. The negatively charged surfaces of glass and oxidized PDMS will cause EOF directed towards the negative electrode. In channel configurations with low Reynolds number, EOF also follows electric field lines [21]. Under these experimental conditions, EOF contributes more significantly to translational forces than EP. This is consistent with the observed motion of particles towards the outlet reservoir, which houses the negative electrode. Furthermore, particles distant from the capture zones followed scalloped pathlines similar to modeled electric field lines and contours (Fig. 3.4). Despite dominant EOF, the electrophoretic mobility (μ_{EP}) of a given particle will

still influence its behavior within the channel. Particle capture zones depend on the ratio $\mu_{DEP}/(\mu_{EO}+\mu_{EP})$ [22].

Capture of RBCs and other material correlates well with existing models [22] and basic theories of DEP. The PDMS teeth within the channel impinge locally upon the passage of current induced by the globally applied electric potential. This creates intense, local field gradients with greatest magnitude near the vertices (Fig. 3.4). An approaching particle with negative μ_{DEP} will experience a repulsive DEP force, directed away from the vertices and the transverse midline of the gate, while a particle with positive μ_{DEP} will experience an oppositely directed, attractive force. As a particle travels down-channel, it moves into and out of sequentially increasing local gradients. If a particle's μ_{DEP} is small or the gates are wide, the combined force of EP and EOF will exceed that of DEP. Under these conditions, the particle will pass the gate and travel continuously towards the device outlet. If, however, μ_{DEP} is large or the gate is sufficiently narrow, DEP can overcome the other forces, resulting in particle capture. Type 1 capture consisted of RBC trapping upstream of a given gate, indicating gradient-induced repulsion resulting from nDEP. Type 2 capture occurred at the tips of PDMS teeth, consistent with pDEP. Other researchers have demonstrated nDEP with erythrocytes in low-frequency AC fields and determined that this effect is expected when erythrocyte electrical conductivities are modeled as a single-shell oblate sphere [23]. This behavior is likely governed by the low conductivity of the RBC membrane relative to the cytosol and surrounding medium. Also observed in association with nDEP capture was the alignment of cells into short pearl chains. Pearl chain formation with RBCs has been observed in both AC and DC applications of DEP [24]; it is attributed to induced polarization of cells and subsequent

dipole-dipole interactions, along with micro-heterogeneities in the electric field created by the cells [25]. At the voltages used in these experiments, a small number of cells (typically less than 10%) passed uncaptured through the final sets of 27 μm teeth. Since these teeth create the strongest DEP traps within the device, the uncaptured cells represent a subset of the population with either lower μ_{DEP} or higher μ_{EP} than the others. Such electrokinetic variability can be attributed to slight differences in the physical properties of RBCs such as size, rigidity, or the expression of surface proteins.

Repeated trials with varied electric field strength demonstrated that appreciable capture only occurs above a certain threshold voltage. The magnitude of local electric field strength is proportional to the globally applied potential, and inversely proportional to the cross-sectional area of the channel. Altering ΔV_{global} will change local magnitudes of $\boldsymbol{\nabla}|\boldsymbol{E}|^2$ and the resulting DEP force. When ΔV_{global} was less than 200V, dielectrophoretic force was insufficient to effectively capture cells and cell fragments. Perhaps more interesting was an apparent shift of capture up- or down-channel with a respective increase or decrease in ΔV_{global}. pDEP capture, for example, was observed at 90 μm gates when ΔV_{global} exceeded 500 V, but occurred exclusively at 27 μm gates as ΔV_{global} approached 200 V.

Most experiments were visualized via fluorescence microscopy. Labeling the membranes of RBCs and other cells with a lipophilic carbocyanine dye (Vybrant DiO) facilitated convenient detection and monitoring. While the dye molecules are positively charged, control experiments with unlabeled blood and RBC samples established that capture was not dependent on the inclusion of intercalated dye molecules within whole or fragmented cell membranes.

Localized accumulation of bioanalyte was typically evident within one minute of ΔV_{global} application. Selective accretion usually continued for 10 to 15 minutes, until enough material had collected to span the width of the channel. Continued buildup at such saturation points was presumed to be non-specific, and indicated that the blockage site was still permeable to aqueous buffer, since upstream particle motion was still consistent with EOF-driven bulk flow. These results are promising, since selective and localized capture occurred within a short time-scale. At the voltages used in these experiments, RBCs began to lyse after five to ten minutes of continuously applied potential. Observed via fluorescence, lysis was noted by observing a marked decrease in fluorescence intensity of the particulates associated with erythrocyte morphology, accompanied by the appearance of increasingly abundant debris and small fragments. Lysis always began at the narrow end of the channel taper then gradually progressed upstream. Under certain conditions an erythrocyte's membrane may be perforated or torn while retaining some of its overall physical structure. Once the bilayer integrity has been compromised and the cytoplasm is lost, the remaining shell is referred to as a ghost [26]. RBC ghosts and other cell fragments exhibited different electrokinetic behavior than intact RBCs—they were both more likely to participate in pDEP capture. Another distinction was the greater degree of particle aggregation observed in this scenario. Whole cells appeared to engage primarily in nDEP capture. Very little particle aggregation occurred apart from pearl chain formation. Cells captured in this manner had not simply adhered to the glass or PDMS surfaces, which was confirmed by observing their release from capture zones upon removal of applied electric field.

Cell lysis may have resulted from Joule heating resulting from the use of relatively high-conductivity buffers and a low heat transfer configuration, compared to other electrophoretic techniques [27, 28]. Greater electrical resistance across the narrowest gates induces concentrated power dissipation, resulting in local heating in this section of the channel and forming a longitudinal temperature gradient, somewhat offset by the high surface-area-to-volume ratio of these sections. This local heating provides one possible explanation for the progressive lysis of RBCs as they move down-channel. If Joule heating does indeed cause or contribute to the destruction of cells, these effects might be ameliorated by the use of low-conductivity zwitterion buffers or altered heat dissipation strategies [14]. Since EOF appeared to be a strong contributor to overall fluid velocity within the channel, reducing the zeta potential of the channel walls will also reduce the field strength required for particle capture [29]. Dynamic surface coatings can decrease the electric field strength required for particle capture, while maintaining the biocompatible nature of iDEP-based techniques [30].

Methods for isolating or selectively staining WBCs and platelets were not pursued for this study. Instead we focused on capturing a single analyte (RBCs) from a complex biological fluid in the form of diluted whole blood. Favorable comparisons were observed between samples enriched for RBCs, and samples in which no such enrichment occurred. Trials with human serum samples further established that the ability to capture RBCs was not dependent on the presence or absence of other fluid components such as serum proteins or cofactors. Spatially resolved separation of blood's distinct cellular components within a single channel may be possible with iterative modeling and design improvements. Optimization of channel geometry, surface treatments, and buffer

composition all promise to augment the bioseparatory power of this technique. Other promising results have been generated in this laboratory, including the capture of bacteria [7], fluorescent microspheres [16], and amyloid Aβ protein fibrils [31].

3.5 Conclusion

The strategy investigated here exploited specific insulator geometry and a DC field to facilitate capture of RBCs from samples of human blood. This work demonstrates the first known capture of RBCs using insulators and DC fields. Electric field modeling demonstrated that capture zones coincided with areas of high DEP force. Future experiments with g-iDEP microchannels will pursue separation of bioanalytes found in complex, naturally heterogeneous fluids. Future applications could include isolating pathogens from blood or identifying variants within a single cell type (such as RBCs).

Refinement of the physical characteristics of the device will lead to the development of clinical bioanalytical tools. The simple glass-PDMS construction used here demonstrates that favorable results can be obtained with DC fields and inexpensive, disposable materials. Treatment with surface coatings to modulate EOF (and reduce fouling) will likely improve results further. In the future, engineering of DC-based microdevices may eliminate the need for bulky power supplies and allow construction of portable, battery-operated diagnostic tools.

3.6 References

[1] Sherwood, L., *Human Physiology: From Cells to Systems 7th Ed.,* Brooks/Cole, Belmont 2010.

[2] Zuckerman, K. S., *Cecil Medicine 23rd Ed.,* Saunders, Philadelphia 2007.

[3] Greer, J. P., Foerster, J., Rodgers, G. M., Paraskevas, F., Glade, B., Arber, D. A., Means, R. T. (ed), *Wintrobe's Clinical Hematology 12th Ed.,* Lippincott Williams & Wilkins, Philadelphia 2008.

[4] Toner, M., Irimia, D., *Annu. Rev. Biomed. Eng.* 2005, *7*, 77–103.

[5] Meighan, M. M., Staton, S. J. R., Hayes, M. A. *Electrophoresis* 2009, *30*, 852–865.

[6] Cabrera, C., Yager, P., *Electrophoresis* 2001, *22*, 355–362.

[7] Pysher, M. D., Hayes, M. A., *Anal. Chem.* 2007, *79*, 4552–4557.

[8] Srivastava, S. K., Daggolu, P. R., Burgess, S. C., Minerick, A. R., *Electrophoresis* 2008, *29*, 5033–5046.

[9] Lapizco-Encinas, B., Simmons, B., Cummings, E., Fintschenko, Y., *Anal. Chem.* 2004, *76*, 1571–1579.

[10] Lapizco-Encinas, B. H., Rito-Palomares, M., *Electrophoresis* 2007, *28*, 4521–4538.

[11] West, J., Becker, M., Tombrink, S., Manz, A., *Anal. Chem.* 2008, *80*, 4403–4419.

[12] Gascoyne, P., Satayavivad, J., Ruchirawat, M., *Acta Trop.* 2004, *89*, 357–369.

[13] Baylon-Cardiel, J. L., Lapizco-Encinas, B. H., Reyes-Betanzo, C., Chavez-Santoscoy, A. V., Martinez-Chapa, S. O. *Lab Chip* 2009, *9*, 2896–2901.

[14] Gagnon, Z., Gordon, J., Sengupta, S., Chang, H. C., *Electrophoresis* 2008, *29*, 2272–2279.

[15] Mack, C., *Fundamental Principles of Optical Lithography: The Science of Microfabrication,* Wiley, Chichester 2007.

[16] Staton, S. J. R., Chen, K. P., Taylor, T. J., Pacheco, J. R., Hayes, M. A., *Electrophoresis* 2010, *31*, 3634–3641.

[17] Turgeon, M. L., *Clinical Hematology: Theory and Procedures 4th Ed.,* Lippincott Williams & Wilkins, Philadelphia 2004.

[18] Hendry, E., *Clin. Chem.* 1961, *7*, 156–164.

[19] Pohl, H. A., *Dielectrophoresis: The behavior of neutral matter in nonuniform electric fields,* Cambridge University Press, Cambridge 1978.

[20] Jan, K., Chien, S., *J. Gen. Physiol.* 1973, *61*, 638–654.

[21] Cummings, E. B., Griffiths, S. K., Nilson, R. H., Paul, P. H., *Anal. Chem.* 2000, *72*, 2526–2532.

[22] Chen, K. P., Pacheco, J. R., Hayes, M. A., Staton, S. J. R., *Electrophoresis* 2009, *30*, 1441–1448.

[23] Pethig, R., *Biomicrofluidics* 2010, *4*, 022811.

[24] Minerick, A., Zhou, R., Takhistov, P., Chang, H., *Electrophoresis* 2003, *24*, 3703–3717.

[25] Wong, P., Wang, T. H., Deval, J. H., Ho, C. M., *IEEE/ASME Trans. on Mechatronics* 2004, *9*, 366–376.

[26] Mohandas, N., Gallagher, P. G., *Blood* 2008, *112*, 3939–3948.

[27] Grushka, E., McCormick, R. M., Kirkland, J. J., *Anal. Chem.* 1989, *61*, 241–246.

[28] Tang, G. Y., Yan, D. G., Yang, C., Gong, H. Q., Chai, C. J., Lam, Y. C., J. *Phys.: Conf. Ser.* 2006, *34*, 925–930.

[29] Martinez-Lopez, J. I., Moncada-Hernandez, H., Baylon-Cardiel, J. L., Martinez-Chapa, S. O., Rito-Palomares, M., Lapizco-Encinas, B. H., *Anal. Bioanal. Chem.* 2009, *394*, 293–302.

[30] Davalos, R. V., McGraw, G. J., Wallow, T. I., Morales, A. M., Krafcik, K. L., Fintschenko, Y., Cummings, E. B., Simmons, B. A., *Anal. Bioanal. Chem*. 2008, *390*, 847–855.

[31] Picou, R., Moses, J. P., Wellman, A. D., Kheterpal, I., Gilman, S. D. *Analyst* 2010, *135*, 1631–1635.

CHAPTER 4

DIFFERENTIATION OF *ESCHERICHIA COLI* SEROTYPES USING DC GRADIENT INSULATOR DIELECTROPHORESIS

4.1 Introduction

It is believed that over 10^{30} bacteria live on planet Earth and their biomass may exceed that of all other organisms combined [1]. The average human intestine is home to about 10^{14} bacteria—a microbiome composed of 500-1000 individual species [2]. Bacteria in the environment, of course, represent an even more complex array of species and niches. Typically these organisms are commensal or mutualistic, conferring some benefit to each other or their host. Some species, however, are pathogenic. Most strains of *Escherichia coli*, for instance, are innocuous to humans. However as news headlines often note, some can cause intoxication and infection where resulting syndromes may lead to death.

Relatively little is known about the immense diversity of species comprising the gut flora that crowds the human intestine. Many species remain unknown since most identification strategies require culturing—the growth of particular species in artificial environment—and many species will not accommodate this strategy. False negatives have been documented to reach at least seventy percent when conventional microbiological culture is used alone [3-5].

In practical settings, bacteria are identified by molecular and microbiologists, who use an ensemble of tests to accomplish this task. Species and strains are identified and grouped by phenotypic characteristics such as appearance and immunologic reactivity, and genotypic characteristics. Specific examples of tests used for classification include

differential staining, selective culturing, serological typing, nucleotide sequence recognition, and flow cytometry [6]. Many of these methods require preparation and growth of cultures, which significantly extends the time required for analysis. Culturing also reduces the possibility of determining the abundance or population diversity of microbes in the original sample. While nucleic acid amplification methods minimize or eliminate the need for culturing, DNA isolation and purification can be laborious. Emerging commercial approaches involving rapid PCR may reduce the time and preparation required for such tests, but involve benchtop instruments, only detect previously identified targets for which sequences are established, and typically only screen for panels of very common pathogens. As such, these approaches do not lend themselves to the development of rapid and broad field-based analysis [7].

A separations-based strategy for isolating and concentrating intact microorganisms could offer significant benefits over traditional approaches. Rapid identification and quantitation could provide revolutionary benefits in scientific, clinical, and environmental applications. A number of scientists, for over fifty years, have recognized that different cells have unique electrical properties and furthermore that those properties can be detected and used to initiate separations between different types of cells. Early work focused on sensing unique resistive and dielectric properties via impedance spectroscopy. These works often investigated the electric properties of single species by applying an alternating potential across the cells and recording current with respect to frequency [8-10]. Others attempted to bifurcate samples into two analyte populations (e.g. leukemic cells and erythrocytes) [11-14]. This research defined many unique and quantifiable differences between bacteria and many other types of cells.

A number of researchers have pursued capillary electrophoresis (CE) of microorganisms [15]. However, designing such a separation scheme faces many hurdles. As targets for analytical separations, bacteria and other microbes are both attractive and uniquely challenging. After several years developing novel approaches to CE of bacteria, Armstrong et al. identified a few of the chief difficulties involved with bacterial CE separations. These include long separation times, poor specificity, sensitivity of the analyte to the surrounding analytical environment, requirements for sample purity, and microbe aggregation [16]. CE separations of bacteria have yielded interesting results, but are typically plagued by band broadening. This decreases selectivity and separation efficiency. Armstrong et al. introduced the use of poly(ethylene oxide) (PEO) as a dynamic additive in bacterial separations. This dramatically increased apparent separation efficiency, however, peak purity was not assessed and the narrow peaks were determined to result from microbial aggregation.

Innovations using mass spectrometry (MS) provide an interesting alternative route to microbe identification. MS is typically used to identify small and large molecules. Identification of cells involves breaking them into ionized molecular fragments and measuring mass/charge ratio of the products. Cells can be identified by the characteristic fingerprint they produce in such analyses. Mass-spectrometry faces many challenges, however, including the need for sample purity, broad chemical differences in cell species, and variations between stages of cell development.

Recent electrokinetic (EK) approaches to the manipulation and analysis of microbes and other cells have demonstrated the potential for significant improvements over traditional methods. As discussed in previous chapters, dielectrophoresis (DEP)

offers tantalizing benefits in the form of extremely rapid and specific separations that can occur while simultaneously concentrating the analyte. Electrokinetic and dielectrophoretic traits can vary widely between cells and microbes that otherwise appear and behave similarly.

Using a sawtooth g-iDEP microchannel, our group is refining the separation of bacterial species and strains based on their physical and electrical properties. The work presented here is unique for three reasons. First, it uses a linear separation mode combining electrophoresis, electroosmotic flow, and dielectrophoresis, where a distinctive balance point can be found for an analyte based on the ratio of its electrokinetic mobility (the sum of electrophoretic and electroosmotic mobilities) and dielectrophoretic mobility. Second, it is an extremely high-resolution separation scheme, better than many traditional electrophoretic and dielectrophoretic strategies. Third, we demonstrate that individual strains of *E. coli* can be differentiated. This suggests an opportunity to begin to identify bacteria by their electric properties. Specifically, this work indicates that three serotypes of *E. coli* can be differentiated within an appropriately designed g-iDEP microchannel, including differentiation of pathogenic from non-pathogenic types.

4.2 Materials and Methods

4.2.1 Microdevice Fabrication

The geometry of the sawtooth channel, as well as the soft-lithographic fabrication process used for these experiments has been described previously in Chapter 3. For these experiments, however, PDMS casts were oxidized with oxygen plasma in a Tegal asher

(PlasmaLine 411, Tegal Corporation, Petaluma, CA) before bonding with the glass coverplate.

4.2.2 Cell Culture and Labeling

Three strains of *Escherichia coli* were obtained including serotypes O157:H7, strain 465-97; O55-H7; and a quality control strain O6:K1:H1, equivalent to ATCC 25922. Each strain represents a different serogroup, and will be referred to by serotype only.

E. coli seed stock was stored on biobeads in Brucella Broth with 10% glycerol at -80°C. Ten-mL aliquots of sterile lysogeny broth (LB) (Sigma-Aldrich Co., St. Louis, MO) were placed in culture tubes. Each tube was inoculated with one of the strains then incubated overnight at 37°C. This allowed each culture to reach late log phase, with a cell concentration of approximately 10^9 cells/mL. Following incubation, 500-µL aliquots of each cell culture were centrifuged at 4000 g for 3 minutes. The supernatant was discarded and the cell pellet resuspended by adding 1 mL 2 mM phosphate buffer at a pH of 7.4 and mixing with a vortexer for 10-15 seconds. This process was repeated two more times in order to wash the cells and remove the LB broth.

Cells were labeled using Vybrant DiO fluorescent dye (Invitrogen) [17-19]. The excitation and emission wavelengths for this dye are 484 and 501 nm, respectively. A 5-µL aliquot of dye was added to each 1-mL suspension of washed cells. These were incubated in a 37°C water bath for approximately 20 minutes. The samples were then washed three times in order to eliminate free dye. This was accomplished by centrifuging and resuspending the cells in phosphate buffer as described above, with the exception that the final buffer solution contained 4 mg/mL bovine serum albumin (BSA). Throughout

the labeling process, exposure to ambient light was minimized in order to prevent photobleaching. Examination of the dispersed, suspended cells using a microscope revealed that they were individual, intact cells, with minimal aggregation.

4.2.3 Experimental

The microdevice was placed on the stage of an Olympus IX70 inverted microscope with a ×4 or ×10 objective for observation and data collection. Samples were introduced into the microdevice by pipetting ~ 20 μL of cell suspension into the inlet reservoir. Hydrodynamic flow was balanced by pipetting a similar volume of buffer into the outlet reservoir (Fig. 4.1). Particle motion within the channel was observed in order to monitor and ensure stasis of flow. A mercury short arc lamp (H30 102 w/2, OSRAM) was used for illumination. An Olympus DAPI, FITC, Texas Red triple band-pass cube (Olympus, Center Valley, PA) was used for fluorescence microscopy. Both still images and video were collected with a monochrome QICAM cooled CCD camera (QImaging, Inc., Surrey, BC) and Streampix V image capture software (Norpix, Inc., Montreal, QC).

Platinum electrodes with a diameter of 0.404 mm (Alfa Aesar, Ward Hill, MA) were inserted through the PDMS access ports into the terminal reservoirs. They were then connected to a HVS448 3000D high voltage sequencer (Labsmith, Inc., Livermore, CA).

Bacteria were captured in both deionized H_2O (DI-H_2O) and 2 mM phosphate buffer at a pH of 7.4. The conductivities of these solutions were 55.3 and 343 μS/cm, respectively. DI-H_2O and buffer solutions also contained BSA ranging in concentration from 0 - 8 mg/mL. The experiments described here contained BSA at 4 mg/mL. DC potentials applied across the device ranged from 0 – 3000 V in 100 V increments. These

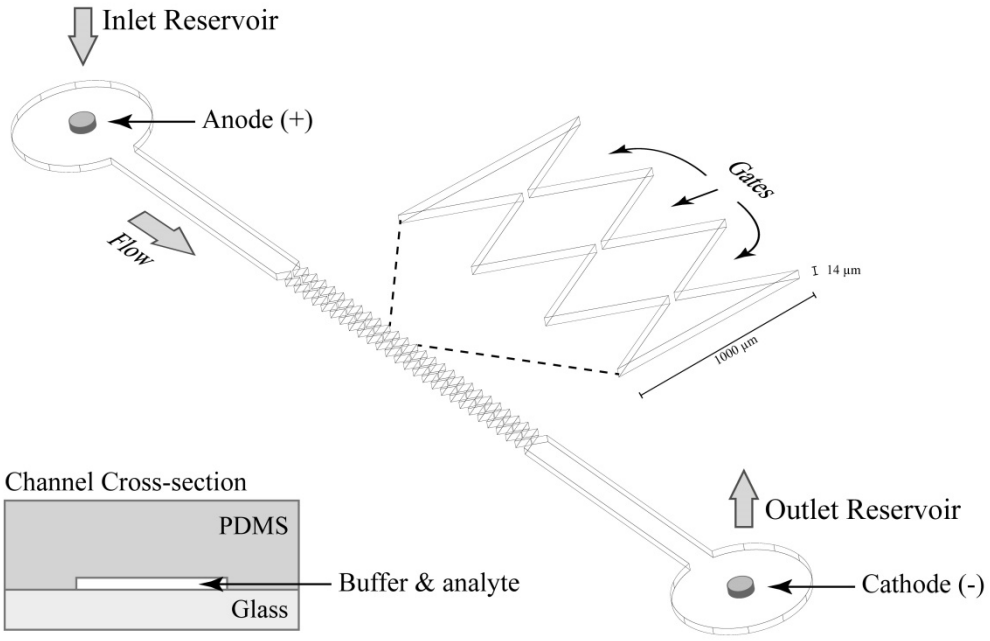

Figure 4.1. Schematic diagram of a g-iDEP microchannel. For these experiments, devices were constructed of glass and PDMS.

potentials correspond to average field strengths (E_{app} = V / 4.1 cm) of 0 – 732 V/cm and increments of approximately 24 V/cm.

Particle image velocimetry (PIV) measurements were used to determine the EK velocity of the bacteria. Cell motion was observed within the straight portions of the microchannel proximal to each reservoir. Local electric field strength was determined using COMSOL Multiphysics modeling. These values were used along with velocity data to estimate EK mobilities.

4.2.4 Mathematical Modeling

Mathematical modeling was performed for these experiments using COMSOL Multiphysics software. The parameters and process were the same as those presented in section 3.2.5 and Appendix A.

4.2.5 Safety Considerations

Organisms used in this experiment were Biosafety Level I or II. All experiments were carried out in an approved BSL II laboratory within accordance with the current version of the CDC/NIH BMBL publication.

4.3 Results

Three strains of *E. coli*, expressing O157:H7, O55:H7, or O6:K1:H1 antigenic phenotypes, with each being a different serotype, were investigated within g-iDEP devices. Their behavior was examined primarily at the final three sets of gates within the microchannel, namely those with a gate pitch of 300 μm, 90 μm, or 27 μm. Gate pitch refers to the distance between the points of opposing teeth. The magnitude of the electric potential applied across the device was recorded in terms of ΔV divided by 4.1 cm, or the overall length of the channel (E_{app}). The value of E_{app} was varied along with the duration of applied potential (t_{app}). The location of collection was noted in terms of gate pitch.

Electrokinetic and dielectrophoretic behaviors of the bacteria were broadly consistent with prior observations of other samples in g-iDEP devices. Upon application of potential, bulk motion of particles was initiated towards the outlet reservoir, which housed the cathode, consistent with expected EOF direction and charge state of bacteria [20]. No particle capture was observed in the wide-gated segments of the sawtooth channel (gate pitch > 300 μm). Within these regions, all visible material traveled consistently towards the cathode in the outlet reservoir. Capture resulted in the formation of crescent-shaped bands of concentrated particles immediately upstream of a given gate (Fig. 4.2) [21-24]. Unique capture and concentration of all three *E. coli* serotypes was observed.

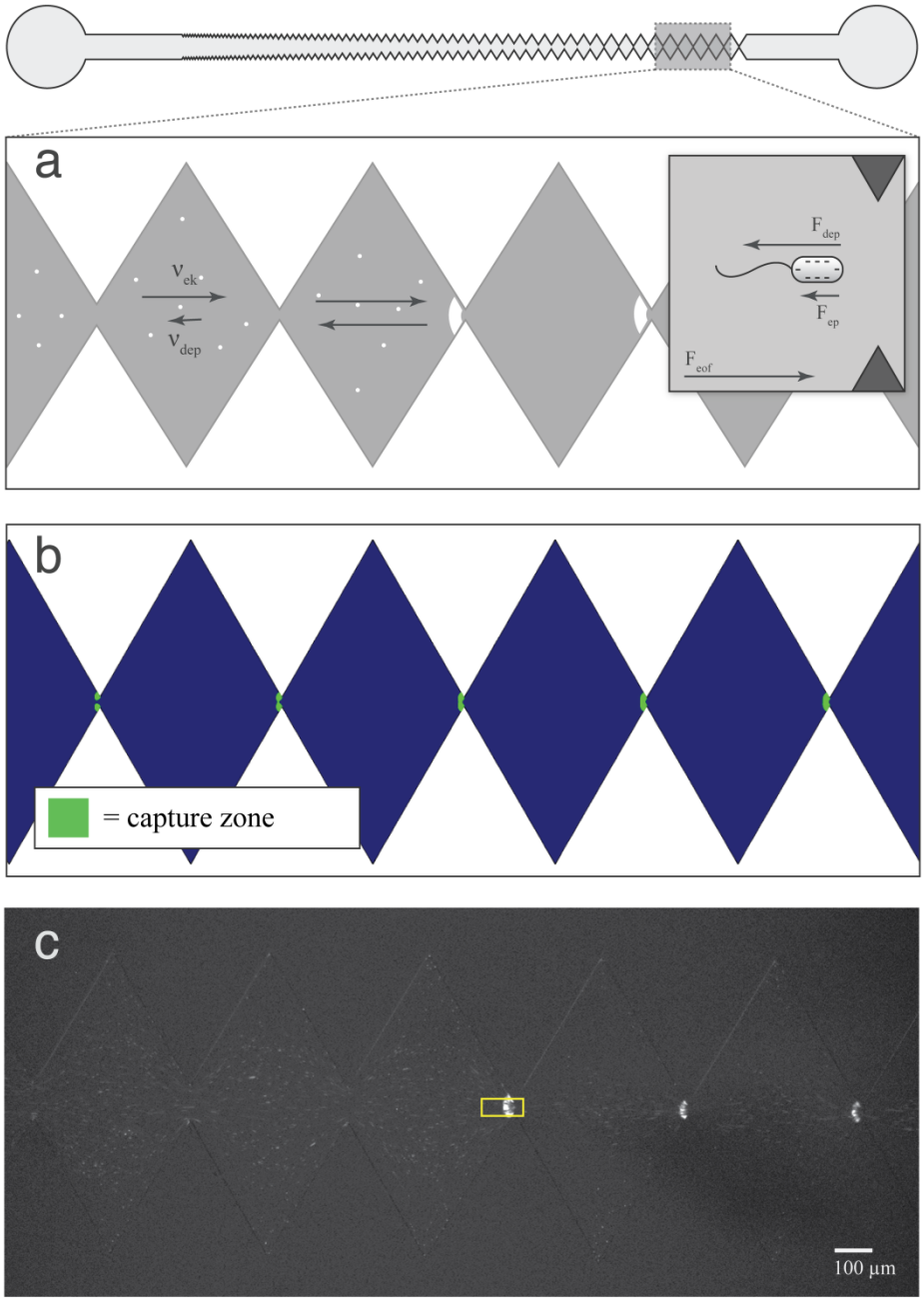

Figure 4.2. Capture of E. coli in a g-iDEP microchannel. (a) Illustration showing capture of *E. coli* organisms as predicted by the presence of opposing electrokinetic and dielectrophoretic forces. (b) An example of capture zones modeled using COMSOL Multiphysics. Appendix A contains more information regarding the modeling of capture zones. (c) Image showing capture of fluorescently-labeled bacteria. The yellow box indicates the region of interest used for fluorescence intensity measurement.

All three serotypes were captured at 27 μm gates, with statistically significant differences in E_{app} required for capture of each. Only two serotypes were captured at 90 μm gates, and one serotype at 300 μm gates. The behavior of O6:K1:H1 and O55:H7 indicate that the difference in E_{app} required for capture of different serotypes increases at larger gate pitches.

The amount of material captured at a particular gate was dependent upon the magnitude and duration of the applied electric field. Below a particular value of E_{app} no capture occurred, even over extended periods of time. That threshold value is referred to as E_{onset} and occurred after sufficient potential was applied across the device, causing particles to collect in characteristic zones near the entrance to a gate. Capture was monitored by local fluorescence intensity. Material continued to capture while potential was applied. Since collection varied with both t_{app} and E_{app}, data was collected and compared at consistent time points following application of the electric field. By holding t_{app} constant, the dependence of capture on E_{app} could be investigated. Above E_{onset}, the rate of particle accumulation increased with E_{app} (Fig. 4.3). This was observed both via qualitative image analysis and fluorescence intensity measurements.

Integrated fluorescence intensity (FI) was measured within a small region of interest (ROI) at expected capture zones. Plots of these data corresponded with qualitative observations. Specifically, measured values of FI increased rapidly with t_{app} above E_{onset} (Fig. 4.4a). FI measurements were taken at t_{app} = 5 s and plotted versus E_{app}, elucidating characteristic behaviors for each serotype at the various gate pitches. At values of E_{app} greater than E_{onset}, FI continued to increase before eventually leveling off. This yielded plots with a roughly sigmoidal shape (Fig. 4.4b).

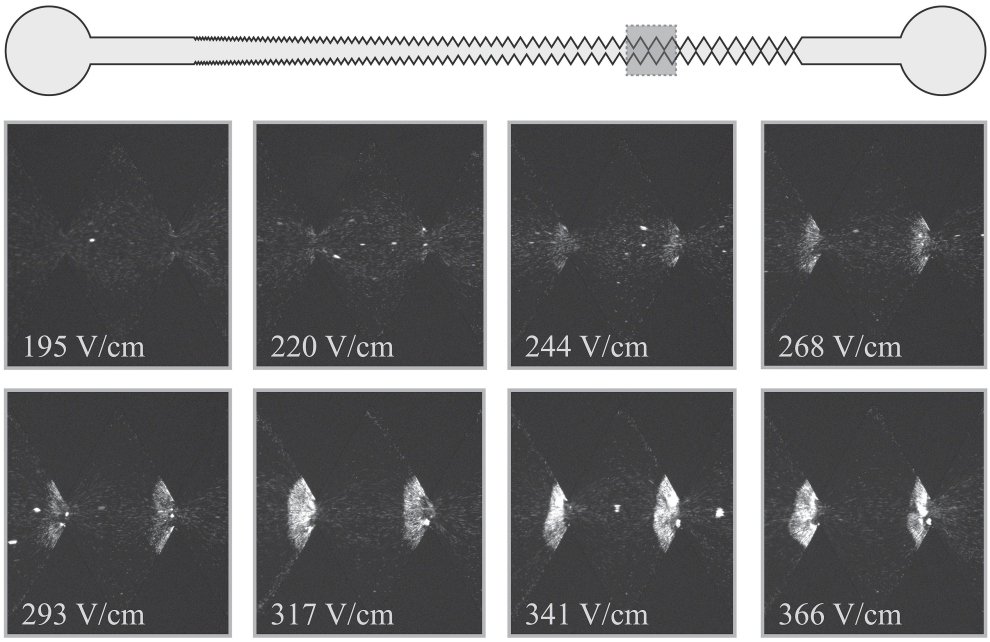

Figure 4.3. Capture of O6:K1:H1 at 90-µm gates. In each image, t_{app} = 5 seconds. Capture only occurs above a threshold value of E_{app}.

Repeated experiments demonstrated similar behavior. Fig. 4.5 shows the average integrated fluorescence intensity for data collected from five different devices with separate bacterial preparations of serotype O6:K1:H1. Error bars indicate the standard deviation of each set.

The inflection points of the sigmoidal curves shown in Fig. 4.4b were used as the serotype-specific E_{onset} values for appreciable capture. These E_{onset} values were plotted versus gate pitch for each serotype (Fig. 4.6). E_{onset} values for O6:K1:H1 were 163 ± 31, 259 ± 52, and 427 ± 53 V/cm for the 27-, 90-, and 300-µm gates, respectively. E_{onset} values for O55:H7 were 290 ± 16 and 470 ± 8 V/cm at 27- and 90-µm gates. For O157:H7, E_{onset} was 324 ± 25 V/cm at 27-µm gates. The results indicate statistically significant differences in capture behavior for the three serotypes of *E. coli* bacteria.

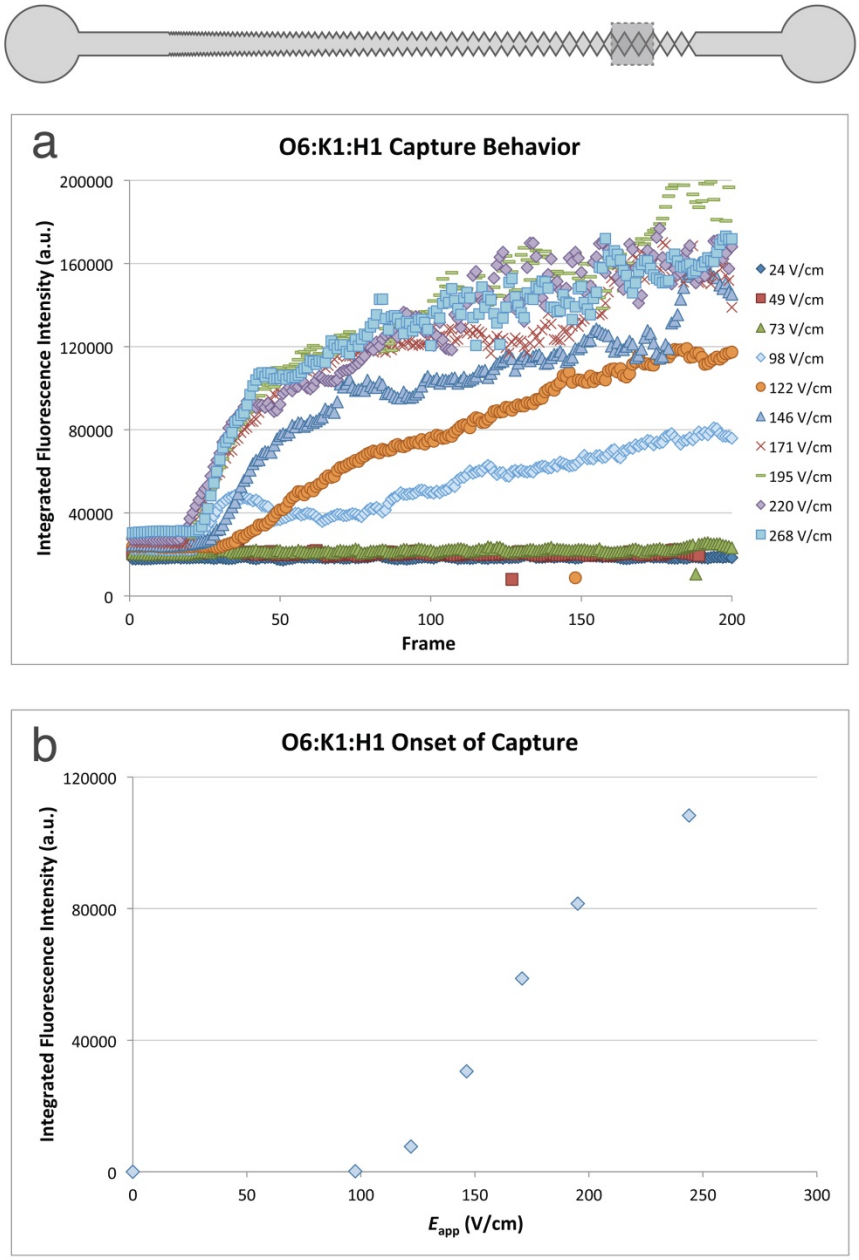

Figure 4.4. Plots showing fluorescence intensity data for capture of O6:K1:H1. (a) Plot showing the accumulation of material over time for various applied field strengths. No capture occurs when E_{app} is 100 V/cm or less, even over extended periods of time. Above this range, capture is observed almost immediately. 120 to 200 V/cm comprise a transition zone, where capture begins to occur, but is not completely exclusive. Above 200 V/cm, increasing the applied field strength does not appreciably affect the accumulation of material with time. (b) Plot showing fluorescence intensity increase at a capture zone (gate) versus applied field strength. Each FI measurement was taken after 5 seconds of applied potential.

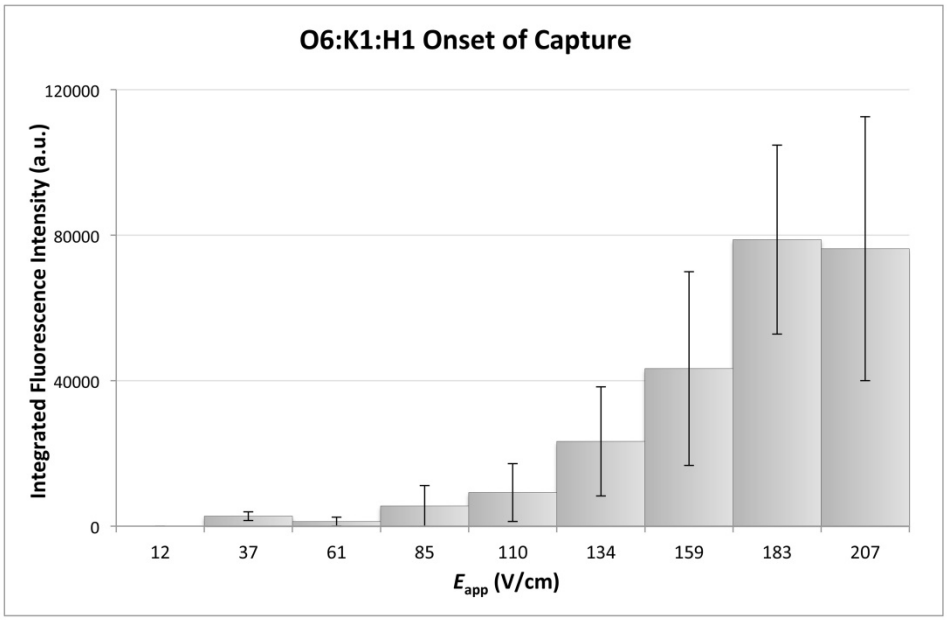

Figure 4.5. Plot showing FI intensity versus applied field strength for five different preparations of serotype O6:K1:H1, each captured on a separate device.

Unstained samples of each E. coli serotype were also used on microdevices and observed using a combination of brightfield and darkfield microscopy. Capture data from these runs agreed identically with that obtained using fluorescently-labeled samples, suggesting that the electrokinetic effects of the membrane-intercalating dye were negligible within the framework of this application.

4.4 Discussion

In order to understand behavior of these species in a g-iDEP microchannel, it's instructive to briefly consider their physicochemical characteristics. The cell surface of gram-negative bacteria such as *E. coli* typically consists of various phospholipids, membrane proteins, and a lipopolysaccharide (LPS) coat [25]. The lipopolysaccharide layer on the outer leaflet of the *E. coli* membrane (associated with the O antigen) is

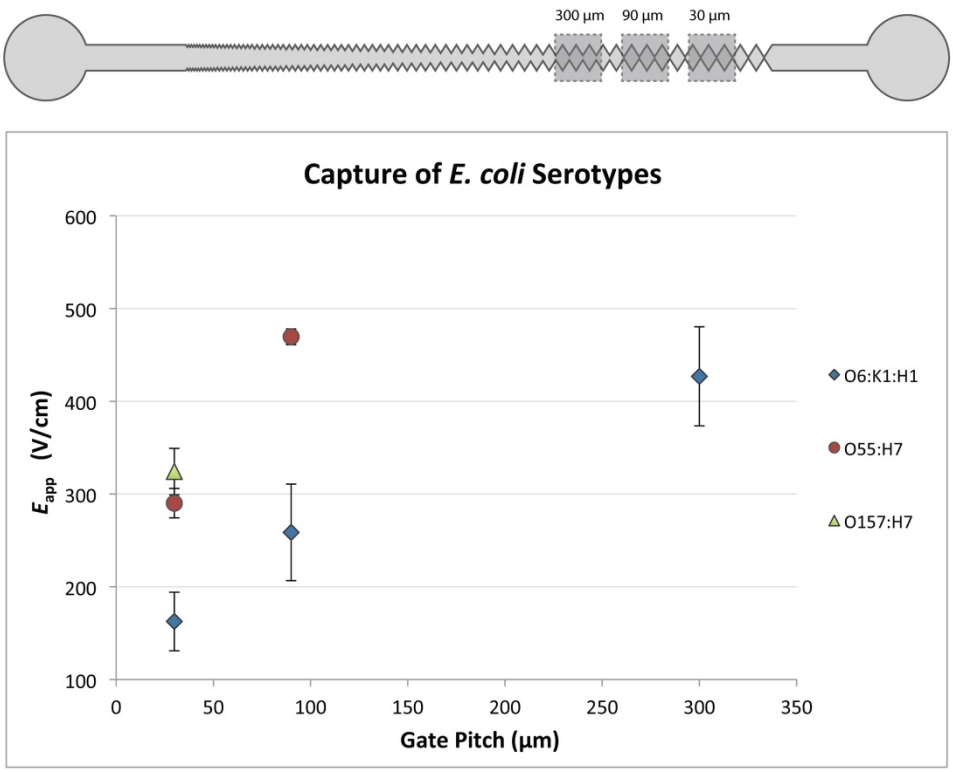

Figure 4.6. Onset field required for capture for all three serotypes of *E. coli*, at three different gate pitches (27, 90, and 300 µm). Onset field differs for all three serotypes, indicating that they can be differentiated based on their electrokinetic behavior within a g-iDEP device. The data marker hides error bars for O55:H7 at the 90-µm gates.

expected to contribute significantly to negative surface charge, due to the presence of both carboxylic acid and phosphate moieties [26]. Large-scale surface features such as flagella and fimbriae also affect the cell's surface properties [27]. Various strains of *E. coli* differ in their biochemical and physical phenotypes. Distinctions between strains can manifest in terms of protein expression, glycosylation, LPS structure, as well as differences in their flagella, fimbriae, and internal structures [28]. Considered together, these phenotypic differences can impact the charge and polarizability of *E. coli* cells, and thus contribute to different electrophoretic and dielectrophoretic mobilities.

Utilizing g-iDEP methodology presents unique opportunities to exploit these differences to generate separations. Although the complexity of biological objects like bacterial cells creates unique challenges, it also furnishes a rich set of vectors for separatory differentiation. Demonstrations of bioparticle capture using this approach have shown rapid, specific capture from heterogeneous samples

For the purposes of this discussion, EK motion refers to the transport of particles induced by the application of an external electric field. In these experiments EK transport included the effects of EP and EOF, which are both directly proportional to electric field strength. In the case of small particles, EP force is proportional to net surface charge as well as field strength. At or below neutral pH, *E. coli* bacteria possess a negative surface charge. As such, EP force will be directed toward positive electric potential. Above a pH of ~4, glass and oxidized PDMS surfaces carry a negative surface charge. This produces EOF in the opposite direction, or towards negative electric potential. In these experiments pH was maintained at 7.4. As a result, the observed motion of all bacteria towards the negative electrode indicated that under these conditions the electroosmotic mobility (μ_{EO}) exceeded the electrophoretic mobility (μ_{EP}) of the bacteria. Although dominant μ_{EO} determined the direction of transport, differences in μ_{EP} between analytes still contribute significantly to net electrokinetic mobility (μ_{EK}) and the resulting translational velocity of particles.

Electrophoretic mobilities for various serotypes of *E. coli*, including O157:H7, have been reported in the range of -0.2×10^{-4} to -1.4×10^{-4} cm^2/Vs at or near neutral pH [29]. However, these values vary with buffer pH and ionic strength. Within the g-iDEP microchannel, μ_{EP} was not measured directly. Instead, an effective estimated μ_{EK} was

determined via particle tracking. Positive values support that EOF exceeded EP force. Values of μ_{EK} determined for *E. coli* in the g-iDEP microchannel ranged from 1.2 x 10^{-4} to 2.5 x 10^{-4} cm^2/Vs.

Theoretical descriptions of dielectrophoretic behaviors of cells utilize multishell models to approximate cell structure and heterogeneity [30]. In these models, cells are treated as bodies consisting of onion-like layers with varying electrical properties. *E. coli* can be approximated as a prolate ellipsoid, with two finite-thickness shells encapsulating the cytoplasm. The outer and inner shells represent the LPS layer and cell membrane, respectively. The cytoplasm and each shell are attributed unique values for permittivity and conductivity. These models indicate that at low frequencies, including DC fields, the conductivity of the LPS layer (σ_{wall}) and cell membrane (σ_{mem}) factor significantly into the dielectric properties of the cell [31]. The dielectric properties of bacteria have yet to be precisely characterized. No alternative or independent quantitative information exists for both size and dielectric differences between strains of *E. coli*. Work performed by Castellarnau et al. using AC DEP focused on crossover frequencies of isogenic mutants of one strain of *E. coli* and further utilized a multishell model to estimate conductivities of cell cytoplasm, membrane, and wall [31]. The geometric parameters used for these calculations involved an ellipsoid with axes $a = 3/2$ and $b = a/2$, cell membrane thickness of 8 nm, and cell wall thickness of 50 nm. Using this approach, respective values for σ_{wall} and σ_{mem} were estimated to be 58 x 10^{-3} S/m and 259 x 10^{-6} S/m for *E. coli* strain 5K. These conductivities are expected to vary significantly between strains of bacteria, based on their chemical makeup and protein expression profiles. Castellarnau et al. found that these values may vary by up to 70 percent for isogenic mutants of a single strain. Their

experiments demonstrated that isogenic mutants of *E. coli*, differing at one allele, express sufficiently divergent phenotypes for different dielectrophoretic behavior.

Discussions of bacterial dielectric properties typically stop short of assigning or estimating specific values for μ_{DEP}. An experimental value of μ_{DEP} can be deduced from g-iDEP data by observing that the electrokinetic ($\boldsymbol{F}_{EK}$) and dielectrophoretic forces ($\boldsymbol{F}_{DEP}$) balance at the noted gate for the appropriate E_{onset}. Thus μ_{DEP} was calculated using the experimentally-determined value of μ_{EK}, along with modeled values of the relevant local electric field characteristics. This estimation was only calculated for the serovar that was captured at all three gates, O6:K1:H1, and resulting a value of $-1.4 \pm 0.9 \times 10^{-17}$ m^4/V^2s—a reasonable value compared to other particles measured in insulator dielectrophoretic systems (polystyrene, 1 micron, -2×10^{-16} m^4/V^2s) [32]. This mobility can be used along with the local electric field strength to estimate the magnitude of the focusing forces exerted upon a single captured bacterium. For E_{onset} at a 27 μm gate COMSOL Multiphysics modeling indicated centerline values of $\nabla|\boldsymbol{E}|^2$ were approximately 1.0×10^{15} V^2/m^3. For this calculation, an *E. coli* cell was treated as a prolate ellipsoid with major axis $a = 2$ μm and minor axis $b = 0.5$ μm. Using these assumptions and calculated values, the force is approximately 0.2 nN ($\boldsymbol{F}_{EK} \leq -\boldsymbol{F}_{DEP} = 2 \times 10^{-10}$ N).

The general features of the observed capture of *E. coli* in a sawtooth g-iDEP device are consistent with previous results obtained using cells and other bioparticles. The characteristic behaviors have been described in detail elsewhere [21].

The local magnitudes of $\nabla|\boldsymbol{E}|^2$ and the resultant trapping DEP force are a function of both E_{app} and gate pitch. The dependence of capture on E_{app} and gate pitch was observed for all three serotypes (Fig. 4.6). A difference in E_{app} required for capture at a

given gate between any two particle types indicates that they possess either differing μ_{EK}, μ_{DEP}, or both. A sufficient difference in these factors indicates that two particles could be differentiated.

When E_{app} was less than 100 V/cm, dielectrophoretic force was insufficient for capture of any cells. Capture at field strengths less than this value would require either a smaller gate pitch or a reduction in EK velocity. The latter could potentially be achieved by a reduction in EOF. Values of E_{app} above approximately 730 V/cm were unattainable due to equipment constraints. This represents the maximum potential of 3000 V that could be applied to the channel using the existing power supply. Application of higher potentials is also impractical due to excessive joule heating, which causes bubble formation within the channel, particularly where a large potential drop occurs across narrow gates.

Variables that could not be precisely controlled or quantitated, such as bacterial cell count, staining efficiency, pressure-driven and electroosmotic flow control, slightly varying properties for the individual cells, and photobleaching effects all contribute to the overall variance.

All samples were inspected at relatively high magnification before and after collection to observe the typical swimming and tumbling behaviors characteristic of the serotype. In all cases investigated, similar behaviors were observed for both conditions, suggesting that the high electric field and possible Joule heating did not negatively impact the bacteria in a significant manner. This is attributed to the relatively weak external field strength compared to local zeta potential/lipid bilayer field strength, which

are typically several orders of magnitude higher than those estimated to be present within these devices.

These results show that O157:H7, O55:H7, and O6:K1:H1 serotypes of *E. coli* can be differentiated using g-iDEP operated with DC fields. In different pathogenic and non-pathogenic *E. coli* serotypes, small differences in cell structure, membrane, and wall composition are shown to be sufficient for differentiating populations. Current literature sources offer scant quantitative data regarding physical and electrical differences between strains of *E. coli*. Strain-to-strain variations in mean size or geometry are unknown. If such variation existed, however, it could be expected to contribute significantly to differences in both electrophoretic and dielectrophoretic force. Strain-specific differences in the biochemical makeup of the cell membrane and wall are likely to affect bacterial surface charge and conductivity. These parameters will in turn yield characteristic differences in electrophoretic and dielectrophoretic force.

Although it has not been demonstrated here, it is plausible that simultaneous separation and capture of all three serotypes within a single channel is achievable. This supports the idea that this approach can be adapted for future separation and identification of similar bacteria in microfluidic devices. However, this would require restructuring the progression of gate pitch along the channel. Future efforts will evaluate the implementation and efficiency of such separations. Specifically, advancements in channel geometry and surface treatments, along with the possible use DC-offset AC fields promise to extend the abilities and applicability of this approach.

While the work presented here must adapt to the semantics of existing microbiological methods, the mechanism of identification and differentiation pursued

here differs. Large-scale, phenotypic differences arise from molecular origins, which are concomitantly associated with identifiable and characteristic variation of cellular electric properties. With sufficient separatory resolution, gradient insulator-based dielectrophoresis (g-iDEP) will enable separation of many if not all of the categories currently used by microbiologists.

4.5 Conclusion

Using a g-iDEP strategy implemented with a pattern of sawtooth insulators has demonstrated differentiation of three serotypes of *E. coli* bacteria. While previous work has shown differentiation of bacteria based on species or live/dead state, this is the first demonstration of serotype differentiation using DC fields or insulator-based dielectrophoresis. Capture behavior was consistent with electric field modeling and overlapped with capture zones predicted from negative DEP forces. The results presented here indicate that all three serotypes could be discretely captured within a single separatory channel. Further modeling and design will facilitate optimization of g-iDEP channel geometry for the separation and capture of similar bioanalytes from complex mixtures. Such improvements will aid the development of new bioanalytical tools that enable the identification of microbes through precise and rapid separations.

4.6 References

[1] Whitman, W. B., Coleman, D. C., Wiebe, W. J., *Proc. Natl. Acad. Sci. U. S. A.* 1998, *95*, 6578-6583.

[2] Hooper, L. V., Gordon, J. I., *Science* 2001, *292*, 1115-1118.

[3] Agata, E. M. C. D., Gautam, S., Green, W. K., Tang, Y.-W., *Clinical Infectious Diseases* 2002, *34*, 167-172.

[4] Benjamin, R. J., Wagner, S. J., *Transfusion* 2007, *47*, 1381-1389.

[5] Scallan, E. G., P. M.; Angulo, F. J.; Tauxe, R. V.; Hoekstra, R. M., *Emerging Infectious Diseases* 2011, *17*, 16-22.

[6] Black, J. G., *Microbiology: principles and applications*, Prentice Hall 1996.

[7] Tenover, F. C., in: Bush, K. (Ed.), *Antimicrobial Therapeutics Reviews* 2010, pp. 70-80.

[8] Suehiro, J., Noutomi, D., Shutou, M., Hara, M., *Journal of Electrostatics* 2003, *58*, 229-246.

[9] Gascoyne, P. R. C., Noshari, J., Becker, F. F., Pethig, R., *IEEE Transactions on Industry Applications* 1994, *30*, 829-834.

[10] Huang, Y., Wang, X. B., Becker, F. F., Gascoyne, P. R. C., *Biochimica et Biophysica Acta-Biomembranes* 1996, *1282*, 76-84.

[11] Becker, F. F., Wang, X. B., Huang, Y., Pethig, R., Vykoukal, J., Gascoyne, P. R. C., *Journal of Physics D-Applied Physics* 1994, *27*, 2659-2662.

[12] Becker, F. F., Wang, X. B., Huang, Y., Pethig, R., Vykoukal, J., Gascoyne, P. R. C., *Proceedings of the National Academy of Sciences of the United States of America* 1995, *92*, 860-864.

[13] Burt, J. P. H., Pethig, R., Gascoyne, P. R. C., Becker, F. F., *Biochimica Et Biophysica Acta* 1990, *1034*, 93-101.

[14] Wang, X. B., Huang, Y., Gascoyne, P. R. C., Becker, F. F., Holzel, R., Pethig, R., *Biochimica et Biophysica Acta-Biomembranes* 1994, *1193*, 330-344.

[15] Petr, J., Maier, V., *Trac-Trends in Analytical Chemistry* 2012, *31*, 9-22.

[16] Armstrong, D. W., Schulte, G., Schneiderheinze, J. M., Westenberg, D. J., *Anal. Chem.* 1999, *71*, 5465-5469.

[17] Hsiao, A. P., Barbee, K. D., Huang, X., 2010, 77590W-77590W.

[18] Preira, P., Grandne, V., Forel, J. M., Gabriele, S., Camara, M., Theodoly, O., *Lab on a Chip* 2013, *13*, 161-170.

[19] Phillips, J. A., Xu, Y., Xia, Z., Fan, Z. H., Tan, W. H., *Anal. Chem.* 2009, *81*, 1033-1039.

[20] Olitzki, L., *Journal of Immunology* 1932, *22*, 251-256.

[21] Jones, P. V., Staton, S. J. R., Hayes, M. A., *Analytical and Bioanalytical Chemistry* 2011, *401*, 2103-2111.

[22] Staton, S. J. R., Jones, P. V., Ku, G., Gilman, S. D., Kheterpal, I., Hayes, M. A., *Analyst* 2012, *137*, 3227-3229.

[23] Chen, K. P., Pacheco, J. R., Hayes, M. A., Staton, S. J. R., *Electrophoresis* 2009, *30*, 1441-1448.

[24] Pysher, M. D., Hayes, M. A., *Anal. Chem.* 2007, *79*, 4552-4557.

[25] Hamadi, F., Latrache, H., Zahir, H., Elghmari, A., Timinouni, M., Ellouali, M., *Brazilian Journal of Microbiology* 2008, *39*, 10-15.

[26] Amory, D. E., Mozes, N., Hermesse, M. P., Leonard, A. J., Rouxhet, P. G., *Fems Microbiology Letters* 1988, *49*, 107-110.

[27] El Ghmari, A., Latrache, H., Hamadi, F., El Louali, M., El Bouadili, A., Hakkou, A., Bourlioux, P., *Microbiologica* 2002, *25*, 173-178.

[28] Latrache, H., Mozes, N., Pelletier, C., Bourlioux, P., *Colloids and Surfaces B: Biointerfaces* 1994, *2*, 47-56.

[29] Lytle, D. A., Rice, E. W., Johnson, C. H., Fox, K. R., *Applied and Environmental Microbiology* 1999, *65*, 3222-3225.

[30] Pethig, R., *Biomicrofluidics* 2010, *4*.

[31] Castellarnau, M., Errachid, A., Madrid, C., Juarez, A., Samitier, J., *Biophysical Journal* 2006, *91*, 3937-3945.

[32] Weiss, N. G., Jones, P. V., Mahanti, P., Chen, K. P., Taylor, T. J., Hayes, M. A., *Electrophoresis* 2011, *32*, 2292-2297.

CHAPTER 5

DEVELOPMENT OF RESOLUTION THEORY FOR GRADIENT INSULATOR-BASED DIELECTROPHORESIS

5.1 Introduction

Effective control over the selective transport of biological material lies at the heart of medical, pharmaceutical, and environmental analytical strategies. Many existing methodologies, such as those used in clinical diagnosis are quite limited in their capabilities, at least relative to the bioanalytical challenges of modern personalized medicine. Developments of new separatory tools are needed to meet these challenges of medical diagnostics and environmental monitoring.

In many analytical separations, components become segregated as they move along a linear axis at different rates. Chromatography and zone electrophoresis serve as examples of this paradigm [1, 2]. Such methods are ultimately limited by band broadening from dispersive effects, which decrease analyte concentration throughout the process. This limits subsequent analyte detection and multi-dimensional analysis. Steady-state separation schemes, such as equilibrium-gradient techniques, employ competing forces to simultaneously concentrate and fractionate analytes. Each unique species is focused to a distinctive zero-velocity location, where the concentration distribution about that point reflects the interplay between focusing and dispersive forces. Isoelectric focusing [3], density gradient sedimentation [4], and electric field gradient focusing [5] serve as paradigmatic examples.

The quality of any separation is described in terms of resolution, an expression

that specifies separation of the centroid of the analyte concentration profiles versus the spreading of each band. Most separatory systems have been thoroughly explored theoretically and experimentally including chromatography [6, 7], capillary electrophoresis [8], isoelectric focusing [9], and electric field gradient focusing [10].

The current work is focused on developing a theoretical basis of resolution for gradient insulator-based dielectrophoresis (g-iDEP). The scheme discussed here is an amalgam of iDEP and traditional linear separation science, which represents a new approach to equilibrium-gradient separations conducive to use with any analyte from ~4 nm to 10 μm diameter and is especially useful for a large portion of, if not all bioparticulates (viruses, organelles, cells, lysosomes, vesicles, etc.). This technique, while employing local-gradient, steady-state focused bands of material, differs significantly from true global gradient techniques in that it is directional; the analytes/targets must be introduced from a single side of the device. There is no mechanism to refocus materials once past their first focus or balance point. This is an important distinction for classification of separations science and will affect certain operating paradigms, but the general advantages of gradient techniques are true for this strategy also. This technique has already demonstrated isolation and concentration of a wide range of particles, including bacteria, polystyrene spheres, red blood cells, and amyloid fibrils [11-15].

Within g-iDEP, a combination of dielectrophoretic (DEP), electrophoretic (EP), and electroosmotic flow (EOF) forces are used to transport, separate, and concentrate particles within a channel. In previous chapters, this technique was implemented using a sawtooth-patterned microchannel. It is important to note that the specific geometric

implementation of g-iDEP may vary. The theory presented here may be used for other geometric series of sequentially changing, constrictive insulating features (referred to as gates). If such features are tailored to induce appropriate amounts of force, they will cause physically distinct particles to settle into discrete zones near different gates along the channel's separatory axis (Fig. 5.1, 5.2, and 5.3).

Considered together, a particle's electrophoretic and dielectrophoretic mobilities reflect an array of properties including size, charge, polarizability, shape, and heterogeneity [16]. Interrogating all these properties together yields a separatory scheme that can be fine-tuned for high-resolution capture and concentration of analytes. This work will allow estimation of the smallest change in electrokinetic or dielectrophoretic properties that can be uniquely differentiated by g-iDEP.

Using common experimental values for field strength, gradient and particle properties, these calculations suggest that separation of targets based on 15-nm differences in 1-μm diameter particles is possible (one part in 10^2) and the smallest resolvable difference in dielectrophoretic mobility is 10^{-23} m^4/V^2s (one part in 10^4) and the smallest resolvable change in Clausius–Mossotti factor is 10^{-5}. When the highest experimentally available values are used, the smallest resolvable difference for these physical parameters are 500 pm for radius, 10^{-26} m^4/V^2s (one part in 10^7) for dielectrophoretic mobility, and 10^{-8} for the Clausius–Mossotti factor (all for a nominal one-micrometer diameter particle). This suggests that the technique promises to be an ultra-high resolution separation scheme for molecules and particles ranging from 4 nm to 10 μm in diameter.

5.2 Theory

5.2.1 Analyte behavior, transport and capture zones

Particle motion within a g-iDEP channel results from a superposition of forces induced by the applied electric field (Fig. 5.1). These forces vary predictably with the electric field and depend on electro-physical properties of the analyte. As a result, a particle's translational velocity in an electric field is described by electrokinetic mobilities intrinsic to that particle. Electrophoretic and electroosmotic forces are both proportional in magnitude and directionally coincident to the electric field and these two terms are included in an electrokinetic mobility (μ_{EK}).

$$\mu_{EK} = \mu_{EP} + \mu_{EOF} \tag{1}$$

The third electrokinetic force to consider is dielectrophoresis, characterized by dielectrophoretic mobility (μ_{DEP}). The dielectrophoretic mobility is a function of the permittivity of the solution (ε_f), particle radius (r), Clausius-Mossotti factor (f_{CM}) and solution viscosity (η) according to $\mu_{DEP} = \varepsilon_f r^2 f_{CM}/3\eta$ [17].

In order to represent the transport of target analyte along the centerline of the system, conventions provided by Giddings are used [18]. These state that transport ($\boldsymbol{w}$) is the sum of field-induced analyte velocity ($\boldsymbol{u}$) and pressure-driven fluid flow velocity ($\boldsymbol{b}$).

$$\boldsymbol{w} = \boldsymbol{u} + \boldsymbol{b} \tag{2}$$

No pressure-driven flow exists, so we consider only field-induced analyte motion. Transport or net velocity is the sum of component electrokinetic and dielectrophoretic velocity vectors for the analyte:

$$\boldsymbol{u} = \boldsymbol{v}_{EK} + \boldsymbol{v}_{DEP} \tag{3}$$

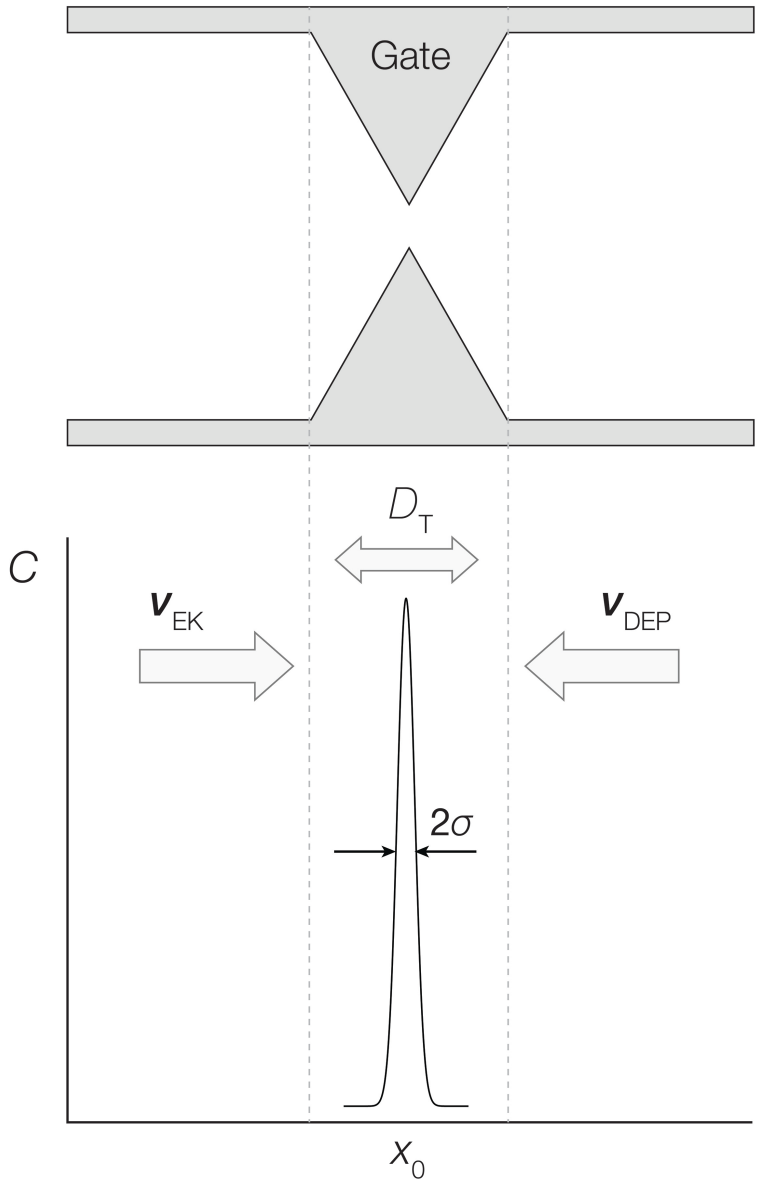

Figure 5.1. Diagram depicting concentration of analyte at a gate structure within a g-iDEP microchannel. Peak width is a function of focusing factors associated with electrophoretic velocity ($\boldsymbol{v}_{EK}$) and dielectrophoretic velocity ($\boldsymbol{v}_{DEP}$) balanced with dispersive forces including diffusion (D_{diff}).

The component electrokinetic and dielectrophoretic velocity vectors can be expressed in the following terms, which derive from the respective force equations (not shown):

$$\boldsymbol{v}_{EK} = \mu_{EK}\boldsymbol{E} \tag{4}$$

$$\boldsymbol{v}_{DEP} = \mu_{DEP}\boldsymbol{\nabla}|\boldsymbol{E}|^2 \quad (5)$$

Each of two analytes can be assigned an electrokinetic mobility (μ_{EK1} and μ_{EK2}) and dielectrophoretic mobility (μ_{DEP1} and μ_{DEP2}). For further discussion of analyte separation, we will also consider the average of the two species' electrokinetic or dielectrophoretic mobilities:

$$\bar{\mu} = \frac{(\mu_1+\mu_2)}{2} \quad (6)$$

Since transport velocity is dependent on the position of the analyte along the separatory axis, equations (3) and (4) can be written as functions of x:

$$\boldsymbol{w}(x) = [\boldsymbol{v}_{EK}(x)] + [\boldsymbol{v}_{DEP}(x)] \quad (7)$$

$$\boldsymbol{w}(x) = \mu_{EK}[\boldsymbol{E}(x)] + \mu_{DEP}[\boldsymbol{\nabla}|\boldsymbol{E}(x)|^2] \quad (8)$$

These equations hold true for any physical position along the centerline of the channel's separatory axis.

While the field and gradient are continuous throughout the system, the areas near the points of closest approach (gates) define the resolution-limiting conditions (Fig. 5.1, 5.2, and 5.3). The width of these zones and the intervening minimum gradient zones are discussed below, but these factors do not need to be considered to develop this approach. At or near one of these gates, for a specific analyte, a balance point is induced and a zone forms about this zero velocity crossover. The width of the zone will directly impact the ability to keep that material trapped at a single gate and prevent some material from moving to the next gate. The variable, x_0, is set at the center of the local capture zone. The forces and resulting velocity are conveniently related to the distance from the balance point for a particular analyte.

$$\boldsymbol{u} = -a(x - x_0) \quad (9)$$

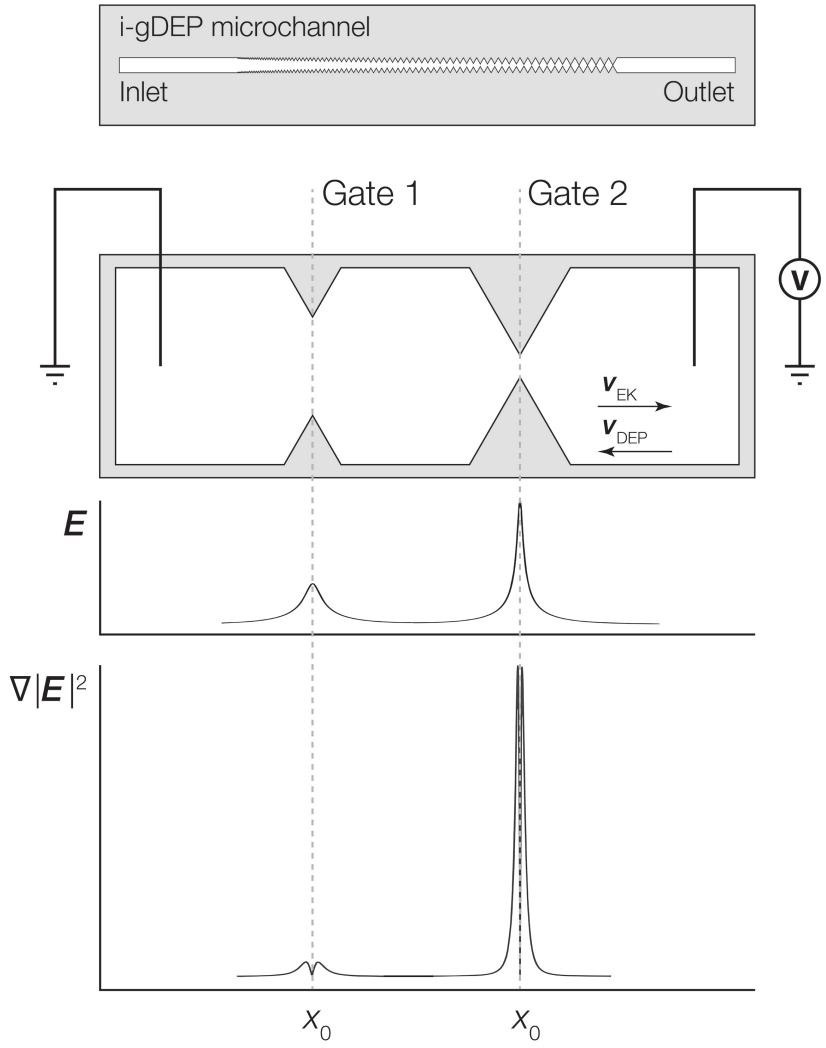

Figure 5.2. Gate and field characteristics. (top) Schematic representation of an entire g-iDEP device. (lower three panels) Detail of two gates within a g-iDEP microchannel. Below the gates are representations of the absolute magnitude of the centerline electric field strength and $\boldsymbol{\nabla|E|^2}$. The device shown here serves only illustrative purposes. Specific implementation and geometry of gates are flexible, and may be altered significantly depending on the desired application. Gates may also be operated in parallel, attaining the same resolution as expressed in this document.

The slope a represents the intensity of the local restoring forces. The a term may be treated as linear, either by assuming very small values of $x - x_0$, or by using the first non-zero factor in a Taylor series expansion about x_0 (in some cases the factor treated as linear

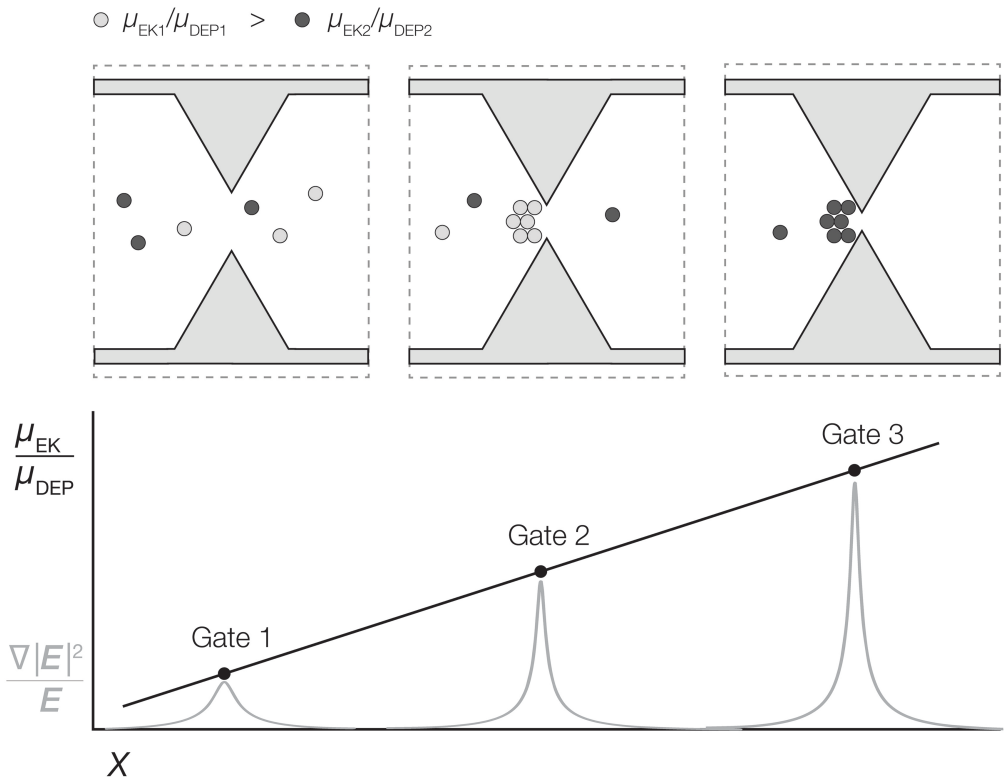

Figure 5.3. Capture of two distinct analytes. (Top) Illustration of three adjacent gates within a hypothetical g-iDEP channel. One of two target analytes is selectively captured and concentrated at the center gate. The other target analyte is captured at the gate to the right. (Bottom) Since gate pitch decreases along the channel in a determinate manner, distance is used to relate the resolvability of two target species. Note capture zones are of finite width, indicating dispersive effects including diffusion, field inhomogeneity, electrothermal effects, diffusion and particle-particle interaction.

from a Taylor series expansion is *u*; instead *a* is utilized here to avoid confusion with the velocity term expressed above). This focusing effect generates a steady-state Gaussian concentration profile around the force balance point. The characteristic width and properties of this distribution define the concentration profile for a band of material.

$$a = -\frac{d\boldsymbol{u}}{dx} = -\frac{d(\boldsymbol{v_{EK}}+\boldsymbol{v_{DEP}})}{dx} = -\left[\bar{\mu}_{EK}\left(\frac{d\boldsymbol{E}}{dx}\right) + \bar{\mu}_{DEP}\left(\frac{d\boldsymbol{\nabla}|\boldsymbol{E}|^2}{dx}\right)\right] \quad (10)$$

Furthermore, Giddings showed that the characteristic variance profile for this type of system is [18]:

$$\sigma^2 = \frac{D_T}{a} \tag{11}$$

In this case, the term D_T represents the sum of all dispersive forces, including those resulting from diffusion (D_{diff}), flow-based effects, solution heating, particle-particle interactions, and heterogeneous fields. Substituting equation 10 for a and solving for σ yields the standard deviation:

$$\sigma = \sqrt{\frac{D_T}{-\left[\overline{\mu}_{EK}\left(\frac{dE}{dx}\right)+\overline{\mu}_{DEP}\left(\frac{d\nabla|E|^2}{dx}\right)\right]}} \tag{12}$$

This expression provides a measure for the peak width of captured analyte. This construct is virtually identical to that of isoelectric focusing, adapted to the focusing forces present in g-iDEP.

5.2.2 Assigning distance between concentration centroids

Spatial segregation of two similar analytes is designated as resolution of the analytes. This is defined by the distance between the centroids of two separated species (ΔX), and their degree of spreading (σ) [19].

$$R = \frac{\Delta X}{4\sigma} \tag{13}$$

The definition of the smallest difference in analytes that can be separated on a g-iDEP device is similar to traditional techniques. There are still slightly overlapping peaks, with R > 1.5, but each peak is collected at separate, nearest neighbor gates (Fig. 5.3). Just to emphasize this point, the resolution of two species is defined as collection of one species at one gate and the other species at the next gate. A finite distance separates these gates.

This distance is used to assign differences in the maximum field and gradient at those gates, allowing for calculation in Eulerian space (focusing on static space instead of time or moving coordinates).

For any two arbitrary neighboring gates, the local maxima are defined as $\boldsymbol{E}_1$ and $\boldsymbol{E}_2$. The average of these two local maxima is $\boldsymbol{E}_{\text{ave}}$. The change between successive pairs of gates is $\Delta\boldsymbol{E}_{\text{max}} = \boldsymbol{E}_2 - \boldsymbol{E}_1$. The local maximum gradient terms are defined as $\boldsymbol{\nabla}|\boldsymbol{E}|^2{}_1$ and $\boldsymbol{\nabla}|\boldsymbol{E}|^2{}_2$. The average of these values is $\boldsymbol{\nabla}|\boldsymbol{E}|^2{}_{\text{ave}}$. The difference in this parameter between successive pairs of neighboring gates or capture zones is expressed as $\Delta(\boldsymbol{\nabla}|\boldsymbol{E}|^2)_{\text{max}} = \boldsymbol{\nabla}|\boldsymbol{E}|^2{}_2 - \boldsymbol{\nabla}|\boldsymbol{E}|^2{}_1$.

Within this context, ΔX represents the distance between capture zones of two analytes along the projected continuum of gates. This concept facilitates determination of the minimum difference in the maximum field strength and the gradient term between two gates required for analyte separation. The term Δv represents the difference in instantaneous net velocity of analytes 1 and 2 at their balance point at adjoining gates. The expression $d\boldsymbol{u}/dx$ represents the rate at which the field and gradient terms change along the channel from gate to gate.

$$\Delta X = \frac{\Delta \boldsymbol{v}}{d\boldsymbol{u}/dx} \tag{14}$$

where:

$$\Delta \boldsymbol{v} = \Delta\mu_{EK}\boldsymbol{E}_{ave} + \Delta\mu_{DEP}\boldsymbol{\nabla}|\boldsymbol{E}|^2{}_{ave} \tag{15}$$

$$\frac{d\boldsymbol{u}}{dx} = \bar{\mu}_{EK}\left(\frac{d\boldsymbol{E}_{max}}{dx}\right) + \bar{\mu}_{DEP}\left(\frac{d\boldsymbol{\nabla}|\boldsymbol{E}|^2{}_{max}}{dx}\right) \tag{16}$$

Combining these yields a complete expression for ΔX:

$$\Delta X = \frac{\Delta\mu_{EK}\boldsymbol{E}_{ave}+\Delta\mu_{DEP}\nabla|\boldsymbol{E}|^2{}_{ave}}{\overline{\mu}_{EK}\left(\frac{d\boldsymbol{E}_{max}}{dx}\right)+\overline{\mu}_{DEP}\left(\frac{d\nabla|\boldsymbol{E}|^2{}_{max}}{dx}\right)} \tag{17}$$

An equation for resolution may be expressed by incorporating equations 17 and 12 (and 13) for ΔX and combined zone width:

$$R = \frac{\Delta X}{4\sigma} = \frac{\frac{\Delta\mu_{EK}\boldsymbol{E}_{ave}+\Delta\mu_{DEP}\nabla|\boldsymbol{E}|^2{}_{ave}}{\overline{\mu}_{EK}\left(\frac{d\boldsymbol{E}_{max}}{dx}\right)+\overline{\mu}_{DEP}\left(\frac{d\nabla|\boldsymbol{E}|^2{}_{max}}{dx}\right)}}{4\sqrt{\frac{D_T}{-\left[\overline{\mu}_{EK}\left(\frac{d\boldsymbol{E}}{dx}\right)+\overline{\mu}_{DEP}\left(\frac{d\nabla|\boldsymbol{E}|^2}{dx}\right)\right]}}} = \frac{\left(\Delta\mu_{EK}\boldsymbol{E}_{ave}+\Delta\mu_{DEP}\nabla|\boldsymbol{E}|^2{}_{ave}\right)\sqrt{-\left[\overline{\mu}_{EK}\left(\frac{d\boldsymbol{E}}{dx}\right)+\overline{\mu}_{DEP}\left(\frac{d\nabla|\boldsymbol{E}|^2}{dx}\right)\right]}}{4\left[\overline{\mu}_{EK}\left(\frac{d\boldsymbol{E}_{max}}{dx}\right)+\overline{\mu}_{DEP}\left(\frac{d\nabla|\boldsymbol{E}|^2{}_{max}}{dx}\right)\right]\sqrt{D_T}} \tag{18}$$

In order to achieve baseline separation, by setting R greater than or equal to 1.5 the equation can be rearranged to solve for the minimum differences between two analytes that can still be separated. $1.5 \leq \frac{\left(\Delta\mu_{EK}\boldsymbol{E}_{ave}+\Delta\mu_{DEP}\nabla|\boldsymbol{E}|^2{}_{ave}\right)\sqrt{-\left[\overline{\mu}_{EK}\left(\frac{d\boldsymbol{E}}{dx}\right)+\overline{\mu}_{DEP}\left(\frac{d\nabla|\boldsymbol{E}|^2}{dx}\right)\right]}}{4\left[\overline{\mu}_{EK}\left(\frac{d\boldsymbol{E}_{max}}{dx}\right)+\overline{\mu}_{DEP}\left(\frac{d\nabla|\boldsymbol{E}|^2{}_{max}}{dx}\right)\right]\sqrt{D_T}}$

$$\Delta\mu_{EK,min}\boldsymbol{E}_{ave} + \Delta\mu_{DEP,min}\nabla|\boldsymbol{E}|^2{}_{ave} \geq \frac{6\left[\overline{\mu}_{EK}\left(\frac{d\boldsymbol{E}_{max}}{dx}\right)+\overline{\mu}_{DEP}\left(\frac{d\nabla|\boldsymbol{E}|^2{}_{max}}{dx}\right)\right]\sqrt{D_T}}{\sqrt{-\left[\overline{\mu}_{EK}\left(\frac{d\boldsymbol{E}}{dx}\right)+\overline{\mu}_{DEP}\left(\frac{d\nabla|\boldsymbol{E}|^2}{dx}\right)\right]}} \tag{19}$$

Assume there is no change in DEP forces to calculate minimum resolvable differences in electrokinetic effects:

$$\Delta\mu_{EK,min} \geq \frac{6\left[\overline{\mu}_{EK}\left(\frac{d\boldsymbol{E}_{max}}{dx}\right)+\overline{\mu}_{DEP}\left(\frac{d\nabla|\boldsymbol{E}|^2{}_{max}}{dx}\right)\right]\sqrt{D_T}}{\boldsymbol{E}_{ave}\sqrt{-\left[\overline{\mu}_{EK}\left(\frac{d\boldsymbol{E}}{dx}\right)+\overline{\mu}_{DEP}\left(\frac{d\nabla|\boldsymbol{E}|^2}{dx}\right)\right]}} \tag{20}$$

Similarly, setting the EK forces to a constant value allows the minimum resolvable differences in dielectrophoretic effects:

$$\Delta\mu_{DEP,min} \geq \frac{6\left[\overline{\mu}_{EK}\left(\frac{d\boldsymbol{E}_{max}}{dx}\right)+\overline{\mu}_{DEP}\left(\frac{d\nabla|\boldsymbol{E}|^2{}_{max}}{dx}\right)\right]\sqrt{D_T}}{\nabla|\boldsymbol{E}|^2{}_{ave}\sqrt{-\left[\overline{\mu}_{EK}\left(\frac{d\boldsymbol{E}}{dx}\right)+\overline{\mu}_{DEP}\left(\frac{d\nabla|\boldsymbol{E}|^2}{dx}\right)\right]}} \tag{21}$$

By assigning any changes in dielectrophoretic mobility to altered radius, a minimum value of resolvable particle diameter can be calculated according to:

$$\Delta r_{min} = \left[\frac{3\eta}{\varepsilon_f f_{CM}}\left[\left(\mu_{DEP}+\frac{1}{2}\mu_{DEP,min}\right)-\left(\mu_{DEP}-\frac{1}{2}\mu_{DEP,min}\right)\right]\right]^{1/2} \quad (22)$$

A similar approach allows solving equation 21 for minimum resolvable differences in f_{CM}:

$$\Delta f_{CM,min} = \frac{3\eta}{\varepsilon_f r^2}\left[\left(\mu_{DEP}+\frac{1}{2}\mu_{DEP,min}\right)-\left(\mu_{DEP}-\frac{1}{2}\mu_{DEP,min}\right)\right] \quad (23)$$

5.3 Results

In the following section, two scenarios will be addressed. In the first, the relationships described above are explored using typical field and gradient values achieved in published works. In the second scenario, resolution capabilities will be explored at the extent of highest reasonably achievable values (these values are limited by complicating factors such as heating or material breakdown). The values used for these two categories are listed in Table 5.1. They reflect numbers reported from experiments as well as those calculated via multi-physics modeling software (COMSOL) for existing g-iDEP designs. Note that most of the common values are within two orders of magnitude of the maximum values and extremely high-resolution separations have already been accomplished with this strategy.

5.3.1 Calculated values under common and best case conditions for radius

Equation 22 can be used to estimate the smallest resolvable difference in radius for a given nominal radius (Fig. 5.4A). This calculation includes an estimate of the diffusion coefficient (D_{diff}) as a function of radius, according to the Einstein equation ($D_{diff} = RT/6\pi\eta r$). The results indicate that the smallest resolvable difference at any

Common input values:

E_{ave}	$\nabla\|E\|^2_{ave}$	dE/dx_{ave}	$d\nabla\|E\|^2/dx_{ave}$	$\Delta E_{max}/dx$	$\Delta(\nabla\|E\|^2_{max}/dx)$
V/m	V^2/m^3	V/m^2	V^2/m^4	V/m^2	V^2/m^4
1.4E+05	9.0E+14	3.5E+09	3.1E+19	1.3E+07	2.5E+17

Highest Experimentally accessible values:

E_{ave}	$\nabla\|E\|^2_{ave}$	dE/dx_{ave}	$d\nabla\|E\|^2/dx_{ave}$	$\Delta E_{max}/dx$	$\Delta(\nabla\|E\|^2_{max}/dx)$
V/m	V^2/m^3	V/m^2	V^2/m^4	V/m^2	V^2/m^4
5.0E+06	1.0E+18	3.5E+11	3.1E+20	1.6E+08	1.1E+17

Table 5.1. Common and maximum experimental values. A typical particle diameter is one micrometer for many dielectrophoretic experiments. Geometric factors (insulator-based dielectrophoresis) include gate-widths between 100 nm and 30 mm, global applied fields of 10^4 V/m. These two factors and ranges therein allow for all calculated values.

radius is about 15 nm, and may be achieved when the nominal particle radius is approximately 1 μm. By dividing the smallest differentiable radius by the nominal radius, the relative resolving power can be estimated across a range of particle sizes. The result is approximately one part in 100. This proportionality is fairly consistent across particles ranging from one to ten micrometers in diameter. For a one-micrometer particle, the expected radius-based resolution should reach to ±10 nanometers.

Using the above equations with higher field strengths or a redesigned microchannel would result in improved resolution. This would yield smaller minimum differentiable variations in analytes. The increased electric field values considered here were the highest noted occurrences in our models as well as in the literature (Table 5.1). These values are currently limited by experimental considerations such as solution or materials breakdown. Improved power supplies or other trivial strategies cannot functionally improve values beyond what is considered here. At these higher field and gradient values, the smallest resolvable change in radius is reduced to approximately 500 pm for nearly all particles in the range investigated (Fig. 5.4B).

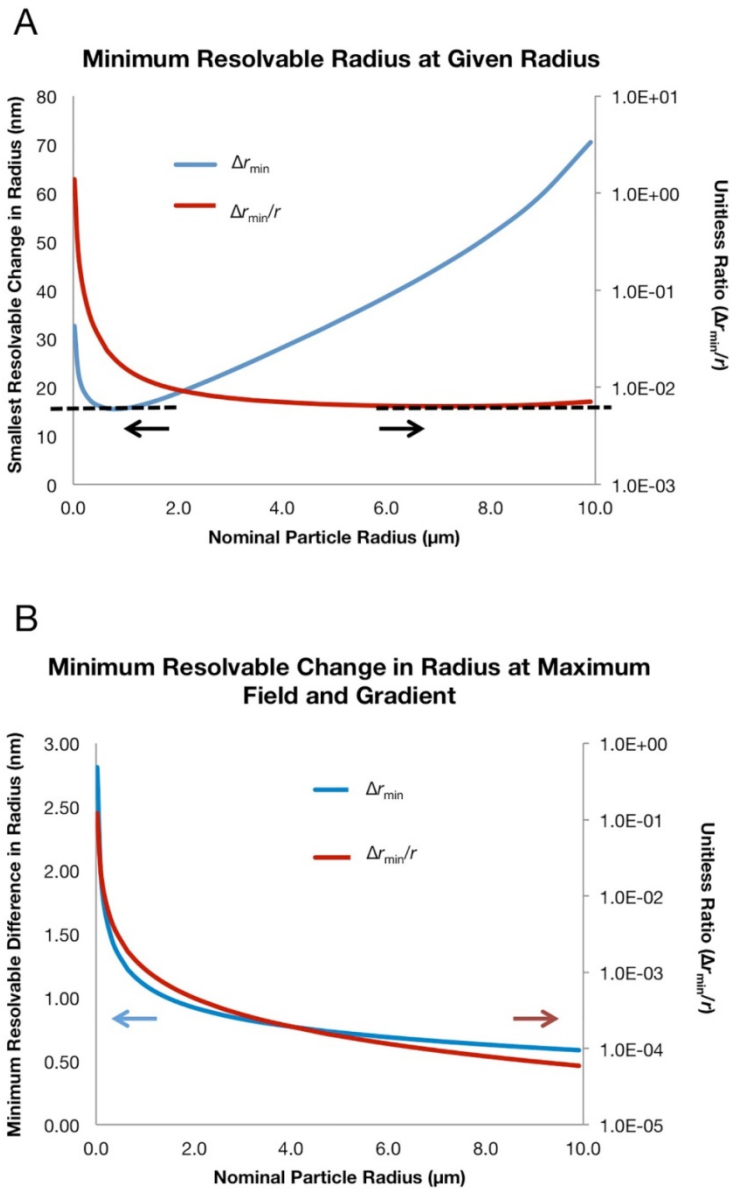

Figure 5.4. Minimum resolvable change in radius. A) Plot showing the smallest change in radius (blue line) that can be resolved as a function of the nominal radius of a particle using experimentally common field and gradient values (see Table 5.1). Also plotted is the normalized ratio of smallest resolvable difference divided by the nominal radius (red line). Arrows emphasize axis associated with each plot line. Note smallest value is ~15 nm at ~1 μm diameter and about $1{:}10^2$ can be separated. B) Plot showing the smallest change in radius (blue line) that can be resolved as a function of the nominal radius of a particle using maximum experimentally accessible field and gradient values (Table 5.1). Also plotted is the normalized ratio of smallest resolvable difference divided by the nominal radius (red line). Arrows emphasize axis associated with each plot line. Note smallest value is ~500 pm at ~1 μm diameter and about $1{:}10^4$ can be separated.

5.3.2 Calculated values under common and best case conditions for mobilities

Considering a particle with a diameter slightly less than one micrometer, for typical absolute magnitudes of operating fields and gradients, the minimum resolvable difference in dielectrophoretic mobility from equation 21 is about 10^{-23} m^4/V^2s for a particle with a nominal mobility of 10^{-19} m^4/V^2s ($\mu_{DEP} = \varepsilon_f r^2 f_{CM}/3\eta$, $\varepsilon_f = 10^{-9}$ F/m, $r = 10^{-6}$ m, $f_{CM} = -0.3$, $\eta = 10^{-3}$ Ns/m^2, Fig. 5.5A). This relationship also displays a fairly constant relative resolving power at around $1{:}10^4$ or 0.01% of the dielectrophoretic mobility. The minimum resolvable change in dielectrophoretic mobility is reduced to 10^{-26} m^4/V^2s with a relative resolution of about $1{:}10^8$, for maximized field and gradient strengths—some four orders of magnitude higher than the common experimental values (Fig. 5.5B).

Two factors that chiefly influence the profile of these relationships are the diffusion coefficient and the dielectrophoretic mobility (Fig. 5.5C). 1) The diffusion coefficient becomes large and an important factor at small radii. It effectively increases dispersion at small radii, increasing the variance (σ^2) and broadening the collected concentration profile. 2) The dielectrophoretic mobility ranges over several orders of magnitude, from 10^{-23} to 10^{-17} m^4/V^2s over the 20-nm to 10-μm range of this study. For larger DEP mobilities, the magnitude of the minimum resolvable value increases. However, comparing minimum to nominal values acts as a normalizing factor leaving the relative resolving power approximately constant across the range.

5.3.3 Calculated values under common and best case conditions for f_{CM}

Similar calculations were performed to determine the minimum resolvable difference in Clausius-Mossotti factor. The result is approximately one part in 10^5 (Fig.

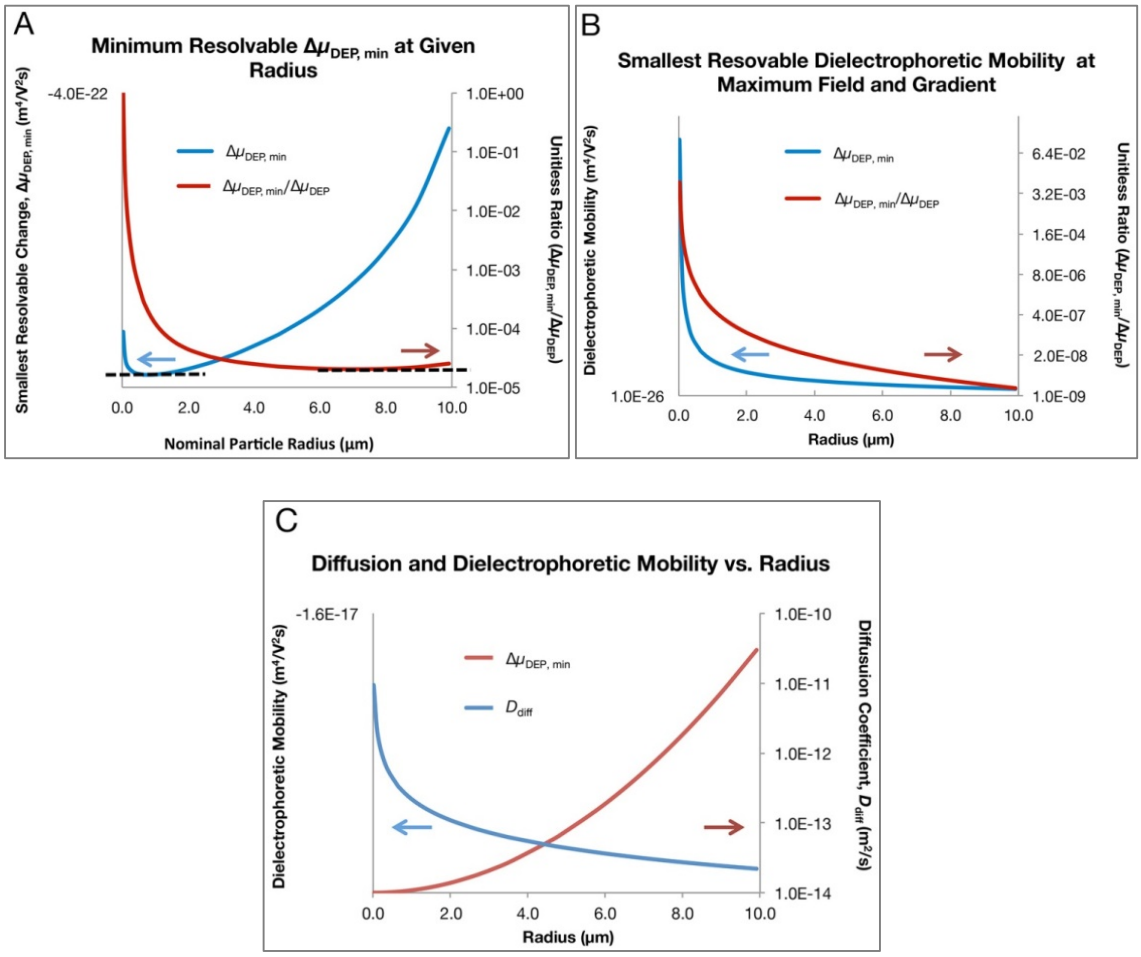

Figure 5.5. Minimum resolvable change in mobilities. A) Examination of smallest difference in dielectrophoretic mobility ($\Delta\mu_{DEP.min}$) that is calculated to be resolvable using experimentally common values of electric field strength and gradient. Absolute values (blue line, left axis) and the ratio of the minimum resolvable value divided by the nominal dielectrophoretic mobility (red line, right axis) are shown. Arrows emphasize axis associated with each plot line. Note the smallest absolute value is about 10^{-23} m^4/V^2s and relative values of about $1{:}10^4$ can be separated. B) Examination of smallest difference in dielectrophoretic mobility ($\Delta\mu_{DEP.min}$) that is calculated to be resolvable using maximum experimentally accessible values of electric field strength and gradient. Absolute values (blue line, left axis) and the ratio of the minimum resolvable value divided by the nominal dielectrophoretic mobility (red line, right axis—note: logarithmic) are shown. Arrows emphasize the axis associated with each plot line. Note the smallest absolute value is about 10^{-26} m^4/V^2s and about $1{:}10^7$ can be separated. C) Plots of two of the most influential factors defining the minimum resolvable physical properties of particles via g-iDEP: average dielectrophoretic mobility ($\mu_{DEP,ave}$) and diffusion coefficient (D_{diff}). Arrows emphasize the axis associated with each plot line. Note the diffusion coefficient becomes quite large at small particle diameters and the dielectrophoretic mobility becomes larger with increasing diameter.

5.6, red line) under standard conditions. The assessment of the Clausius-Mossotti factor under optimal or maximum conditions results in a similar plot (Fig. 5.6, blue line), but with the resolving power increasing to $1{:}10^8$.

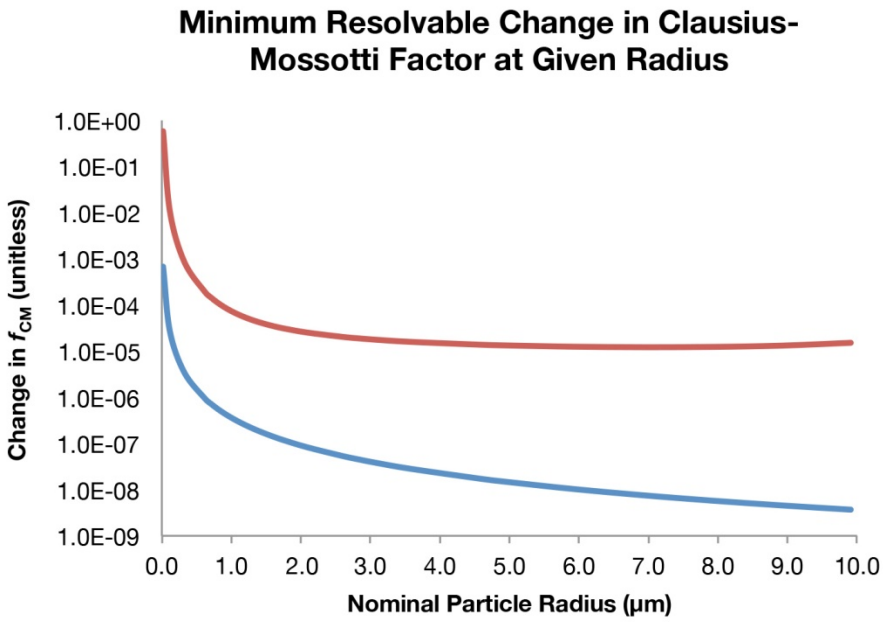

Figure 5.6. Minimum resolvable change in f_{CM}. Red line: Plot of smallest change in Clausius-Mossotti factor (f_{CM}) that can be separated versus particle diameter. Note that f_{CM} is unitless and that this plots suggests that relative values of approximately $1{:}10^5$ can be resolved under experimentally common values of electric field strength and gradient. Blue line: Plot of smallest change in f_{CM} (unitless) that can be separated versus particle diameter, for maximum experimentally accessible values of electric field strength and gradient. This suggests that differences as small as approximately $1{:}10^8$ can be resolved.

5.4 Discussion

The equations developed above suggest that a limited number of factors affect the resolution of a g-iDEP separation, including field strength ($\boldsymbol{E}_{ave}$ and indirectly $\nabla|\boldsymbol{E}|^2{}_{ave}$), the local slope of the electric field at each gate ($d\boldsymbol{E}/dx$ and $d(\nabla|\boldsymbol{E}|^2)/dx$), dispersive effects ($D_T$, including diffusion D_{diff}), and the gate-to-gate step-wise increase in ($d\boldsymbol{E}_{max}/dx$

and $d(\nabla|\boldsymbol{E}|^2{}_{\max})/dx$). Each of these factors can be manipulated by adjusting channel geometry and applied potential. In general, increasing local field gradients ($d\boldsymbol{E}/dx$ and $d(\nabla|\boldsymbol{E}|^2)/dx$), and decreasing gate-to-gate variation ($d\boldsymbol{E}_{\max}/dx$ and $d(\nabla|\boldsymbol{E}|^2{}_{\max})/dx$) will improve resolution (Table 5.2). We note the maximum experimental values demonstrated in condensed phase aqueous solution are about 10^6 V/m for $\boldsymbol{E}_{\text{ave}}$ and 10^{18} V^2/m^3 for $\nabla|\boldsymbol{E}|^2{}_{\text{ave}}$ [20].We also note that other related forces can be harnessed to create a local trap, including electrothermal effects, while understanding that this effect may also add to dispersion.

Minimize	Maximize	Minimal, arbitrary, or not adjustable
$d\boldsymbol{E}_{\max}/dx$	$\boldsymbol{E}_{\text{ave}}$	$\Delta\mu_{\text{EK, min}}$
$d(\nabla\|\boldsymbol{E}\|^2{}_{\max})/dx$	$\nabla\|\boldsymbol{E}\|^2{}_{\text{ave}}$	μ_{EK}
	$d\boldsymbol{E}/dx$	$\Delta\mu_{\text{DEP, min}}$
	$d(\nabla\|\boldsymbol{E}\|^2)/dx$	μ_{DEP}
		D_{T}

Table 5.2. Maximizing resolution. Since diffusion (D_{diff}) and average dielectrophoretic mobility ($\bar{\mu}_{\text{DEP}}$) are a function of radius and influence resolution, these variables interact to give a minimum in $\Delta r_{\min}$.

There are some subtle issues, which must be addressed when executing these calculations. For any given specific gate, and true for all of these calculations, the forces (velocities) must balance ($\mu_{\text{EK}} * \boldsymbol{E}_{\text{ave}} + \mu_{\text{DEP}} * \nabla|\boldsymbol{E}|^2{}_{\text{ave}} = 0$). Generally, electrokinetic mobility was used as an adjustable parameter, keeping well within ranges of known values from a very rich data set, captured over decades via capillary electrophoresis, as reflected in the literature. In some cases, the electric field ($\boldsymbol{E}_{\text{ave}}$) was adjusted. The dielectrophoretic mobility was not adjusted, since it was calculated from fundamental

factors (radius, permittivity, etc.). In general, these values corresponded reasonably with real-world expectations. For instance, for a balanced target $\boldsymbol{E}_{\text{ave}} = -\frac{\mu_{\text{DEP}}}{\mu_{\text{EK}}}\boldsymbol{\nabla}|\boldsymbol{E}|^2{}_{\text{ave}}$. Real values of μ_{DEP} can differ significantly from the simple Clausius-Mossotti factor-based calculations, but this is relatively unimportant to the development of this theory [17, 21]. The actual values are bracketed in practice and these remain within reasonable values of the juxtaposing $\mu_{\text{EK}} * \boldsymbol{E}_{\text{ave}}$ product. Using modeled values and multiplying the ratio of $\frac{\mu_{\text{DEP}}}{\mu_{\text{EK}}}$ by $\boldsymbol{\nabla}|\boldsymbol{E}|^2{}_{\text{ave}}$ yields 10^6 V/m. An $\boldsymbol{E}_{\text{ave}}$ maximum value is approximately 10^6 V/m before materials begin to break down.

The Clausius-Mossotti factor (f_{CM}) was set at -0.3, which is a reasonable value and results in a negative dielectrophoretic force. Mathematically and theoretically this factor only accounts for the polarizability of the particle, but in practice this factor turns into the catchall for differences in behaviors of otherwise-identical particle populations. The real physical origins of the forces on the particles arise from a diverse range of features, including size, shape, roughness, heterogeneity, internal structures, internal charge distribution, fluidity of internal structures, deformability, charge mobility, and interactions with local environment, all of which may or may not directly influence polarizability. Any difference in any of these features may result in a separation, although none of them are analytically accounted for in the theory underlying f_{CM}.

Noting that $\frac{\boldsymbol{E}_{\text{ave}}}{\boldsymbol{\nabla}|\boldsymbol{E}|^2{}_{\text{ave}}} = -\frac{\mu_{\text{DEP}}}{\mu_{\text{EK}}}$ for a given capture or balance point, the focusing can be maintained while minimizing $\boldsymbol{E}_{\text{ave}}$. This suggests that dynamic range can be extended with lower applied voltage for capture, avoiding limitations in power supplies

or physical breakdown of materials. However, this extension is juxtaposed by a decrease in resolution with lower $\boldsymbol{E}_{\text{ave}}$.

The derivation presented herein ties the change in maximum local gradient between gates ($d\boldsymbol{E}_{\text{max}}/dx$ and $d(\boldsymbol{\nabla}|\boldsymbol{E}|^2{}_{\text{max}})/dx$) to the specific gate position along the channel (x). Conceptually, as the gate-to-gate separation approaches zero, the capture regions become arbitrarily close to each other and thus the continuous analysis is valid [10, 22]. One way our approach may be considered is to examine continuous functions which are sampled in either time or space and then analyzed and processed in sampled-data systems. Subsequently, the processed samples are used to reconstruct a continuous waveform [23]. Sampled data methods are not explored here, but serve to illustrate that such treatment is not unprecedented. Treating these values as continuous variables of x simplifies the derivation, but brings up a noteworthy caveat. In actuality, the local maxima which comprise $d\boldsymbol{E}_{\text{max}}/dx$ and $d(\boldsymbol{\nabla}|\boldsymbol{E}|^2{}_{\text{max}})/dx$ must occur at successive gates with a finite, non-zero x-axis separation. Physical implementation of arbitrarily-close gates is not realizable. As the distance between gates becomes very small, the necessary local field maxima, $\boldsymbol{E}_{\text{max}}$ and $\boldsymbol{\nabla}|\boldsymbol{E}|^2{}_{max}$, decrease and eventually collapse into a smooth global gradient. Since each gate creates a local disruption/maximum in the field, sufficient space is required for the field to return to its relaxed or average value before a new disruption/maximum can be created with an even higher value of $\boldsymbol{\nabla}|\boldsymbol{E}|^2$. Furthermore, gates must be separated by a distance greater than the characteristic variance of a captured analyte. This distance may be estimated from the predicted peak width of a target population. As long as the physical separation between gates is several times the width of collected targets, the system is reasonable.

This system can be operated with gates in parallel as well as in series with the same or similar results, and the derivation could be reconstructed to reflect such a design. A similar construct has been used to examine electrophoretic exclusion [24]. Relevant field maxima at each parallel gate element would need to be designed with sufficiently different values to capture non-mixed analyte populations. The work by Kenyon et al., utilized alongside the approach developed here would elucidate these values.

A practical and important metric of resolution is $\Delta\mu_{EK,min}$ and $\Delta\mu_{DEP,min}$. These two values allow direct comparison with other electrokinetic and dielectrophoretic techniques. In general, two scenarios are considered when assessing the theoretical resolution. Under common experimental values, $\Delta\mu_{EK,min} = 2 \times 10^{-12}$ m^2/Vs (equation 20) and $\Delta\mu_{DEP,min} = 10^{-23}$ m^4/V^2s (see Fig. 5.5A). Current and past literature contains many examples of minimum resolvable electrokinetic values; this number is demonstrably better than any reported [24]. Such values are rarely reported for DC dielectrophoresis and thus cases for comparison are limited. For the 'best case' scenario, limited by breakdown voltages for materials and maximal gradients, these become $\Delta\mu_{EK,min} = 2 \times 10^{-14}$ m^2/Vs and $\Delta\mu_{DEP,min} = 10^{-26}$ m^4/V^2s. One limitation for the high-resolution capabilities of electrokinetic effects is that the targets need appreciable dielectrophoretic force and therefore traditional targets smaller than 20 nm in diameter are not accessible.

No quantitative studies have been published examining the peak width and resolution of g-iDEP, or any iDEP device for that matter. One major limitation is the lack of accepted standard materials of known dielectrophoretic properties. However, there are many clues suggesting the calculated bandwidths are reasonable and that the technique offers high-resolution separations. In the work of Staton et al. [12], 200 nm particles were

focused into a band approximately three micrometers wide (Fig. 2 in reference). Under the conditions of the experiment, the calculated bandwidth using the derivation here is one micrometer. This result is reasonable since there may be many sources of dispersion not explicitly included in this model for this study. Other experiments using iDEP show bandwidths for targets ranging from large molecules to 5-μm diameter particles in the range of 1-10 μm [25, 26]. The simple reason for these narrow peaks is that the focusing slopes for this strategy are very large compared to other techniques. The '*a*' factor (slope of restoring force) for focusing can reach 10^3 s^{-1} whereas traditional techniques (IEF, gradient field systems) range from 10^{-4} to 10 s^{-1}. Since our model does not yet include the dispersive effects of particle-particle interactions and lateral heterogeneity of the gate gradient, these results again suggest that the theory presented is reasonable.

5.5 Conclusions

The derivation presented here suggests that extremely high-resolution separations are possible for particles from 20 nm to 10 μm in diameter. These separations may reflect very subtle differences in the target particles. In fact, specific strains of bacteria have already shown significant differentiation using these forces [15, 27]. Used as ultimate benchmarks, the best case suggests that one part in 10^3 differences in diameter (1 nm for a 1-μm particle) can be isolated, one part in approximately 10^8 can be separated as measured by Δf_{CM} or $\Delta \mu_{DEP,min}$. Compared with competing separations or analysis techniques, these offer orders of magnitude improvements.

5.6 References

[1] Giddings, J. C., Eyring, H., *Journal of Physical Chemistry* 1955, *59*, 416-421.

[2] Jorgenson, J. W., Lukacs, K. D., *Anal. Chem.* 1981, *53*, 1298-1302.

[3] Kolin, A., *Journal of Chemical Physics* 1954, *22*, 1628-1629.

[4] Brakke, M. K., *Journal Of The American Chemical Society* 1951, *73*, 1847-1848.

[5] Koegler, W. S., Ivory, C. F., *Journal of Chromatography A* 1996, *726*, 229-236.

[6] Keller, R. A., Giddings, J. C., *Journal of Chromatography* 1960, *3*, 205-220.

[7] Giddings, J. C., *Analytical Chemistry* 1963, *35*, 1999-2002.

[8] Foret, F., Fanali, S., Ossicini, L., Bocek, P., *J. Chromatogr.* 1989, *470*, 299-308.

[9] Giddings, J. C., Dahlgren, K., *Separation Science* 1971, *6*, 345-356.

[10] Kelly, R. T., Woolley, A. T., *Journal of Separation Science* 2005, *28*, 1985-1993.

[11] Pysher, M. D., Hayes, M. A., *Analytical Chemistry* 2007, *79*, 4552-4557.

[12] Staton, S. J. R., Chen, K. P., Taylor, T. J., Pacheco, J. R., Hayes, M. A., *Electrophoresis* 2010, *31*, 3634-3641.

[13] Jones, P. V., Staton, S. J. R., Hayes, M. A., *Analytical and Bioanalytical Chemistry* 2011, *401*, 2103-2111.

[14] Staton, S. J. R., Jones, P. V., Ku, G., Gilman, S. D., Kheterpal, I., Hayes, M. A., *Analyst* 2012, *137*, 3227-3229.

[15] Jones, P. V., DeMichele, A. F., Kemp, L., Hayes, M. A., *Analytical and Bioanalytical Chemistry* 2014, *406*, 183-192.

[16] Jones, T. B., *Electromechanics of Particles*, Cambridge University Press 2005.

[17] Weiss, N. G., Jones, P. V., Mahanti, P., Chen, K. P., Taylor, T. J., Hayes, M. A., *Electrophoresis* 2011, *32*, 2292-2297.

[18] Giddings, J. C., *Unified Separation Science*, John Wiley and Sons, New York 1991.

[19] Giddings, J. C., *Dynamics of Chromatography*, M. Dekker, New York 1965.

[20] Jacobson, S. C., Culbertson, C. T., Daler, J. E., Ramsey, J. M., *Anal. Chem.* 1998, *70*, 3476-3480.

[21] Kang, K. H., Xuan, X. C., Kang, Y. J., Li, D. Q., *Journal Of Applied Physics* 2006, *99*, art. numb. 064702.

[22] Tolley, H. D., Wang, Q. G., LeFebre, D. A., Lee, M. L., *Analytical Chemistry* 2002, *74*, 4456-4463.

[23] Shannon, C. E., *Proceedings of the Institute of Radio Engineers* 1949, *37*, 10-21.

[24] Kenyon, S. M., Keebaugh, M. W., Hayes, M. A., *Electrophoresis* 2014, *35*, 2551-2559.

[25] LaLonde, A., Gencoglu, A., Romero-Creel, M. F., Koppula, K. S., Lapizco-Encinas, B. H., *Journal Of Chromatography A* 2014, *1344*, 99-108.

[26] Liao, K. T., Tsegaye, M., Chaurey, V., Chou, C. F., Swami, N. S., *Electrophoresis* 2012, *33*, 1958-1966.

[27] Braff, W. A., Willner, D., Hugenholtz, P., Rabaey, K., Buie, C. R., *Plos One* 2013, *8*, art. numb. e76751.

CHAPTER 6

IMPROVING THE DESIGN OF G-iDEP MICROCHANNELS

6.1 Theoretical approach

Insulator geometry has significant effects upon the resolution and capabilities of a g-iDEP microchannel. As discussed in Chapter 2, the voltage drop across any material is proportional to its resistance. Because this drop is greater across materials or regions with a higher resistance, a stronger electric field is produced. Resistance is inversely proportional to the cross-sectional area of the medium, thus a cross-section results in higher resistance, greater voltage drop, and thus higher field strength. These relationships describe the general characteristics of electric field properties within a g-iDEP microchannel, which in turn determine its separatory capabilities and resolution.

The goals and benefits of increased resolution in a g-iDEP system are analogous to those for all separation science, including examples like chromatography, mass-spectrometry, and gel or capillary electrophoresis [1]. For any analytical technique, the utility and significance of the approach is defined by the amount of meaningful diagnostic information that can be garnered with a given amount of time, space, or effort [2]. Improving metrics such as resolution, dynamic range, or overall peak capacity for a particular technique increase the amount of useful information that can be obtained from samples.

Resolution can be described as spatial or temporal isolation of multiple analytes. Increasing resolution offers the potential for more finely-tuned discrimination of similar analytes. It can also enable simultaneous separation of a larger number of analytes. Conversely, poor or decreased resolution can result in overlapping peaks and low peak

capacity. This limits both the ability to differentiate similar analytes and analytical throughput. For g-iDEP separations, discrete capture zones comprise a discontinuous series, rather than a single separatory continuum. As a result, poor resolution is not adequately explicated by traditional descriptors such as "broad peaks." Instead, analyte may co-capture across multiple capture zones at adjacent gates (Fig 6.1). Therefore, improved resolution will increase the capability of g-iDEP systems to differentiate similar analytes by limiting the co-capture across gates and by being able to separate a larger number of species in a single analysis (Fig. 6.2).

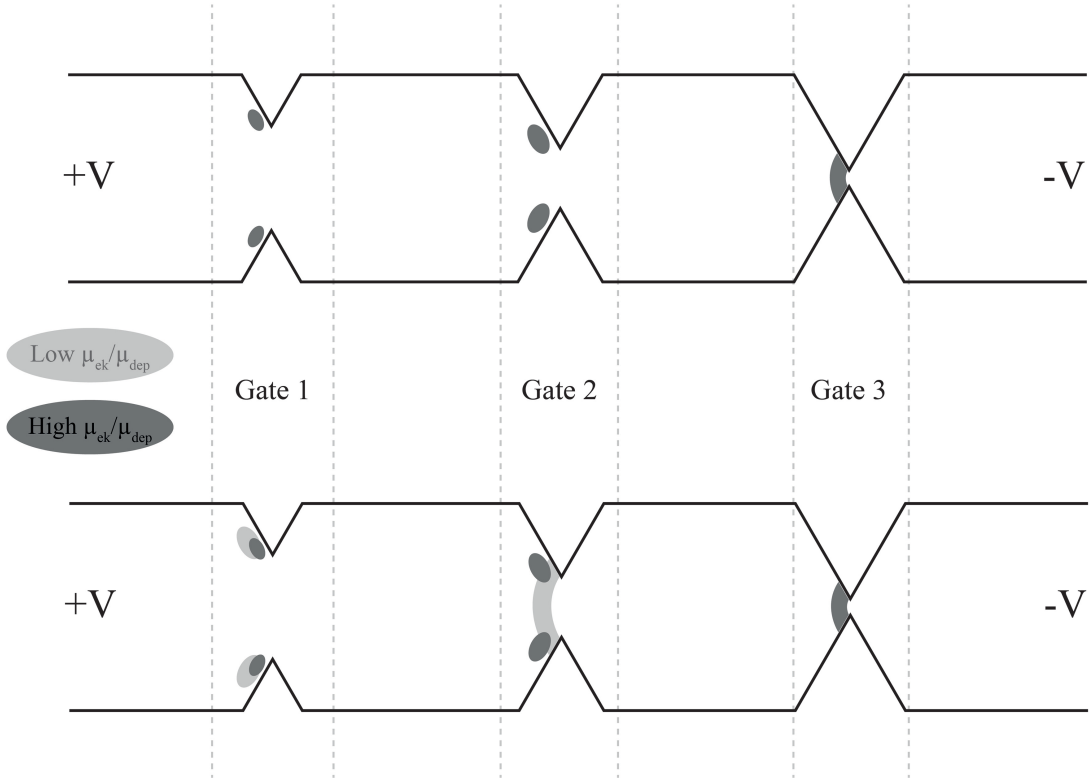

Figure 6.1. Illustration showing unresolved capture in a g-iDEP microchannel. (Top) Fractions of a single analyte population are captured at multiple adjacent gates. Ideally, an analyte would instead be confined to capture at a single gate (or as few gates as possible). (Bottom) Fractions of two analyte populations are captured at multiple adjacent gates with overlap.

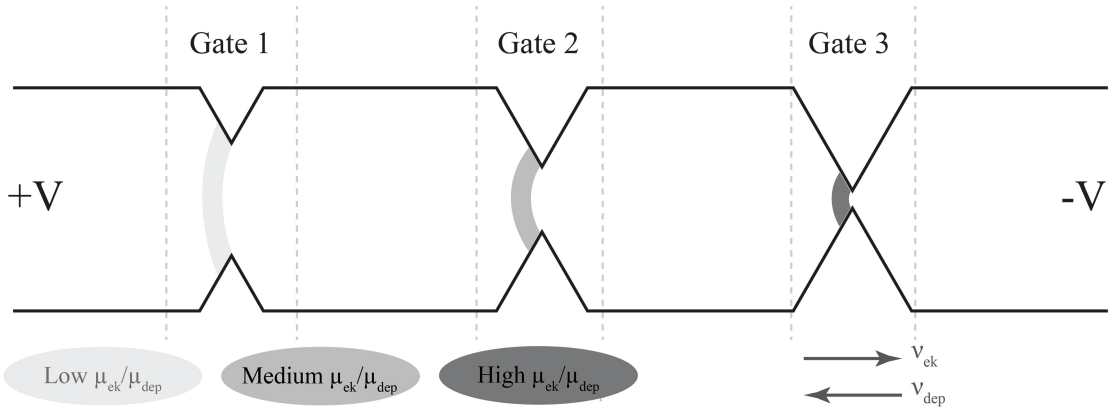

Figure 6.2. Illustration showing resolved capture in a g-iDEP microchannel. Increased resolution offers the potential of more finely-tuned discrimination of similar analytes. It could also enable simultaneous separation of a larger number of analytes.

Chapter 5 developed a theoretical framework for describing the resolving capabilities of a g-iDEP system [3]. The equations developed therein suggest that certain controllable parameters affect the resolution of a g-iDEP microchannel. These include field strength (specifically as represented by $\boldsymbol{E}_{\text{ave}}$ and $\boldsymbol{\nabla}|\boldsymbol{E}|^2{}_{\text{ave}}$), the local slope of the electric field at each gate ($d\boldsymbol{E}/dx$ and $d(\boldsymbol{\nabla}|\boldsymbol{E}|^2)/dx$), and the gate-to-gate step-wise increase in local field maxima (represented by $d\boldsymbol{E}_{\text{max}}/dx$ and $d(\boldsymbol{\nabla}|\boldsymbol{E}|^2{}_{\text{max}})/dx$). Also important to consider are the total dispersive effects throughout the channel (represented by D_{T}). Changing applied potential or the channel geometry can modify each of these parameters. The resolution of a g-iDEP microchannel can be improved by increasing local field gradients ($d\boldsymbol{E}/dx$ and $d(\boldsymbol{\nabla}|\boldsymbol{E}|^2)/dx$), decreasing gate-to-gate variation ($d\boldsymbol{E}_{\text{max}}/dx$ and $d(\boldsymbol{\nabla}|\boldsymbol{E}|^2{}_{\text{max}})/dx$), and reducing sources of dispersion. The latter two approaches to improving resolution are explored in greater detail in sections 6.2 and 6.3 below.

Based on the mathematical expressions for electrokinetic/dielectrophoretic capture included in Chapter 2 of this dissertation, the following expression can be used to represent conditions for particle trapping at a gate:

$$\frac{\nabla|\boldsymbol{E}|^2 \cdot \boldsymbol{E}}{E^2} = e_{\mathrm{c}} \geq \frac{\mu_{\mathrm{EK}}}{\mu_{\mathrm{DEP}}} \quad (1)$$

Importantly, this expression relates electric field parameters within the channel directly to the characterizable and intrinsic properties of analyte(s) that are to be differentiated. To simplify the present discussion, this field-related term will be expressed as e_{c}. This value (and the concomitant electromotive force experienced by a particle) reaches a local maximum near each gate. Given knowledge of the mobilities of the species to be analyzed, the required value of e_{c} can be determined. The design must, therefore, accommodate the achievement of this value. The gate-to-gate change in e_{c} maxima will directly affect gate-to-gate differentiation of particles. This latter concept can also be expressed as:

$$\Delta e_{\mathrm{c}} \propto \Delta\left[\frac{\mu_{\mathrm{EK}}}{\mu_{\mathrm{DEP}}}\right] \quad (2)$$

6.2 Designing a new series of sawtooth features

In order to examine and potentially refine the capabilities of sawtooth g-iDEP microchannel designs, the electric potential distribution within a channel was modeled. This was accomplished using finite-element multiphysics software (COMSOL, Inc.). In order to simplify the complexities inherent to 3D modeling and to focus on gate-to-gate variability, this study was limited to 2D geometry and considered the electric field along the channel centerline where dielectrophoretic and electrokinetic forces are collinear.

This centerline is parallel to the channel's long (separatory) axis and centered between the sawtooth vertices.

The first published g-iDEP microchannel (V1) consisted of successive sets of six identical gates, where the gate pitch (p) decreased after each set of gates (Δp). This created successively more constricted sets of gates moving from inlet to outlet. In the V1 microchannel, the absolute difference in p (measured in microns) between each set of gates increases exponentially along the channel towards the outlet. Thus, most of the channel consists of gate sets that can be described as possessing large values of p and small values of Δp. In contrast, the last three sets of gates are described by relatively small values of p and large values of Δp. Specifically, p values for the last three sets of gates in the V1 microchannel are 300 μm, 90 μm, and 27 μm. Throughout most of the channel this geometry yields small and minimally varying values of e_c that are insufficient to produce capture zones. Near the end of the channel, as e_c and the changes in e_c become larger, the trapping forces increase exponentially (Fig. 6.3). This geometry results in sub-optimal resolving capabilities for separations. An analyte is unlikely to capture along much of the channel due to large p and low e_c. At the last three sets of gates, where p and e_c are more conducive to the formation of capture zones, Δp is too large between gate sets to offer fine-tuned differentiation of analytes ($\Delta[\mu_{EK}/\mu_{DEP}]$). Experimental results with the V1 microchannel support this idea. With most experimentally-accessible values of applied potential, capture only occurs at the ultimate or penultimate sets of gates.

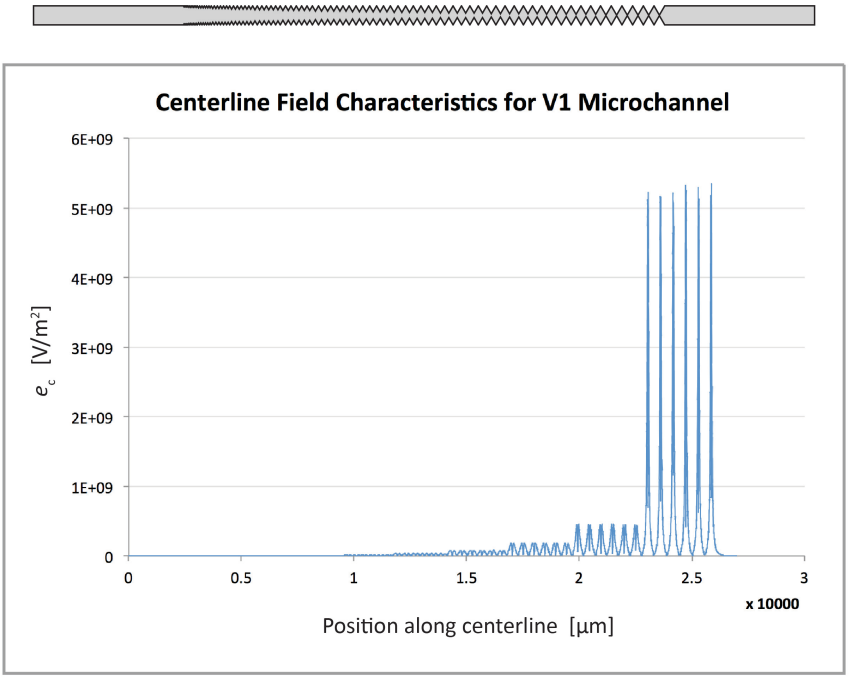

Figure 6.3. Centerline values of e_c modeled for the V1 microchannel. The channel inlet and large p values are oriented to the left, while the outlet and small p values are oriented to the right. Specific values for e_c depend upon channel geometry and the applied potential (500 V for this model). Each set of gates consists of 6 geometrically equivalent gates, all with equal p.

Resolution theory as applied to g-iDEP microchannels suggests a few possible approaches to improving the resolution of a microchannel. One such approach involves decreasing the gate-to-gate rate of change in local electric field maxima. Decreasing Δe_c in this manner consequently decreases the rate of change in local force maxima as well. This offers the potential to improve resolution of analytes by creating a series of more finely tuned and graduated dielectrophoretic traps. Each trap is then capable of distinguishing smaller gradations in particle characteristics ($\Delta[\mu_{EK}/\mu_{DEP}]$). This approach has the added advantage of yielding a greater separation (in terms of both physical distance and the number of intervening gates) between capture zones for two analytes.

In an effort to improve resolution and enable simultaneous separation of two similar analytes, two new microchannels (designated V2a and V2b) were designed based on these principles. The V2 microchannel designs feature more incremental stair-steps in pitch between sets of gates. Furthermore, the increase in e_c between gate-sets was linearized. In other words, Δe_c was kept approximately constant between each set of gates. Modeled values of e_c are related to gate pitch (p) by a power function (Fig. 6.4). The specific values of e_c are related to additional inputs, including the applied voltage and the specific channel geometry. Using this data, a progression of p values was

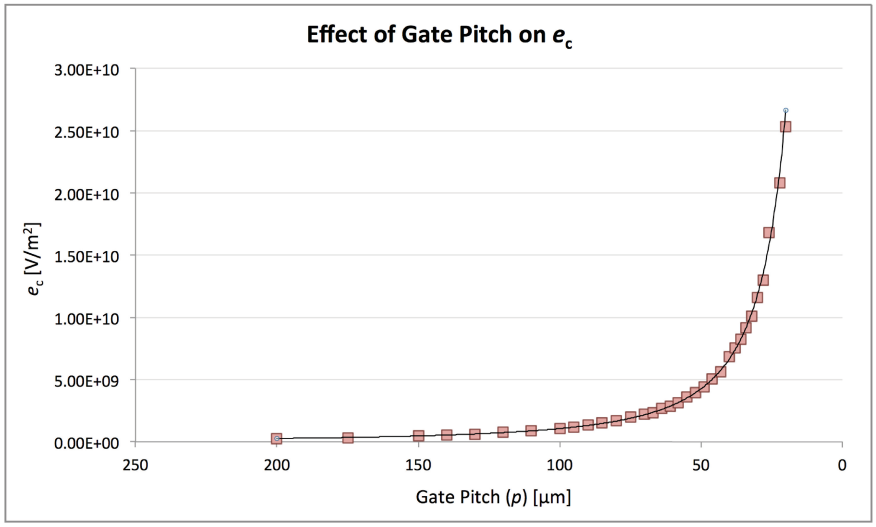

Figure 6.4. Centerline maxima in e_c for a hypothetical sawtooth microchannel. Values for e_c are represented as a function of p. The channel inlet and large p values are oriented to the left, while the outlet and small p values are oriented to the right. The increase in e_c with respect to p can be represented as a power function.

calculated that would yield a linear increase in e_c across a channel, ranging between a desired starting and ending value for p (Fig. 6.5).

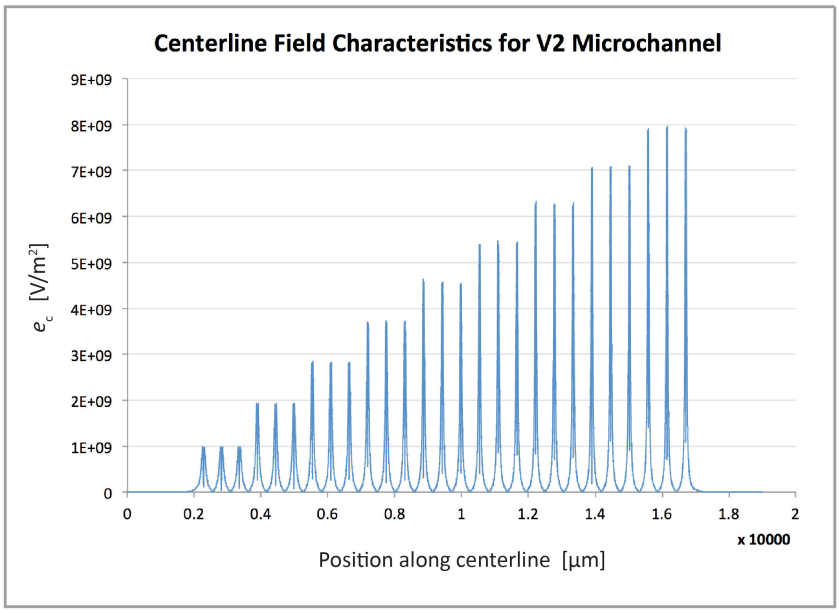

Figure 6.5. Centerline values of e_c modeled for a V2 microchannel. A progression of values for p was calculated to yield a linear step-wise increase in the local maxima of e_c between gate sets. Each set consists of three geometrically equivalent gates, all with equal p.

Each of the V2 microchannel designs was created for use with a particular range of bioparticle sizes. V2a was designed for use with cells and other large bioparticles. It featured initial and final gate pitches of 73 and 25 µm, respectively. V2b was designed for use with small bioparticles such as viruses and proteins. It featured initial and final gate pitches of 30 and 3 µm, respectively.

6.3 Exploratory investigation of gate design

Some of the earliest experiments performed with iDEP used angular posts such as diamonds or triangles to create electric field gradients [4, 5]. These shapes feature sharp corners, which yield strong gradients in the electric field. Sharp features thus offer the potential advantage of strong DEP force, which can contribute to particle trapping at a

gate, even for particles traveling on or near the channel centerline [6]. A potential disadvantage of these strong and highly-localized electric field gradients arises from the fact that particles traveling along different streamlines may encounter a significantly different dielectrophoretic force as they approach a gate (Fig. 6.6). To assess this effect in more detail, first consider a single gate within a sawtooth microchannel. If the field properties are examined along an axis orthogonal to the channel's longitudinal (separatory) axis, it becomes apparent that the value of e_c varies along this transverse axis especially in the immediate vicinity of a gate. Moving away from the axis midpoint toward an insulator vertex, e_c increases significantly. This condition can be referred to as transverse-axis field variability. As a result of this variability, particles traveling along streamlines near the channel periphery will encounter significantly higher values of e_c than those traveling along the channel centerline. These values may differ by an order of magnitude or more (Fig. 6.6, top image).

A large degree of transverse-axis field variability results in certain undesirable consequences for analyte resolution and separation. As described above, V2 channels were designed to decrease Δe_c and thus improve resolution. One of the drawbacks associated with small Δe_c is the potential for a greater degree of capture/zone spreading across adjacent gates. Therefore, for any analyte there is an optimal Δe_c, which is small enough to allow differentiated or unique capture at a gate, without being so small that capture is spread across adjacent gates (as modeled in Fig. 6.6, bottom image).

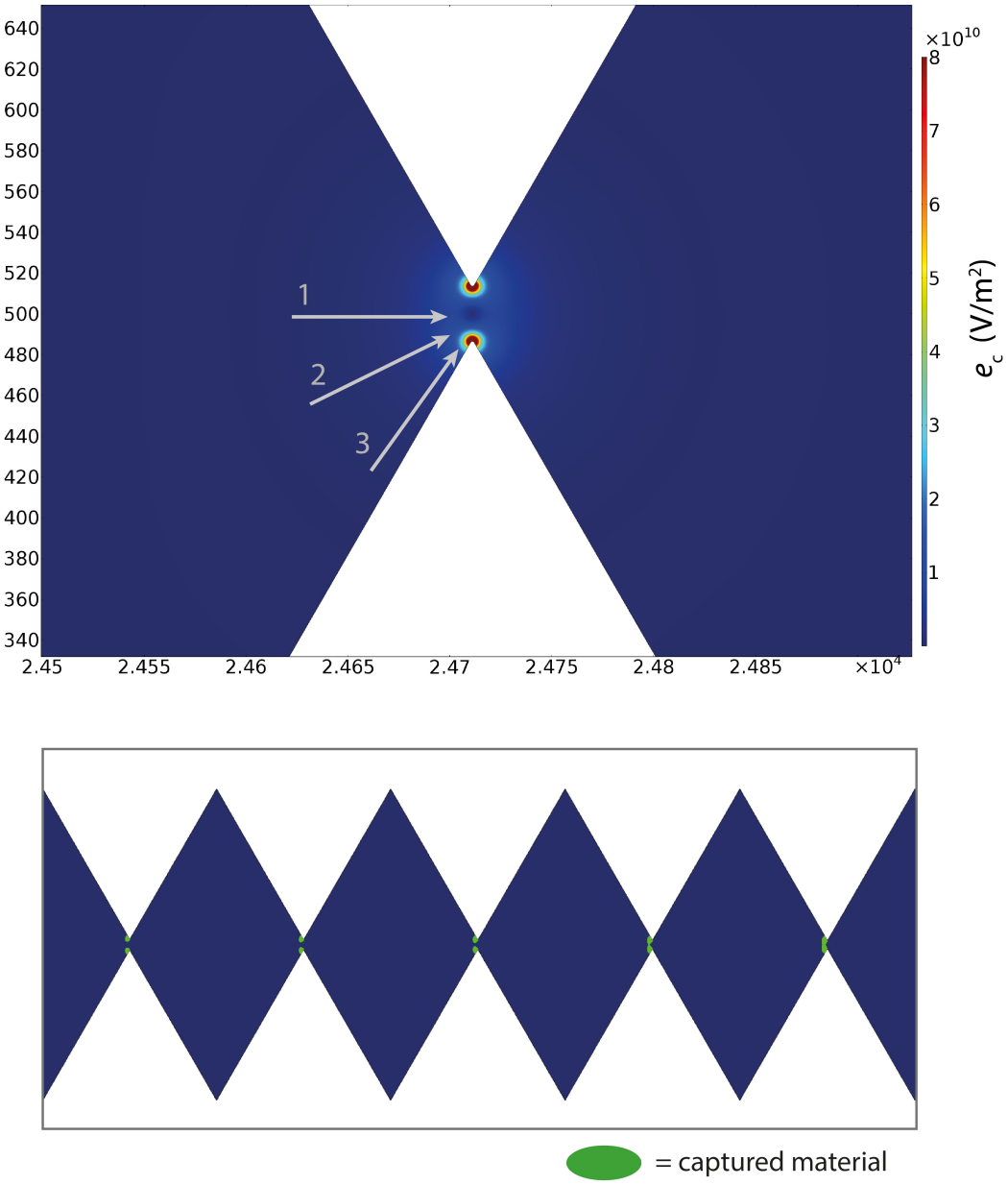

Figure 6.6. Modeled values of e_c for a gate in a sawtooth g-iDEP microchannel. Using COMSOL Multiphysics software, field properties were modeled within the V2a microchannel design, at an applied potential of 500 V. (Top) Sharp features create strong local gradients in the electric field. As a result, particles traveling along streamlines near the channel periphery (arrow 3) will encounter stronger DEP force and are thus more likely to be trapped than particles traveling on or near the channel centerline (arrows 1 and 2). (Bottom) Using COMSOL Multiphysics, and Equation 19 in Chapter 2, the conditions for capture of a hypothetical analyte were modeled. The inhomogeneity in e_c at the gate results in capture at multiple adjacent gates. In this image, the left- and right-most gates shown have pitches of ~ 35 and 30 µm, respectively.

Finding ways to decrease capture zone spreading between adjacent gates is analogous to decreasing total dispersion (D_T) within the channel, and will improve overall resolution. With existing sawtooth designs, a percentage of the total analyte population is captured at leading gates, before the analyte encounters a gate where complete trapping occurs. Decreasing transverse-axis field variability at each gate by producing uniform values of e_c from vertex to vertex would effectively increase the capture efficiency of each gate, and thus decrease gate-to-gate dispersion since particles in all streamlines would encounter the same value of e_c. Achieving constant e_c may not be possible, but approximating that condition would improve resolution.

Possible approaches to decreasing transverse-axis field variability could include rounding the sawtooth vertices or using smoothly contoured insulator geometry. Such features have been used in other implementations of iDEP, such as circular post-based designs. Other work by the author has explored the use of tapered constrictions that produce a linear increase in the electric field strength, and thus a constant gradient (represented by $\boldsymbol{\nabla}|\boldsymbol{E}|^2$) [7]. In this case, the cross-sectional area of the channel decreases as a function of $1/x$, where x is longitudinal distance along the channel. This approach is also similar to conductive polymer designs used for equilibrium gradient focusing [8].

In this vein, various gate designs were modeled using finite-element modeling. The results were qualitatively evaluated for their effect on local electric field properties. These gate designs included hurdles, rounded features, and various tapers (Fig. 6.7). Also investigated were the effects of asymmetric gate geometry with different leading and trailing features. Results confirmed that rounded features produced smaller variation in e_c across the transverse axis of gates. Gates tapered by factors of "$1/x$" yielded the least

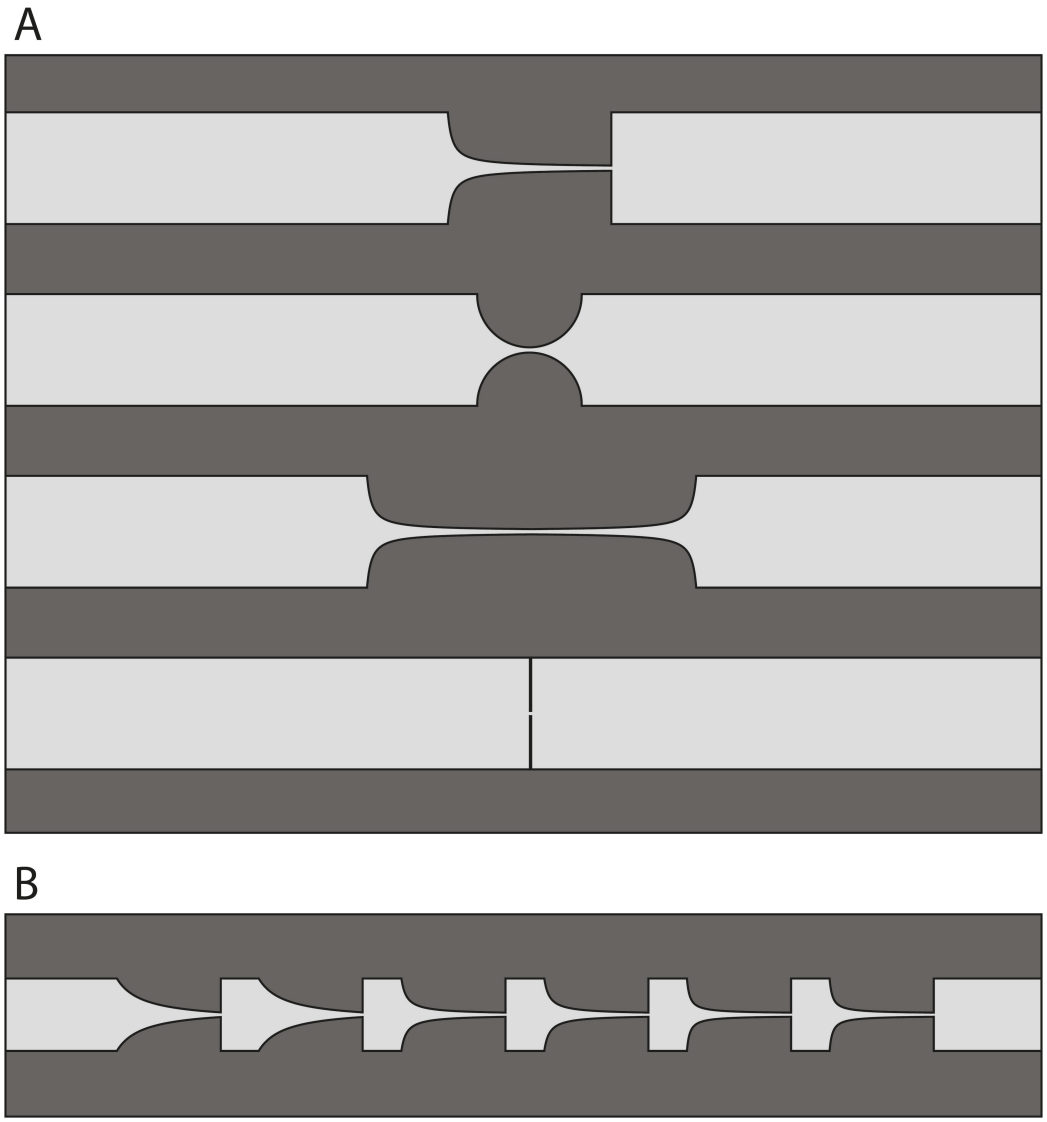

Figure 6.7. Illustration of various hypothetical gate designs. (A) This image depicts a set of gate designs that were subsequently modeled and examined for their effects on electric field values. Represented here from top to bottom are an asymmetric $1/x$ taper, semicircles, a symmetric $1/x$ taper, and hurdles. This list is representative of the designs examined, but not exhaustive. (B) Example showing how various tapers could be incorporated into a g-iDEP microchannel.

degree of transverse-axis field variability, achieving near-constant profiles of e_c.

However, as outlined above, all smooth-featured gates were limited in terms of the maximum value of e_c achieved. As developed in Chapter 5, resolution theory for g-iDEP

suggests that reduced values of e_c also reduce the overall resolution capabilities of a g-iDEP microchannel. This then suggests that the search for optimal resolution and peak capacity may require a compromise or balance between improving gate efficiency (served by the use of smooth features), and achieving maximal local values of e_c (served by sharp features and geometric discontinuities).

6.4 Integration with microfluidic systems

The future potential of g-iDEP as a tool for bioparticle analysis will likely be served by incorporating g-iDEP separatory channels into larger systems. With the ability to both isolate and concentrate analytes, g-iDEP channels may be uniquely well-suited for use in micro-total-analysis systems. Multiple g-iDEP channels could operate in parallel and in series to create systems with an extremely large dynamic range. These channels may also be multiplexed with other types of microfluidic analysis. These could feasibly include other types of separations-based analysis, spectroscopy, or amplification.

To this end, preliminary investigations explored g-iDEP channels with multiple outlets/inlets. Models of both sawtooth and tapered g-iDEP channels were created with periodic and symmetric side-channels. Examples are shown in Fig. 6.8. The aim of these designs was to facilitate the selective removal of captured material by applying addressable electric-field-driven flow or even incorporating pressure-driven flow. Theoretically, side-channels could be implemented at or near every gate (Fig 6.8, A). For simplified fabrication and use, channels were designed with fewer side-channels (Fig. 6.8, B). One of these designs was produced using the soft-lithographic techniques described in other chapters of this dissertation. Trials with these channels revealed that a microfluidic platform enabling precise flow control would be needed for further testing

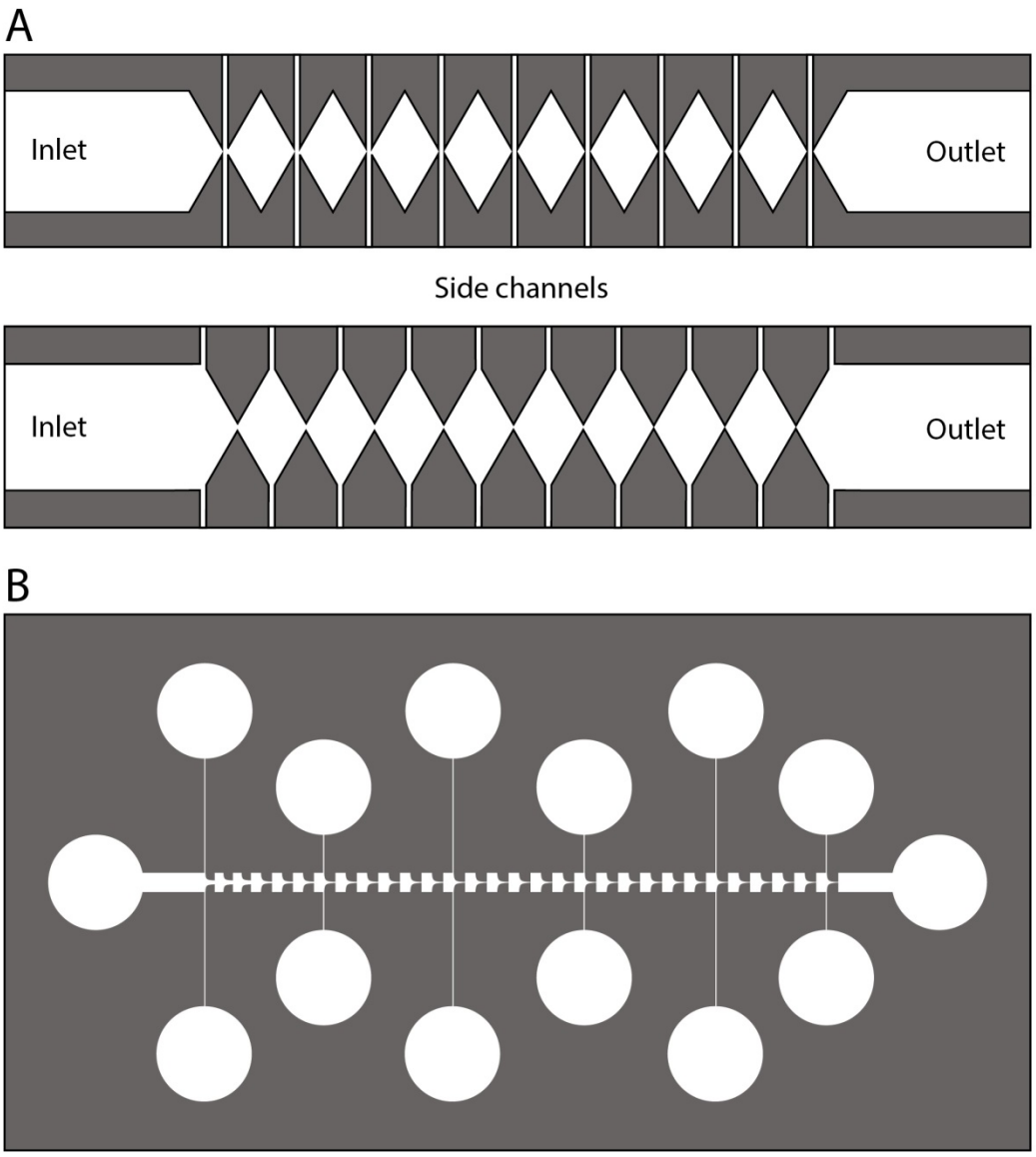

Figure 6.8. Illustration of g-iDEP channel designs with multiple outlets. Both sawtooth and tapered g-iDEP channels were designed with multiple outlets or side-channels. (A) These illustrations show two hypothetical approaches to implementation of side-channels in a sawtooth g-iDEP microchannel. Placing side-channels in the recesses between gates (lower image) would have less impact upon the values of e_c generated at the gate. Placing side-channels at the gate vertices would significantly impact e_c, but would facilitate collection of captured material. (B) This image shows a photomask design for one of two multiple-outlet g-iDEP microchannels that were fabricated in the laboratory. This instance utilized tapered gates. The other g-iDEP channel produced in this manner (not shown) featured sawtooth gates. For simplified fabrication and use, channels were designed with fewer side-channels.

Future work with such multiple-outlet g-iDEP microchannels would likely need to address flow control and the dispersion of captured analyte when transported into and through side-channels.

6.5 Summary and future directions

Moving forward, the utility of g-iDEP as a separations-based approach to bioanalysis will be determined by the traditional descriptors of separation science: resolution, dynamic range, and peak capacity. The first iterations of sawtooth g-iDEP microchannels have demonstrated a remarkable ability to both capture and discriminate between similar bioanalytes [9-11]. They have also demonstrated compatibility with a broad range of bioparticle types, including particles as diverse in size and character as proteins, viruses, and cells. However interesting these results may be, the ultimate goals of this approach reach far beyond single-analyte determinations.

Future research must further examine potential improvements and innovations for g-iDEP devices. These include optimization of experimental parameters, gate geometry and channel design, and integration of g-iDEP channels into larger, multiplexed microfluidic chips.

6.6 References

[1] Giddings, J. C., Dahlgren, K., *Separation Science* 1971, *6*, 345-356.

[2] Giddings, J. C., *Unified Separation Science*, Wiley-Interscience 1991.

[3] Jones, P. V., Hayes, M. A., *Electrophoresis* 2015, Accepted for publication.

[4] Chou, C., Tegenfeldt, J., Bakajin, O., Chan, S., Cox, E., Darnton, N., Duke, T., Austin, R., *Biophysical Journal* 2002, *83*, 2170-2179.

[5] Cummings, E., Singh, A., *Analytical Chemistry* 2003, *75*, 4724-4731.

[6] Chen, K. P., Pacheco, J. R., Hayes, M. A., Staton, S. J. R., *Electrophoresis* 2009, *30*, 1441-1448.

[7] Weiss, N. G., Jones, P. V., Mahanti, P., Chen, K. P., Taylor, T. J., Hayes, M. A., *Electrophoresis* 2011, n/a-n/a.

[8] Humble, P. H., Kelly, R. T., Woolley, A. T., Tolley, H. D., Lee, M. L., *Analytical Chemistry* 2004, *76*, 5641-5648.

[9] Jones, P. V., Staton, S. J. R., Hayes, M. A., *Analytical and Bioanalytical Chemistry* 2011, *401*, 2103-2111.

[10] Staton, S. J. R., Jones, P. V., Ku, G., Gilman, S. D., Kheterpal, I., Hayes, M. A., *Analyst* 2012, *137*, 3227.

[11] Jones, P. V., DeMichele, A. F., Kemp, L., Hayes, M. A., *Analytical and Bioanalytical Chemistry* 2014, *406*, 183-192.

CHAPTER 7

BIOPHYSICAL SEPARATION OF *STAPHYLOCOCCUS EPIDERMIDIS* STRAINS BASED ON ANTIBIOTIC RESISTANCE

7.1 Introduction

7.1.1 Antibiotic resistance in bacteria

In a process spanning vast chasms of time, bacteria have become fine-tuned for survival and genetic transmission [1]. Even amidst highly variable and seemingly inhospitable extremes of environment, they have adapted and spread. They are genetically agile—able to rapidly develop and exchange beneficial genomic alterations [2]. Bacteria have not only adapted in response to environments; they have adapted in response to other life forms. They have developed complex relationships with humans: relationships that span the range of commensalism, mutualism, and antagonism. One type of adaptation is resistance to antibiotics.

Even ancient humans benefited from natural antimicrobials and antibiotics. Archaeological evidence confirms the presence of tetracycline in the skeletal remains of ancient Sudanese Nubians [3]. The evidence indicates that population-wide benefits may have been gained from its consumption. Modern antibiotics first entered broad usage in the early 1930's, with the introduction of the synthetic sulfa compound, Prontosil. Meanwhile, Alexander Fleming was attempting to solve problems involved with the purification and stability of the active compound obtained from *Penicillium* mold. A team of Oxford researchers eventually resolved this issue, which led to the mass production of penicillin in 1945.

Resistance to sulfonamide compounds was first reported in the late 1930's. Even before the widespread usage of penicillin in the late 1940's, researchers noted that certain bacteria seemed to destroy it through enzymatic action [4]. Indeed, modern phylogenetic reconstructions indicate that many resistance genes are of ancient origin [5]. Regardless of provenance, antibiotic resistance now interferes significantly with the benefits humanity gains from antibiotics. Resistant strains result in prolonged illnesses and higher mortality rates [6]. National summary data from the Centers for Disease Control and Prevention indicate that each year in the United States, at least two million people acquire serious infections with antibiotic-resistant bacteria. At least 23,000 people die as a direct result of these infections and many more die from related complications [7].

The genus *Staphylococcus* is represented by some of the most notorious antibiotic resistant strains and species [8]. These bacteria are spherical, gram-positive, non-motile, facultative anaerobes that grow in characteristic clusters. They are typically classified as pathogenic or non-pathogenic based on production of the enzyme coagulase. Those possessing this enzyme produce a yellow pigment, giving rise to the name *Staphylococcus aureus.* This species is perhaps the most well-known of the genus. It is responsible for a variety of both acute and chronic infections that cause significant morbidity and mortality each year. *Staphylococcus epidermidis* does not produce coagulase, and colonies of this species remain unpigmented. It is generally less invasive than *S. aureus*. In fact, it is a normal and commensal resident of human skin and mucosa [9, 10]. In recent decades, *S. epidermidis* has increasingly emerged as a cause of multi-resistant nosocomial infections [11]. Immunocompromised patients, indwelling medical devices, and surgically implanted prostheses provide suitable environments for *S.*

epidermidis to propagate and form biofilms [12]. *S. epidermidis* exhibits high phenotypic and genotypic flexibility. These environments, combined with the selective pressure of antibiotics, have created an evolutionary niche for the development of highly adapted and successful strains of opportunistically pathogenic *S. epidermidis*. In recent years, it has become the most common cause of medical device-associated colonization and infection [13].

Strains of *S. epidermidis* have developed resistance to many antibiotics. This research focuses on gentamicin resistance in *S. epidermidis*. Gentamicin is a common aminoglycoside antibiotic. Its mechanism of action (common to all aminoglycosides) results from binding to the 16S subunit of the bacteria's ribosomal RNA (rRNA) and disrupting the protein-proofreading function. Mistranslated proteins interfere with proper cellular function. Insertion of mistranslated proteins into the cell membrane allows leakage, which in turn allows more antibiotic to enter the cell. Accumulation of mistranslated proteins eventually leads to cell death.

In general, antibiotic resistance occurs through one or more of four pathways. These include modification of the antibiotic's target, modification or degradation of the antibiotic, reduction of the cellular concentration of antibiotic (either by decreasing cell permeability or by increasing efflux), and bypassing the antibiotic's target through an alternate metabolic pathway [14]. Many aspects of gentamicin resistance have been investigated and reported in the literature, including genes responsible and their expression products. Aminoglycoside resistance in gram-positive bacteria occurs through the modification of antibiotic via aminoglycoside-modifying enzymes. Many such enzymes exist, with various modifications and locations of these modifications on the

antibiotic. While the specific case of *Staphylococcus epidermidis* resistance to gentamicin has not been well characterized, gentamicin resistance in *Staphylococcus* in general has been attributed to three specific enzymes: an acetyltransferase, a phosphotransferase, and an adenyltransferase. The enzymes may be present individually or together. Most often, the production of a bifunctional enzyme AAC(6')-APH(2'') from the gene *aac*(6')-*aph*(2'') is responsible for gentamicin resistance [15]. The possible mechanisms of resistance in these bacteria must then be a result of changes due to the expression of these enzymes.

Bacteria readily share beneficial DNA through horizontal gene transfer [16]. Many resistance genes are encoded in plasmid DNA. Transfer of resistance to multiple compounds has been shown to occur through plasmid exchange in natural environments, even between phylogenetically diverse populations [17]. It is reasonable to assume that resistance mechanisms found in other bacteria, and especially in other *Staphylococci*, are found in *S. epidermidis* as well.

It is plausible that these enzymes affect the electrostatic and dielectric properties of the bacteria. Biological material in all shapes and sizes is composed of electrostatically interacting atoms, molecules, polymers, and other higher-order structures. Hypothetically, even net-neutral biological particles will possess a unique distribution of charge. The electrostatic, dipolar, and multipolar diversity of all matter presents a valuable mode of manipulation and separation, which is exploited here for the separation of antibiotic-resistant and susceptible bacteria (Fig. 7.1).

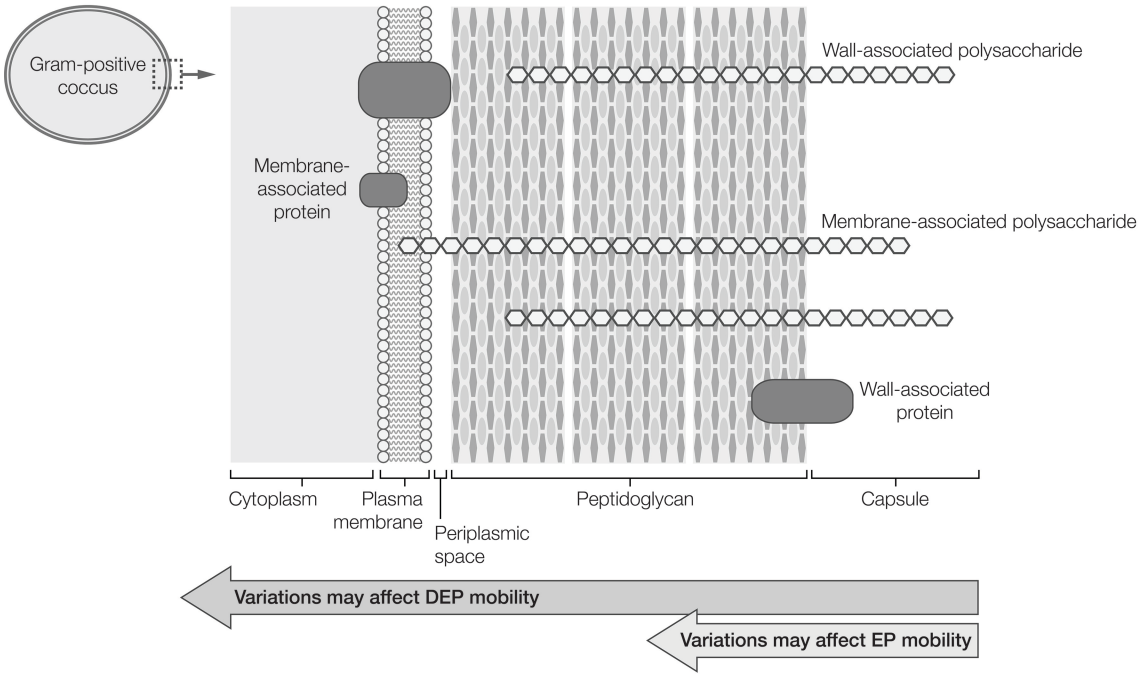

Figure 7.1. Basic illustration of a gram-positive bacterium. Certain simplified physical components of the bacterium are listed. Changes in any of these components could alter the effective electrostatic and dielectric properties of the cell. The possible effect of these changes on EK and DEP forces are categorized and listed.

7.1.2 Electrokinetic forces used for separations

Various electrophoretic and dielectrophoretic methods have been used for cell separation [18-20]. Dielectrophoresis has been used for a number of separations. Some examples include separating cancer cells, stem cells, different bacterial cells, infected and healthy red blood cells, platelets and whole blood, and fetal cells from maternal blood [21-23]. It can also be used to separate viable from nonviable cells, as has been shown with both yeast and bacteria [24]. In this last case, the difference in membrane conductivity was assigned as the reason for separation.

The work reported in this chapter is focused on applying gradient insulator-based dielectrophoresis (g-iDEP) to high-resolution separation of pathogens (Fig. 7.2). The

mechanism and forces are described in other chapters and referenced works [25-29]. In assessing the work here, the most important relationship is $\frac{\nabla|\boldsymbol{E}|^2 \cdot \boldsymbol{E}}{E^2} = \frac{\mu_{\mathrm{EK}}}{\mu_{\mathrm{DEP}}}$, which occurs at the balance or focusing point for the particles, and $\boldsymbol{E}$ is the electric field vector.

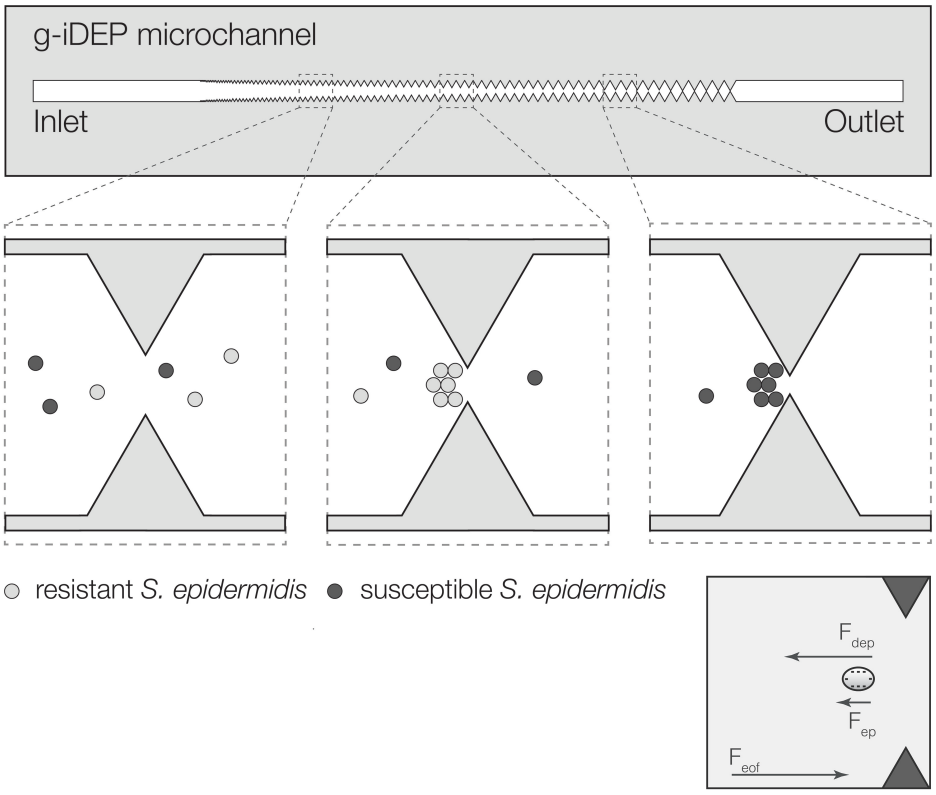

Figure 7.2. Overview of microchannel geometry used for capture. (Top) Conceptual illustration of g-iDEP device and expected capture behavior for *S. epidermidis* resulting from a superposition of opposing forces. The g-iDEP microchannel is patterned in insulating materials and constructed using soft lithography. The geometry consists of a sawtooth pattern: constrictions of gradually decreasing pitch formed by approaching apices of equilateral triangular units. (Middle) Different analytes are expected to capture at unique gates based upon their characteristic EK and DEP properties. In this case, both analytes pass the initial, large-pitched gates unhindered since EK force exceeds DEP force for both types. When gates become sufficiently small-pitched, EK force is overcome by DEP force for one of the two analytes, causing selective capture and concentration. The remaining analyte will continue to progress down-channel. Eventually EK force is overcome by DEP force for the second analyte, resulting in its capture. (Bottom) This shows a basic illustration of relative EK and DEP forces expected to act upon a bacterium traveling along the channel centerline.

7.1.3 Significance of g-iDEP separations

Current clinical approaches to determination of antibiotic resistance often require two or more days to obtain results. One such example is disk diffusion, in which the growth of bacteria is measured in the presence of antibiotic. Many methods such as this rely on treating the bacteria with antibiotics, then observing colony growth patterns [30]. These time-consuming processes sometimes result in "treat first, ask later" situations where broad-spectrum antibiotics are used for acute treatment before the particulars of pathology are understood. As laboratory results are obtained, or the patient does not improve, other (more appropriate) drugs are used. This approach bolsters populations of antibiotic resistant strains and generally leads to suboptimal outcomes for patients (including increased mortality rates) [31-33].

The work reported in this chapter demonstrates rapid and reproducible differentiation of gentamicin-resistant and gentamicin-susceptible strains of *S. epidermidis*. With appropriate channel design, simultaneous spatial separation and concentration of these bacterial strains is achievable. This work represents significant progress in demonstrating the ability of g-iDEP to separate nearly-identical pathogens.

7.2 Materials and methods

7.2.1 Microdevice fabrication

Two versions of a sawtooth microchannel were used in these experiments: one for single-strain experiments (V1), and another for two-strain separations (V2a). V1 has been described in detail [25-29]. The development of V2a was described in Chapter 6. For channel V1, the channel length, width, and depth were 4.1 cm, 1000 μm, and 14 ± 1 μm

(average between templates), respectively. The initial gate height was 945 μm and the final was 27 μm. For channel V2a, the channel length, width, and depth were 4.2 cm, 1000 μm, and 20 μm, respectively. The initial gate pitch was 73 μm, and the final gate pitch was 25 μm.

Template wafers for the V1 microchannels were fabricated using the same procedures described in Chapters 3. For the V2a microchannels, Si wafers were coated with AZ 4330 photoresist (AZ Electronic Materials, Branchburg, NJ). Photoresist was exposed using a glass chrome mask produced by JD Photo-Tools (United Kingdom). After developing, wafers were etched using reactive ion etching (ICP etcher, SPTS, San Jose, CA), with SF_6 gas and C_4F_8 gas.

The template wafers for both V1 and V2a were used to create PDMS casts as described in Chapter 3. The PDMS casts and glass coverplates were then treated with oxygen plasma in a plasma cleaner (PDC-32G, Harrick Plasma, Ithaca, NY). Treatment with oxygen plasma lasted for 60 seconds at 18W. The PDMS and glass were then allowed to seal upon contact.

7.2.2 Cell culture and labeling

Two strains of *Staphylococcus epidermidis* were obtained, including gentamicin resistant (ATCC 35983) and gentamicin sensitive (ATCC 14990) strains. *S. epidermidis* seed stock was stored in tryptic soy broth (TSB) with 10% glycerol at −80°C. Aliquots of 8 mL sterile TSB were placed in culture tubes. Each tube was inoculated with one of the strains then placed in a shaker/incubator and allowed to grow overnight at 37°C. Cultures reached late log phase, with a cell concentration of approximately 10^9 CFU/mL. Following incubation, a 1:10 dilution of each cell culture was centrifuged at 4000 g for 3

minutes. After discarding the supernatant, the cell pellet was resuspended in 1 mL of 2 mM phosphate buffer (PB), pH 7.4, by agitation with a vortexer ensuring redispersion of cells. This process was repeated three times in order to remove all of the TSB.

For single-strain experiments, cells were labeled using Vybrant DiO fluorescent dye (Invitrogen). Excitation and emission wavelengths for this dye are 484 and 501 nm. The labeling procedure was the same as that described in Section 4.2.2. After labeling was complete, cells were examined using bright field and fluorescence microscopy to ensure that they were both dispersed and intact.

For two-strain separations, each strain of *S. epidermidis* was separately labeled with either NHS-rhodamine or NHS-fluorescein (respective excitation/emission wavelengths: 552/575 nm and 494/518 nm). In each case, 1 mg of dye was first dissolved in 100 µL dimethylsulfoxide. A 20-µL aliquot of this mixture was added to 1 mL of washed and suspended bacterial cells. This suspension was incubated in a 37°C water bath for 20 minutes before washing the cells as described above, and finally suspending them in 1 mL PB with BSA.

7.2.3 Experimental

The experimental equipment and set-up are the same as those described in Section 4.2.3. In all experiments, bacteria were captured in phosphate buffer (PB) with BSA. The conductivities of these solutions were approximately 343 µS/cm. For single-strain experiments, DC potentials applied across the device ranged from 0 – 3000 V in 100 V increments. For dual-strain experiments, DC potentials ranged from 800 – 1200 V in 100 V increments.

For the single-strain experiments, still images and video were collected with a monochrome QICAM cooled CCD camera (QImaging, Inc., Surrey, BC) and Streampix V image capture software (Norpix, Inc., Montreal, QC). For the dual-strain separations, color video data was captured using an iPhone 5S camera. Software included Apple iPhoto for retrieving data from the device, ImageJ for file conversion and fluorescence intensity analysis, and Adobe Photoshop for assembly of channel-wide photo mosaics.

The data were obtained over a period of several months. PDMS casts were kept in airtight plastic bags in the freezer for up to two weeks before use. Casts were bonded to their glass coverplate on the same day they were used for experiments, and were discarded after use. Bacterial preparations were typically labeled and used the day after inoculation and incubation. Prior to fluorescence intensity analysis, the collected imaging datasets were examined to find those showing the least degree of bacterial aggregation and device fouling. For each strain, at least four datasets were used, with each dataset representing separate device and bacterial preparation.

7.2.4 Mathematical modeling of device

Finite element, multiphysics software (COMSOL, Inc., Burlington, MA) was used to model the electric field within the microchannel. The parameters and process were the same as those presented in section 3.2.5 and Appendix A.

7.2.5 Safety considerations

Organisms used in this experiment were Biosafety Level (BSL) I or II. All experiments were carried out in an approved BSL II laboratory within accordance to the current version of the CDC/NIH BMBL publication.

7.3 Results

The electrokinetic and dielectrophoretic behavior of two strains of *S. epidermidis* were investigated with g-iDEP. Two sets of experiments were performed. The first set of experiments involved single strains in separate V1 devices and varied the applied potential. When varying the applied voltage, in V1 microchannels, capture only occurred at the ultimate or penultimate sets of gates. This design was well-suited for single-gate, single-analyte experiments. The second set of experiments involved two strains in V2a microchannels, observed with differential labeling.

As described in Chapter 6, the V2a microchannels feature more incremental stair-steps between sets of gates and were used for simultaneous dual-analyte separation. The gradual decreases in gate size produce smaller increases in local force maxima and increase the resolving capabilities of the channel [34].

7.3.1. Single-strain experiments

Within V1 microchannels, the electrokinetic and dielectrophoretic behaviors of both gentamicin-resistant and gentamicin-susceptible *S. epidermidis* were examined at the final set of gates (27-μm pitch). No capture was observed at gates with pitch greater than 90 μm. The magnitude (V_A) and duration (t_A) of the applied electric potential were varied. The overall behavior of the bacteria was consistent with the results of previous work using gates of similar geometry. Upon application of an electric potential within the device, motion of all analyte was directed towards the outlet (cathode) reservoir, consistent with EOF-dominated transport. At the gate of interest, capture resulted in the formation of crescent-shaped bands of material, localized immediately upstream (within a few micrometers) of the gate's transverse axis (Fig. 7.3, left).

The amount of material that accumulated within the capture zone depended upon both the magnitude and duration of applied potential. Accumulation within the capture zone was quantified by integrating fluorescence intensity (*FI*) across a small region of interest (ROI) centered at the point of typical band formation. Below strain-specific threshold values (c) of V_A, no capture occurred, even over extended periods of time. Above this threshold value of V_A, material continued to accumulate as long as potential was maintained. Under these conditions, *FI* within the ROI increased linearly with t_A (Fig. 7.3, right).

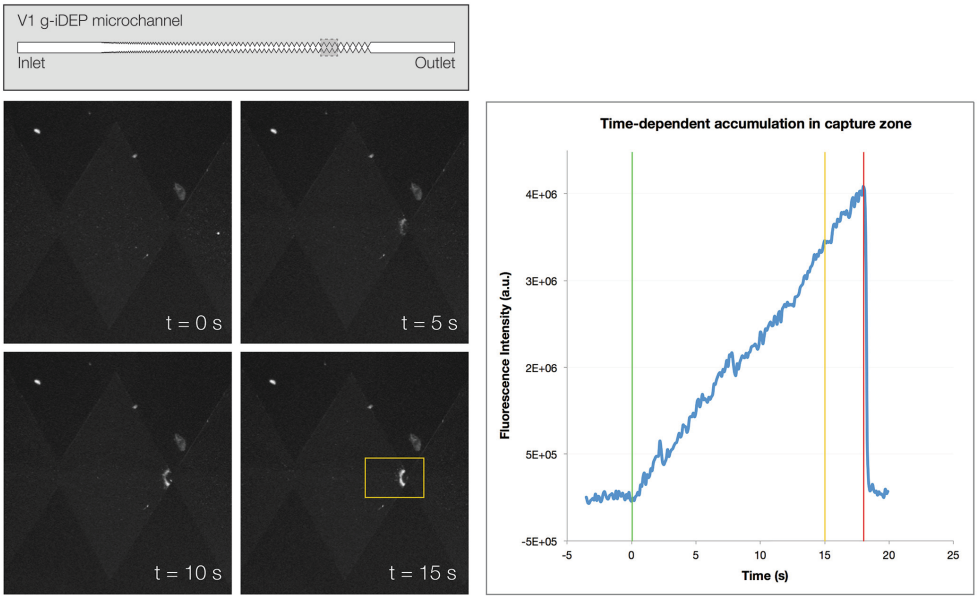

Figure 7.3. Capture of gentamicin-resistant *S. epidermidis* at a 27-µm gate within a V1 microchannel. Material is captured and concentrated in tight, crescent-shaped bands near the gate. Above the threshold value of V_A required for capture, bacteria collect continuously as long as potential is applied. (Left) Images show capture at four different time points when V_A = 1200 V. ROI is framed in yellow for the bottom left image. (Right) Integrated fluorescence intensity over the ROI shows steady accumulation of bacteria. The green line indicates t_A = 0 s, or the point when potential was applied. The yellow line indicates t_A = 15 s, or the point at which FI was measured for subsequent analysis of V_A-dependence of capture. The red line indicates the point at which potential was removed.

Data was examined at a consistent time point (t_A = 15 s, yellow line in Fig. 7.3, right) across a range of voltages from 100 to 2000 V in 100-V increments, for both strains of *S. epidermidis* (Fig 7.4). Integrated *FI* values for the ROI were divided by the mean *FI* signal for individual, labeled bacteria in order to convert these values to an approximate particle count (*N*).

Because there is a region at low values of V_A where no capture occurs, it is informative to identify an equation that accounts for this region and the threshold ($V_A = c$) above which capture occurs. When the applied voltage was sufficient to generate trapping force, *N* departed from baseline values. As V_A increased ($V_A > c$), the amount of material accumulated during the 15-s window increased. This yielded a predominantly linear, positive slope for particle count at values of V_A greater than *c*. This behavior is well described by a piecewise function, where the *y*-axis represents *N*, and the *x*-axis represents V_A. The line describing increasing *N* departs from the baseline at $V_A = c$.

$$N(V_A) = \begin{cases} 0 & if\ V_A < c \\ m(V_A - c) & if\ V_A \geq c \end{cases} \quad (1)$$

Assuming that a large proportion of the particle population is successfully trapped within a capture zone, the slope of this line (*m*) is primarily related to the rate of analyte delivery to the gate. The specific value of *c* is related to the values of μ_{EK} and μ_{DEP} intrinsic to an analyte population, and can be described in relation to the electric field parameters in terms of the ratio of the two mobilities (μ_{EK}/μ_{DEP}).

By fitting the piecewise function (Eq. 1) to the experimental data, we can determine a specific value of *c* for each bacterial strain. First, baseline values were

established for each strain by averaging the results measured from 100 – 400 V. Next, a set of data points was selected for linear regression analysis of the sloped region. Significance of capture was noted when mean values for N reached magnitudes 2σ above

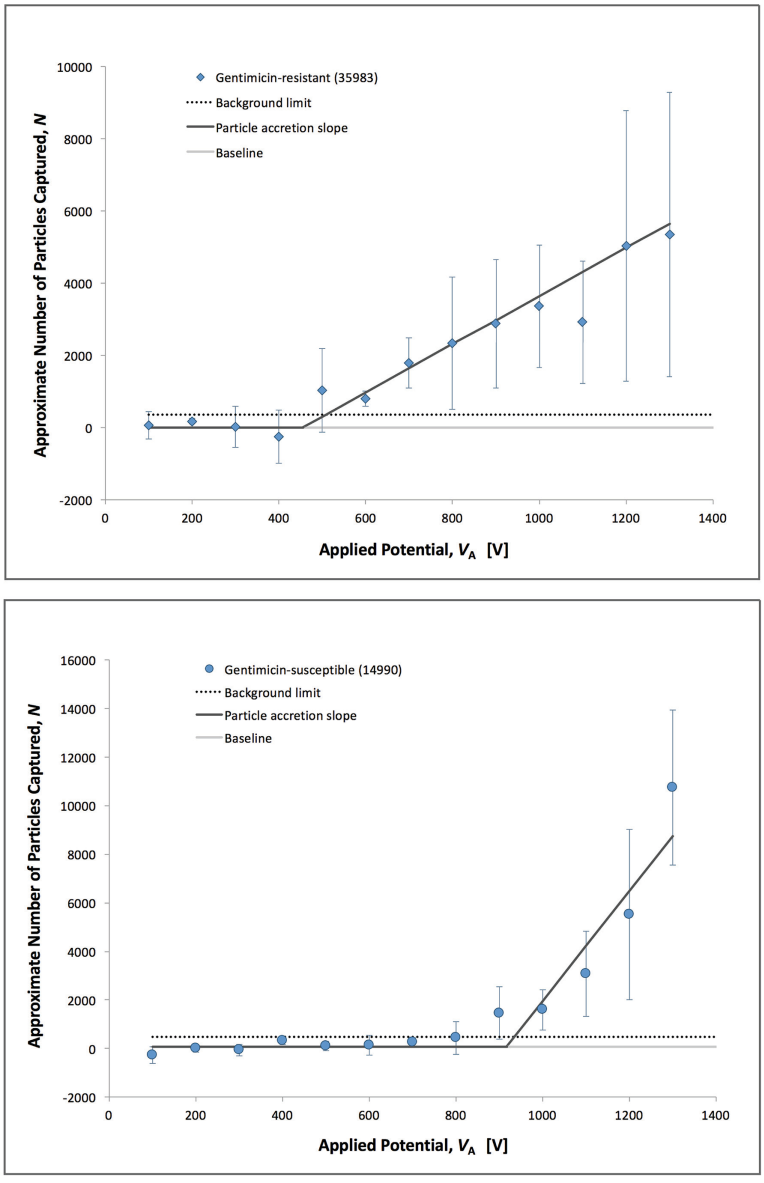

Figure 7.4. Plots of captured particle count. For both gentamicin-resistant (top) and gentamicin-susceptible (bottom) *S. epidermidis*, with increasing applied potentials (V_A). All data was collected at a 27-µm gate on V1 microchannels, with a duration of applied potential (t_A) of 15 seconds. Accumulation was noted when particle count exceeded the background limit (twice the standard deviation of baseline data points).

the baseline. The slope and intercept of these lines were used to determine the rate of particle accumulation and extrapolate values for *c* where the accumulation slope intersected the baseline. In this manner, values for *c* were determined to be 443 ± 59 and 881 ± 38 for the resistant and susceptible strains, respectively. Using COMSOL models, the equivalent ratio was determined to be $4.6\pm0.6\times10^{9}$ V/m^2 for the resistant strain versus $9.2\pm0.4\times10^{9}$ V/m^2 For the susceptible strain.

7.3.2 Dual-strain experiments

The V2 microchannels were used for a simultaneous study of gentamicin-resistant and susceptible *S. epidermidis*. The motion of bacteria upon application of an electric potential was toward the outlet (cathode) reservoir, again consistent with EOF-dominated particle conveyance. Values of V_A ranged between 800 and 1200 V in 100-V increments. In each experiment, significant differences in behavior were noted for the resistant (red-labeled) and susceptible (green-labeled) bacteria (Fig. 7.5). There was a distinct capture of red particles at larger gate pitch and green at smaller pitches. There was considerable spread in the loci of collection and notable overlap where both red and green were observed at some gates. These general observations held for all V_A where capture was observed, with capture occurring at smaller gates with lower V_A. The largest differentiation between strains was observed at V_A = 1000 V. The observed capture behaviors were consistent with the findings from single-strain experiments. Namely, the strain exhibiting lower mobility ratio (gentamicin-resistant) was captured at larger-pitch gates relative to the strain exhibiting higher mobility ratio, which was captured at smaller-pitch gates for any given value of V_A.

7.4 Discussion

A new micro-scale separation technique was used to generate high-resolution isolation and concentration of gentamicin-resistant and gentamicin-susceptible strains of *Staphylococcus epidermidis*. By most metrics these two strains are phenotypically

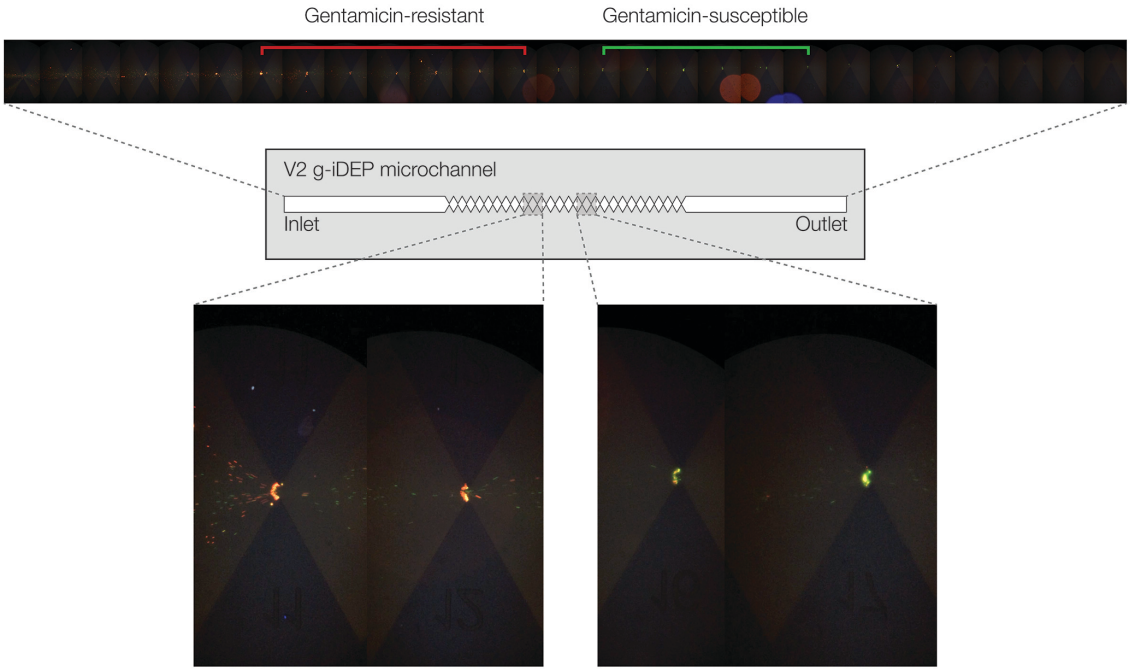

Figure 7.5. Images showing simultaneous capture and concentration. Plots of gentamicin-resistant (red) and gentamicin-susceptible (green) *S. epidermidis* within separate regions of a single microchannel. (Top) An image mosaic of the V2 microchannel shows that capture is distributed across several gates for each strain. Approximately 8 gates separate the mean gate position for each strain's region of capture, with mixing at some of the intervening gates. (Bottom) Detailed images taken from different regions of the channel show the formation of selective capture zones for each strain.

identical, thus presenting a significant challenge to traditional analytical separation techniques. Using g-iDEP microchannels, the strains were first electrokinetically differentiated and largely separated within a single channel. The characteristic separation times spanned a few seconds to a few minutes time. This data supports the concept that

complex bioparticles can be identified by their electrical properties in short periods of time and for low-abundance samples. This approach could transform current medical diagnostics by eliminating the need for time-consuming steps (culturing, genotyping, resistance panels, etc.) in the clinical pathology workflow.

This concept is supported by both interrogations. In single-strain experiments, the relationship between capture and applied voltage was examined for both gentamicin-resistant and gentamicin-susceptible *S. epidermidis* at a single gate. These relationships revealed a significant difference in V_A required for capture of each strain. Calculated values for c were 443 ± 59 and 881 ± 38 for the resistant and susceptible strains, respectively. These values for c correspond to μ_{EK}/μ_{DEP} values of $4.6\pm0.6\times10^9$ V/m^2 and $9.2\pm0.4\times10^9$ V/m^2. This difference indicates that the two analytes' ratios of μ_{EK}/μ_{DEP} are sufficiently distinct for separation.

Examining V_A-dependent capture data demonstrates that a piecewise function can effectively approximate the relationship. Mathematical modeling helps reveal quantitative criteria for analyte differentiation, based on plots of FI as a function of V_A. Two analytes could prove differentiable if they exhibit different points of discontinuity or threshold for capture ($V_A = c$). This difference would indicate that the two analytes' ratios of μ_{EK}/μ_{DEP} are sufficiently distinct for separation. Interestingly, the analytes could still prove differentiable if they shared the same value for c, but different accretion slopes for $V_A > c$. In this latter scenario, electrokinetic velocity of the two analytes would serve as the primary differentiating factor.

The dual-strain experiments demonstrate a proof-of-principle separation of the two strains within a single g-iDEP microchannel. These experiments revealed

significantly different loci of capture for the two strains within V2 microchannels. Qualitatively, the observed order of capture within the V2 microchannels (gentamicin-resistant at larger-pitch gates (red labeled) and gentamicin susceptible (green labeled) at smaller-pitch gates) corresponds with inferences drawn from the single-strain data regarding relative electrokinetic and dielectrophoretic mobilities. Thus, the ratio μ_{EK}/μ_{DEP} is expected to be larger for gentamicin-susceptible than for gentamicin-resistant *S. epidermidis*. The separation was not complete; there were overlapping zones with some admixture of the two strains. However, this does not reflect limitations to the technique, but in the current 'first generation' designs. These limitations and their reduction are discussed below.

In these experiments, a distinct and statistically significant difference was observed between the behavior of gentamicin-resistant and gentamicin-susceptible *S. epidermidis*. The physical and structural differences associated with gentamicin resistance and susceptibility may be subtle, but they are sufficient to facilitate separation. The physical origins and effects stem from the structural and molecular elements of cells. In gram-positive cocci such as *S. epidermidis* the cell envelope primarily consists of two layers: an outer, thick peptidoglycan layer and an inner cell membrane (Figure 2). Sandwiched between these two layers is a thin periplasmic space. Electromotive forces depend upon complex and subtle variables; bacteria and other cells are especially complex entities from an electrophysical point of view. They consist of multiple subdomains that all possess independent or semi-independent electric and dielectric properties [35]. These subdomains are never spherical, lossless, or isotropic (as is often presumed for theoretical treatment of electrokinetic forces). Living cells, for instance,

consist of multiple aqueous regions separated by semipermeable membranes. The lipid membrane itself is composed of polar molecules and contains highly peripatetic membrane-bound proteins. Internal structures such as the cytoskeleton and organelles are also polarizable, mobile or semi-mobile, and likely contribute to the overall multipolar character of the cell. These characteristics can vary between biological targets, even based on slight differences in genotype.

Changes in surface features such as the peptidoglycan layer, surface-expressed proteins, or teichoic acids are likely to influence electrophoretic mobility [36]. Constituents of the cell wall (including proteins, lipids, and polysaccharides), the permeability of the cell wall, and internal cytoplasmic structures are all likely to affect dielectrophoretic mobility. One direct mechanism for physical cellular change could be overexpression of the AAC(6')-APH(2'') bifunctional enzyme. The isoelectric points of AAC(6') and APH(2'') have been shown to range from approximately 5 to 8 [37]. This differs greatly from the pI of *S. epidermidis*, which is 2.3 [38]. If these are expressed on the cell surface, there could be a direct electrophoretic effect since the pI of the bacteria would be significantly altered. It is noteworthy that osmotic shock studies with resistant *E. coli* bacteria indicate some gentamicin resistance-conferring enzymes may be more concentrated within the cell envelope, in particular the periplasmic space [39].

Recognizing that subtle changes in a cell's envelope, inner structure, overall shape, or deformability can result in a unique net force on that cell, it is reasonable to expect genetically or phenotypically distinct strains to behave differently in response to electric fields. The complex dielectric characteristics of a biological cell and its interactions with the surrounding medium are approximated by an experimental or

effective value for the Clausius-Mossotti factor (f_{CM}), which is an important component of the dielectrophoretic force equation. The smallest theoretically resolvable difference for the f_{CM} is about one part in 10^5 under the conditions of these experiments [34]. If presumed to represent only changes in effective cell conductivity [29], this could translate to changes as small as a few μS/m. Castellarnau et al. estimated that cell wall and membrane conductivities vary up to 70% for isogenic mutants of a single strain of *E. coli* [40]. Based their results, previous g-iDEP results with strains of *E. coli*, and theoretical resolution estimates, the observed differences in electromotive behavior can reasonably be attributed to mechanisms associated with gentamicin resistance in *S. epidermidis*.

The data were obtained over several months, on many devices, and by different operators. While the assessed error appears to be large, it does not preclude establishing initiation of capture (c) and approximating a slope (m) of N vs V_A, the key elements of this study. Variations between experimental sessions in the following parameters may contribute to the spread: specific bacterial cells counts, staining efficiency, photobleaching, and slight pressure-driven or electroosmotic flow bias. The effects of these variables are compounded by the amount of material captured and measured at the ROI. Thus the standard deviation appears to increase proportionally with V_A.

For dual-strain experiments, these sources of variability also hold. These can be attributed largely to two phenomena: the increased resolution capability of the V2 channels compared to the V1 channels, and low capture efficiency at any given gate. The latter results from the dispersive effect of transverse electric field inhomogeneity, especially across the gate axis. This inhomogeneity is a consequence of the formation of

extremely high gradient zones in the immediate vicinity of sharp geometric features. This lateral field inhomogeneity is being addressed with new device designs that will minimize these particular effects.

At high values of V_A, detrimental and interfering effects are introduced by Joule heating and bubble formation. With alternative experimental or device design, capture could be achieved with lower applied potential; this would require either smaller gate pitch or a reduction in EK velocity.

With adequate resolution and dynamic range, it is reasonable to expect that a g-iDEP microchannel does generate unique loci for separation and concentration of multiple bioanalytes. Furthermore, these bioanalytes may range from dissimilar to similar, spanning a variety of clinically important targets. The present implementation of g-iDEP has already shown sufficient resolution for differentiating pathogenic and non-pathogenic strains of *E. coli*. The results presented here break new ground by differentiating and separating bacteria based upon their antibiotic susceptibility. While the physical forces at work are unlikely sufficient to observe simple mutations in the genetic code, it is plausible that any expressed gene product will alter the physicochemical parameters of the cell in a sufficient manner to effect separation. With the potential for extremely high resolution and large dynamic range, this strategy will create a new and extremely valuable tool for identifying and isolating pathogens. Additionally, this tool could be used as a powerful preparative step for other traditional modes of characterization. In these cases, g-iDEP would offer improved results obtained from traditional methods by first removing interfering components and concentrating the target.

7.5 Conclusion

Using two types of sawtooth-patterned g-iDEP microchannels, this work demonstrates both differentiation and spatial resolution of gentamicin-resistant and gentamicin-susceptible *S. epidermidis*. Importantly, this is achieved using DC fields and easily achievable values of applied potential.

Previous work by the authors has demonstrated differentiation of similar bioparticles, including pathogenic and non-pathogenic strains of *E. coli*. This research represents a refinement of the existing technique, and introduces the use of a higher-resolution g-iDEP sawtooth microchannel to effect the separation. These results bear significant implications for the future of clinical analytics and diagnostics. Additional modeling and refinements of g-iDEP microchannel geometry will improve the resolution and capabilities of this technique.

7.6 References

[1] Ochman, H., Lawrence, J. G., Groisman, E. A., *Nature* 2000, *405*, 299-304.

[2] Malachowa, N., DeLeo, F. R., *Cellular and molecular life sciences : CMLS* 2010, *67*, 3057-3071.

[3] Nelson, M. L., Dinardo, A., Hochberg, J., Armelagos, G. J., *American Journal of Physical Anthropology* 2010, *143*, 151-154.

[4] Abraham, E. P., Chain, E., *Nature* 1940, *146*, 837-837.

[5] Aminov, R. I., Mackie, R. I., *FEMS microbiology letters* 2007, *271*, 147-161.

[6] Cosgrove, S. E., *Clinical Infectious Diseases* 2006, *42*, S82-S89.

[7] Division of Healthcare Quality Promotion, National Center for HIV/AIDS Viral Hepatitis STD and TB Prevention, National Center for Immunization and Respiratory Diseases (NCIRD), Atlanta, GA 2013.

[8] Davies, J., Davies, D., *Microbiology and Molecular Biology Reviews* 2010, *74*, 417-433.

[9] Kloos, W. E., Musselwhite, M. S., *Applied Microbiology* 1975, *30*, 381-395.

[10] Grice, E. A., Segre, J. A., *Nature reviews. Microbiology* 2011, *9*, 244-253.

[11] Vuong, C., Otto, M., *Microbes and infection / Institut Pasteur* 2002, *4*, 481-489.

[12] Uçkay, I., Pittet, D., Vaudaux, P., Sax, H., Lew, D., Waldvogel, F., *Annals of Medicine* 2009, *41*, 109-119.

[13] Otto, M., *Nature reviews. Microbiology* 2009, *7*, 555-567.

[14] Wright, G. D., *Chemical communications (Cambridge, England)* 2011, *47*, 4055-4061.

[15] Miller, G. H., Sabatelli, F. J., Hare, R. S., Glupczynski, Y., Mackey, P., Shlaes, D., Shimizu, K., Shaw, K. J., Bauernfeind, A., Schweighart, S., Shannon, K., Patzer, J., Molinari, G., Schito, G. C., GomezLus, R., GomezLus, S., Ferreira, H., Sousa, J. C., Vaz, M., Collatz, E., Bismuth, R., Lambert, T., Courvalin, P., Minozzi, C., Klugman, K., Bilgeri, Y., Giamarellou, H., Petrikkos, G., Akalin, H., Gur, D., Woloj, M., Rossi, A., Casellas, J., Tokumoto, M., Couto, E., Juliet, C., Pinto, M. E., Zemelman, R., Pedreira, W., Fernandez, M., Leal, I., Guzman, M., Murillo, J., Isturiz, P., Merentes, A., Bremner, A., Ho, B., Mayer, K., Ellal, J., Fu, W., Zhu, D., Dornbusch, K., Goransson, E., *Clinical Infectious Diseases* 1997, *24*, S46-S62.

[16] Davison, J., *Plasmid* 1999, *42*, 73-91.

[17] Kruse, H., Sørum, H., *Applied and environmental microbiology* 1994, *60*, 4015-4021.

[18] Huang, L. R., Cox, E. C., Austin, R. H., Sturm, J. C., 2004, *304*, 987-990.

[19] Neirinck, B., Van der Biest, O., Vleugels, J., *Journal Of Physical Chemistry B* 2013, *117*, 1516-1526.

[20] Šalplachta, J., Kubesová, A., Horká, M., *Proteomics* 2012, *12*, 2927-2936.

[21] Gagnon, Z. R., *Electrophoresis* 2011, *32*, 2466-2487.

[22] Demircan, Y., Özgür, E., Külah, H., *Electrophoresis* 2013, *34*, 1008-1027.

[23] Çetin, B., Li, D., *Electrophoresis* 2011, *32*, 2410-2427.

[24] Yang, L., *Analytical Letters* 2012.

[25] Pysher, M. D., Hayes, M. A., *Analytical Chemistry* 2007, *79*, 4552-4557.

[26] Staton, S. J. R., Chen, K. P., Taylor, T. J., Pacheco, J. R., Hayes, M. A., *Electrophoresis* 2010, *31*, 3634-3641.

[27] Jones, P. V., Staton, S. J. R., Hayes, M. A., *Analytical and Bioanalytical Chemistry* 2011, *401*, 2103-2111.

[28] Staton, S. J. R., Jones, P. V., Ku, G., Gilman, S. D., Kheterpal, I., Hayes, M. A., *Analyst* 2012, *137*, 3227-3229.

[29] Jones, P. V., DeMichele, A. F., Kemp, L., Hayes, M. A., *Analytical and Bioanalytical Chemistry* 2014, *406*, 183-192.

[30] Jorgensen, J. H., Ferraro, M. J., *Clinical Infectious Diseases* 2009, *49*, 1749-1755.

[31] Ibrahim, E. H., Sherman, G., Ward, S., Fraser, V. J., Kollef, M. H., *Chest* 2000, *118*, 146-155.

[32] Iregui, M., Ward, S., Sherman, G., Fraser, V. J., Kollef, M. H., *Chest* 2002, *122*, 262-268.

[33] Lodise, T. P., McKinnon, P. S., Swiderski, L., Rybak, M. J., *Clinical Infectious Diseases* 2003, *36*, 1418-1423.

[34] Jones, P. V., Hayes, M. A., *Electrophoresis* 2015, Accepted for publication.

[35] Govindarajan, S., Nevo-Dinur, K., Amster-Choder, O., *FEMS microbiology reviews* 2012, *36*, 1005-1022.

[36] Sonohara, R., Muramatsu, N., Ohshima, H., Kondo, T., *Biophysical chemistry* 1995, *55*, 273-277.

[37] Le Goffic, F., Martel, A., Moreau, N., Capmau, M. L., Soussy, C. J., Duval, J., *Antimicrobial Agents and Chemotherapy* 1977, *12*, 26-30.

[38] Horká, M., Kubícek, O., Růzicka, F., Holá, V., Malinovská, I., Slais, K., *Journal of Chromatography A* 2007, *1155*, 164-171.

[39] Williams, J. W., Northrop, D. B., *Biochemistry* 1976, *15*, 125-131.

[40] Castellarnau, M., Errachid, A., Madrid, C., Juarez, A., Samitier, J., *Biophysical Journal* 2006, *91*, 3937-3945.

CHAPTER 8

SUMMARY AND CONCLUSIONS

8.1 Dielectrophoretic Separations

In recent decades, dielectrophoresis (DEP) has emerged as an important tool for manipulating bioparticles as well as quantifying certain biophysical parameters. Dielectrophoretic approaches to sample handling and analysis are richly varied. These approaches have proven uniquely well-suited for a wide range of bioparticles including proteins, viruses, and cells. Certain implementations of DEP (particularly those using AC DEP with quadrupole electrode arrangements) have demonstrated a remarkable ability to distinguish similar analytes based on their crossover frequency. These finely-tuned quantifications demonstrate impressive ability, but lack the advantages afforded by analytical separation science. Separation-based approaches offer the ability to simultaneously separate and concentrate analyte, enable high-throughput analysis, and handle complex samples.

By adapting dielectrophoresis to a separation-based design, gradient insulator dielectrophoresis (g-iDEP) promises the ability to rapidly and specifically separate extremely similar bioparticles, with the additional benefit of compatibility with complex and native samples. Rapid, high-resolution, and high-throughput biophysical characterizations are on the horizon. The work presented in this dissertation demonstrates the ability to capture and concentrate target bioparticles from complex, native samples such as whole blood (Chapter 3). Also demonstrated is differentiation and separation of very similar cells in g-iDEP microchannels (Chapters 4 and 7). Importantly, this includes strains of cells for which phenotypic differences remain largely uncharacterized. In

addition to experimental applications, current understanding of g-iDEP and its capabilities has also been advanced by the development of resolution theory for the technique (Chapter 5). This theory lays the groundwork for informed refinements to channel geometry and experimental design (Chapter 6). Already demonstrated herein was an iterative redesign of a sawtooth g-iDEP microchannel that yielded higher resolution and facilitated the simultaneous separation and concentration of antibiotic-resistant and antibiotic-susceptible *Staphylococcus epidermidis* (Chapter 7).

8.2 Future Directions

High-resolution analysis of bioparticles requires the use of selective techniques that lead to sample enrichment. Dielectrophoretic techniques such as g-iDEP are poised to open new frontiers in this field. However, certain challenges must be surmounted before wide-scale implementation for clinical or scientific applications is feasible. In many respects, these challenges can be categorized as either microfluidic engineering issues, or a lack of accurate, quantitative particle assessment. A chief engineering issue that needs to be addressed involves fine or high-resolution control of electric field generation. Designing and fabricating improved electrode or insulator geometry could go a long way toward improving resolution. Examples include maximizing the local restoring forces that produce capture zones, decreasing gate-to-gate variability, and decreasing dispersive effects such as transverse field heterogeneity and disruptive flow effects. Fortunately microfluidic engineering is a diverse and fast-moving field. Many tools and techniques already exist that could be brought to bear on improving g-iDEP designs. Further quantitative assessment of the biophysical and dielectrophoretic properties of analytes-of-interest would assist with the informed and intelligent design of

new g-iDEP microchannels, perhaps tailored for specific clinical tests or particle classes. These g-iDEP microchannels can be used in combination with finite-element multiphysics modeling software to facilitate rough but quantitative estimations of dielectrophoretic mobility for particle populations. Other work by the author (not represented within this dissertation) has contributed to the design of simplified microchannels that can be used to determine the dielectrophoretic mobility of particles. Using approaches such as these, it's easy to envision an iterative process of channel design that yields both an improved understanding of the dielectrophoretic behavior of particles as well as improved channel design for future separations. This work lays a foundation for quantitative g-IDEP which will enable the design of new and improved technology.

It's easy to envision other improvements and extensions of g-iDEP methodology. These could include (but are not limited to) addressable outlets for sample diversion and recovery, parallelization for high-throughput screening and analysis, and multiplexing with traditional analytical techniques for high-fidelity quantitation.

8.3 Summary

The work presented in this dissertation contributes to a better understanding of the scope and capabilities of g-iDEP for bioparticle separation and characterization. These results bear significant implications for the future of analytics and diagnostics. Incorporating g-iDEP channels into micro-total-analysis systems could facilitate high-resolution separation of analytes spanning the entire diversity of the microbiological world. This technology is conducive to the production of low-cost, portable devices. With accessible and widespread capability to separate similar analytes,

one can envision the application of these microchannel devices to studies in antibiotic resistance, vaccine development, and diagnostics in health and nutrition. It is even conceivable to assess the epidemiology of human disease in near real-time and on an individual basis, rather than waiting to assess outbreaks and progress. As g-iDEP continues to gain momentum, its potential in other fields beyond healthcare will be elucidated, including possibilities for environmental monitoring, bioengineering, and forensics.

REFERENCES

CHAPTER 1

[1] Bianconi, E., Piovesan, A., Facchin, F., Beraudi, A., Casadei, R., Frabetti, F., Vitale, L., Pelleri, M. C., Tassani, S., Piva, F., Perez-Amodio, S., Strippoli, P., Canaider, S., *Ann Hum Biol* 2013, *40*, 463-471.

[2] Sherwood, L., *Human Physiology: From Cells to Systems*, Cengage Learning 2008.

[3] Wintrobe, M. M., Greer, J. P., *Wintrobe's Clinical Hematology*, Wolters Kluwer Health/Lippincott Williams & Wilkins 2009.

[4] Hooper, L. V., Gordon, J. I., *Science* 2001, *292*, 1115-1118.

[5] Kau, A. L., Ahern, P. P., Griffin, N. W., Goodman, A. L., Gordon, J. I., *Nature* 2011, *474*, 327-336.

[6] Eloe-Fadrosh, E. A., Rasko, D. A., *Annual review of medicine* 2013, *64*, 145-163.

[7] Grice, E. A., Segre, J. A., *Nature reviews. Microbiology* 2011, *9*, 244-253.

[8] Toner, M., Irimia, D., *Annual Review of Biomedical Engineering* 2005, *7*, 77-103.

[9] Black, J. G., *Microbiology: principles and applications*, Prentice Hall 1996.

[10] Staton, S. J. R., Chen, K. P., Taylor, T. J., Pacheco, J. R., Hayes, M. A., *Electrophoresis* 2010, *31*, 3634-3641.

[11] Weston, A. D., Hood, L., *Journal of Proteome Research* 2004, *3*, 179-196.

[12] Anderson, N. L., Anderson, N. G., *Mol. Cell. Proteomics* 2002, *1*, 845-867.

[13] Collins, F. S., Lander, E. S., Rogers, J., Waterston, R. H., Int Human Genome Sequencing, C., *Nature* 2004, *431*, 931-945.

[14] Guarner, F., Malagelada, J. R., *Lancet* 2003, *361*, 512-519.

[15] Hooper, L. V., Gordon, J. I., *Science* 2001, *292*, 1115-1118.

[16] Giddings, J. C., *Unified Separation Science*, Wiley-Interscience 1991.

[17] Sameiro, M., Goncalves, T., *Chem. Rev.* 2009, *109*, 190-212.

[18] Pethig, R., *Biomicrofluidics* 2010, *4*.

[19] Pohl, H. A., *Dielectrophoresis: The Behavior of Neutral Matter in Nonuniform Electric Fields*, Cambridge University Press 1978.

[20] Gagnon, Z. R., *Electrophoresis* 2011, *32*, 2466-2487.

[21] Yang, L., *Analytical Letters* 2012.

[22] Srivastava, S. K., Gencoglu, A., Minerick, A. R., *Analytical and Bioanalytical Chemistry* 2011, *399*, 301-321.

[23] Çetin, B., Li, D., *Electrophoresis* 2011, *32*, 2410-2427.

[24] Suehiro, J., Zhou, G., Imamura, M., Hara, M., *Ieee Transactions on Industry Applications* 2003, pp. 1514-1521.

[25] Ying, L., White, S., Bruckbauer, A., Meadows, L., Korchev, Y., Klenerman, D., *Biophysical Journal* 2004, *86*, 1018-1027.

[26] Kang, Y., Li, D., Kalams, S. A., Eid, J. E., *Biomed Microdevices* 2007, *10*, 243-249.

[27] Zhu, J., Tzeng, T.-R. J., Hu, G., Xuan, X., *Microfluidics and Nanofluidics* 2009, *7*, 751-756.

[28] Pysher, M. D., Hayes, M. A., *Analytical Chemistry* 2007, *79*, 4552-4557.

CHAPTER 2

[1] Chen, W. K., *The Electrical Engineering Handbook*, Elsevier Science 2004, p. 486.

[2] Pohl, H. A., *Dielectrophoresis: The Behavior of Neutral Matter in Nonuniform Electric Fields*, Cambridge University Press 1978.

[3] Ida, N., *Engineering Electromagnetics*, Springer International Publishing 2015, p. 96.

[4] Garfin, D. E., Ahuja, S., *Handbook of Isoelectric Focusing and Proteomics*, Elsevier Academic Press 2005, pp. 14-15.

[5] Pethig, R., *Biomicrofluidics* 2010, *4*, 022811.

[6] Jones, T. B., *Electromechanics of Particles*, Cambridge University Press 2005.

[7] Sancho, M., Martínez, G., Martin, C., *Journal of Electrostatics* 2003, *57*, 143-156.

[8] Vrinceanu, D., Gheorghiu, E., *Bioelectrochemistry and bioenergetics* 1996, *40*, 167-170.

[9] Sukhorukov, V. L., Meedt, G., Kurschner, M., Zimmermann, U., *Journal of Electrostatics* 2001, *50*, 191-204.

[10] Huang, Y., Holzel, R., Pethig, R., Wang, X. B., *Physics in Medicine and Biology* 1992, *37*, 1499-1517.

[11] Pohl, H. A., Hawk, I., *Science* 1966, *152*, 647-649.

[12] Pohl, H. A., Crane, J. S., *Biophysical Journal* 1971, *11*, 711-727.

[13] Crane, J. S., Pohl, H. A., *Journal of the Electrochemical Society* 1968, *115*, 584-586.

[14] Mack, C., *Fundamental Principles of Optical Lithography*, John Wiley & Sons 2011.

[15] Pethig, R., Huang, Y., Wang, X. B., *Journal of Physics D: ...* 1992.

[16] Price, J. A., Burt, J. P., Pethig, R., *Biochimica et biophysica acta* 1988, *964*, 221-230.

[17] Becker, F., Wang, X., *Journal of Physics D: Applied Physics* 1994.

[18] Washizu, M., Nanba, T., Masuda, S., *Ieee Transactions on Industry Applications* 1990, *26*, 352-358.

[19] Washizu, M., *Journal of Electrostatics* 1993, *29*, 177-188.

[20] Huang, Y., Pethig, R., *Measurement Science and Technology* 1991, *2*, 1142.

[21] Hoettges, K. F., Hughes, M. P., Cotton, A., Hopkins, N. A., McDonnell, M. B., *IEEE engineering in medicine and biology magazine : the quarterly magazine of the Engineering in Medicine & Biology Society* 2003, *22*, 68-74.

[22] Gonzalez, C. F., Remcho, V. T., *Journal of Chromatography A* 2009, *1216*, 9063-9070.

[23] Masuda, S., Washizu, M., Nanba, T., *Ieee Transactions on Industry Applications* 1989, *25*, 732-737.

[24] Chou, C. F., Tegenfeldt, J. O., Bakajin, O., Chan, S. S., Cox, E. C., Darnton, N., Duke, T., Austin, R. H., *Biophysical Journal* 2002, *83*, 2170-2179.

[25] Cummings, E., Singh, A., *Analytical Chemistry* 2003, *75*, 4724-4731.

[26] Lapizco-Encinas, B., Simmons, B., Cummings, E., Fintschenko, Y., *Electrophoresis* 2004, *25*, 1695-1704.

[27] Lapizco-Encinas, B., Simmons, B., Cummings, E., Fintschenko, Y., *Analytical Chemistry* 2004, *76*, 1571-1579.

[28] Suehiro, J., Zhou, G., Imamura, M., Hara, M., *Ieee Transactions on Industry Applications* 2003, pp. 1514-1521.

[29] Ying, L., White, S., Bruckbauer, A., Meadows, L., Korchev, Y., Klenerman, D., *Biophysical Journal* 2004, *86*, 1018-1027.

[30] Kang, Y., Li, D., Kalams, S. A., Eid, J. E., *Biomed Microdevices* 2008, *10*, 243-249.

[31] Zhu, J., Tzeng, T.-R. J., Hu, G., Xuan, X., *Microfluidics and Nanofluidics* 2009, *7*, 751-756.

[32] Srivastava, S. K., Baylon-Cardiel, J. L., Lapizco-Encinas, B. H., Minerick, A. R., *Journal of Chromatography A* 2011, *1218*, 1780-1789.

[33] Staton, S. J. R., Chen, K. P., Taylor, T. J., Pacheco, J. R., Hayes, M. A., *Electrophoresis* 2010, *31*, 3634-3641.

[34] Jones, P. V., Staton, S. J. R., Hayes, M. A., *Analytical and Bioanalytical Chemistry* 2011, *401*, 2103-2111.

[35] Staton, S. J. R., Jones, P. V., Ku, G., Gilman, S. D., Kheterpal, I., Hayes, M. A., *Analyst* 2012, *137*, 3227.

[36] Pysher, M. D., Hayes, M. A., *Analytical Chemistry* 2007, *79*, 4552-4557.

[37] Jones, P. V., DeMichele, A. F., Kemp, L., Hayes, M. A., *Analytical and Bioanalytical Chemistry* 2014, *406*, 183-192.

CHAPTER 3

[1] Sherwood, L., *Human Physiology: From Cells to Systems 7th Ed.,* Brooks/Cole, Belmont 2010.

[2] Zuckerman, K. S., *Cecil Medicine 23rd Ed.,* Saunders, Philadelphia 2007.

[3] Greer, J. P., Foerster, J., Rodgers, G. M., Paraskevas, F., Glade, B., Arber, D. A., Means, R. T. (ed), *Wintrobe's Clinical Hematology 12th Ed.,* Lippincott Williams & Wilkins, Philadelphia 2008.

[4] Toner, M., Irimia, D., *Annu. Rev. Biomed. Eng.* 2005, *7*, 77–103.

[5] Meighan, M. M., Staton, S. J. R., Hayes, M. A. *Electrophoresis* 2009, *30*, 852–865.

[6] Cabrera, C., Yager, P., *Electrophoresis* 2001, *22*, 355–362.

[7] Pysher, M. D., Hayes, M. A., *Anal. Chem.* 2007, *79*, 4552–4557.

[8] Srivastava, S. K., Daggolu, P. R., Burgess, S. C., Minerick, A. R., *Electrophoresis* 2008, *29*, 5033–5046.

[9] Lapizco-Encinas, B., Simmons, B., Cummings, E., Fintschenko, Y., *Anal. Chem.* 2004, *76*, 1571–1579.

[10] Lapizco-Encinas, B. H., Rito-Palomares, M., *Electrophoresis* 2007, *28*, 4521–4538.

[11] West, J., Becker, M., Tombrink, S., Manz, A., *Anal. Chem.* 2008, *80*, 4403–4419.

[12] Gascoyne, P., Satayavivad, J., Ruchirawat, M., *Acta Trop.* 2004, *89*, 357–369.

[13] Baylon-Cardiel, J. L., Lapizco-Encinas, B. H., Reyes-Betanzo, C., Chavez-Santoscoy, A. V., Martinez-Chapa, S. O. *Lab Chip* 2009, *9*, 2896–2901.

[14] Gagnon, Z., Gordon, J., Sengupta, S., Chang, H. C., *Electrophoresis* 2008, *29*, 2272–2279.

[15] Mack, C., *Fundamental Principles of Optical Lithography: The Science of Microfabrication,* Wiley, Chichester 2007.

[16] Staton, S. J. R., Chen, K. P., Taylor, T. J., Pacheco, J. R., Hayes, M. A., *Electrophoresis* 2010, *31*, 3634–3641.

[17] Turgeon, M. L., *Clinical Hematology: Theory and Procedures 4th Ed.,* Lippincott Williams & Wilkins, Philadelphia 2004.

[18] Hendry, E., *Clin. Chem.* 1961, *7*, 156–164.

[19] Pohl, H. A., *Dielectrophoresis: The behavior of neutral matter in nonuniform electric fields,* Cambridge University Press, Cambridge 1978.

[20] Jan, K., Chien, S., *J. Gen. Physiol.* 1973, *61*, 638–654.

[21] Cummings, E. B., Griffiths, S. K., Nilson, R. H., Paul, P. H., *Anal. Chem.* 2000, *72*, 2526–2532.

[22] Chen, K. P., Pacheco, J. R., Hayes, M. A., Staton, S. J. R., *Electrophoresis* 2009, *30*, 1441–1448.

[23] Pethig, R., *Biomicrofluidics* 2010, *4*, 022811.

[24] Minerick, A., Zhou, R., Takhistov, P., Chang, H., *Electrophoresis* 2003, *24*, 3703–3717.

[25] Wong, P., Wang, T. H., Deval, J. H., Ho, C. M., *IEEE/ASME Trans. on Mechatronics* 2004, *9*, 366–376.

[26] Mohandas, N., Gallagher, P. G., *Blood* 2008, *112*, 3939–3948.

[27] Grushka, E., McCormick, R. M., Kirkland, J. J., *Anal. Chem.* 1989, *61*, 241–246.

[28] Tang, G. Y., Yan, D. G., Yang, C., Gong, H. Q., Chai, C. J., Lam, Y. C., J. *Phys.: Conf. Ser.* 2006, *34*, 925–930.

[29] Martinez-Lopez, J. I., Moncada-Hernandez, H., Baylon-Cardiel, J. L., Martinez-Chapa, S. O., Rito-Palomares, M., Lapizco-Encinas, B. H., *Anal. Bioanal. Chem.* 2009, *394*, 293–302.

[30] Davalos, R. V., McGraw, G. J., Wallow, T. I., Morales, A. M., Krafcik, K. L., Fintschenko, Y., Cummings, E. B., Simmons, B. A., *Anal. Bioanal. Chem*. 2008, *390*, 847–855.

[31] Picou, R., Moses, J. P., Wellman, A. D., Kheterpal, I., Gilman, S. D. *Analyst* 2010, *135*, 1631–1635.

CHAPTER 4

[1] Whitman, W. B., Coleman, D. C., Wiebe, W. J., *Proc. Natl. Acad. Sci. U. S. A.* 1998, *95*, 6578-6583.

[2] Hooper, L. V., Gordon, J. I., *Science* 2001, *292*, 1115-1118.

[3] Agata, E. M. C. D., Gautam, S., Green, W. K., Tang, Y.-W., *Clinical Infectious Diseases* 2002, *34*, 167-172.

[4] Benjamin, R. J., Wagner, S. J., *Transfusion* 2007, *47*, 1381-1389.

[5] Scallan, E. G., P. M.; Angulo, F. J.; Tauxe, R. V.; Hoekstra, R. M., *Emerging Infectious Diseases* 2011, *17*, 16-22.

[6] Black, J. G., *Microbiology: principles and applications*, Prentice Hall 1996.

[7] Tenover, F. C., in: Bush, K. (Ed.), *Antimicrobial Therapeutics Reviews* 2010, pp. 70-80.

[8] Suehiro, J., Noutomi, D., Shutou, M., Hara, M., *Journal of Electrostatics* 2003, *58*, 229-246.

[9] Gascoyne, P. R. C., Noshari, J., Becker, F. F., Pethig, R., *IEEE Transactions on Industry Applications* 1994, *30*, 829-834.

[10] Huang, Y., Wang, X. B., Becker, F. F., Gascoyne, P. R. C., *Biochimica et Biophysica Acta-Biomembranes* 1996, *1282*, 76-84.

[11] Becker, F. F., Wang, X. B., Huang, Y., Pethig, R., Vykoukal, J., Gascoyne, P. R. C., *Journal of Physics D-Applied Physics* 1994, *27*, 2659-2662.

[12] Becker, F. F., Wang, X. B., Huang, Y., Pethig, R., Vykoukal, J., Gascoyne, P. R. C., *Proceedings of the National Academy of Sciences of the United States of America* 1995, *92*, 860-864.

[13] Burt, J. P. H., Pethig, R., Gascoyne, P. R. C., Becker, F. F., *Biochimica Et Biophysica Acta* 1990, *1034*, 93-101.

[14] Wang, X. B., Huang, Y., Gascoyne, P. R. C., Becker, F. F., Holzel, R., Pethig, R., *Biochimica et Biophysica Acta-Biomembranes* 1994, *1193*, 330-344.

[15] Petr, J., Maier, V., *Trac-Trends in Analytical Chemistry* 2012, *31*, 9-22.

[16] Armstrong, D. W., Schulte, G., Schneiderheinze, J. M., Westenberg, D. J., *Anal. Chem.* 1999, *71*, 5465-5469.

[17] Hsiao, A. P., Barbee, K. D., Huang, X., 2010, 77590W-77590W.

[18] Preira, P., Grandne, V., Forel, J. M., Gabriele, S., Camara, M., Theodoly, O., *Lab on a Chip* 2013, *13*, 161-170.

[19] Phillips, J. A., Xu, Y., Xia, Z., Fan, Z. H., Tan, W. H., *Anal. Chem.* 2009, *81*, 1033-1039.

[20] Olitzki, L., *Journal of Immunology* 1932, *22*, 251-256.

[21] Jones, P. V., Staton, S. J. R., Hayes, M. A., *Analytical and Bioanalytical Chemistry* 2011, *401*, 2103-2111.

[22] Staton, S. J. R., Jones, P. V., Ku, G., Gilman, S. D., Kheterpal, I., Hayes, M. A., *Analyst* 2012, *137*, 3227-3229.

[23] Chen, K. P., Pacheco, J. R., Hayes, M. A., Staton, S. J. R., *Electrophoresis* 2009, *30*, 1441-1448.

[24] Pysher, M. D., Hayes, M. A., *Anal. Chem.* 2007, *79*, 4552-4557.

[25] Hamadi, F., Latrache, H., Zahir, H., Elghmari, A., Timinouni, M., Ellouali, M., *Brazilian Journal of Microbiology* 2008, *39*, 10-15.

[26] Amory, D. E., Mozes, N., Hermesse, M. P., Leonard, A. J., Rouxhet, P. G., *Fems Microbiology Letters* 1988, *49*, 107-110.

[27] El Ghmari, A., Latrache, H., Hamadi, F., El Louali, M., El Bouadili, A., Hakkou, A., Bourlioux, P., *Microbiologica* 2002, *25*, 173-178.

[28] Latrache, H., Mozes, N., Pelletier, C., Bourlioux, P., *Colloids and Surfaces B: Biointerfaces* 1994, *2*, 47-56.

[29] Lytle, D. A., Rice, E. W., Johnson, C. H., Fox, K. R., *Applied and Environmental Microbiology* 1999, *65*, 3222-3225.

[30] Pethig, R., *Biomicrofluidics* 2010, *4*.

[31] Castellarnau, M., Errachid, A., Madrid, C., Juarez, A., Samitier, J., *Biophysical Journal* 2006, *91*, 3937-3945.

[32] Weiss, N. G., Jones, P. V., Mahanti, P., Chen, K. P., Taylor, T. J., Hayes, M. A., *Electrophoresis* 2011, *32*, 2292-2297.

CHAPTER 5

[1] Giddings, J. C., Eyring, H., *Journal of Physical Chemistry* 1955, *59*, 416-421.

[2] Jorgenson, J. W., Lukacs, K. D., *Anal. Chem.* 1981, *53*, 1298-1302.

[3] Kolin, A., *Journal of Chemical Physics* 1954, *22*, 1628-1629.

[4] Brakke, M. K., *Journal Of The American Chemical Society* 1951, *73*, 1847-1848.

[5] Koegler, W. S., Ivory, C. F., *Journal of Chromatography A* 1996, *726*, 229-236.

[6] Keller, R. A., Giddings, J. C., *Journal of Chromatography* 1960, *3*, 205-220.

[7] Giddings, J. C., *Analytical Chemistry* 1963, *35*, 1999-2002.

[8] Foret, F., Fanali, S., Ossicini, L., Bocek, P., *J. Chromatogr.* 1989, *470*, 299-308.

[9] Giddings, J. C., Dahlgren, K., *Separation Science* 1971, *6*, 345-356.

[10] Kelly, R. T., Woolley, A. T., *Journal of Separation Science* 2005, *28*, 1985-1993.

[11] Pysher, M. D., Hayes, M. A., *Analytical Chemistry* 2007, *79*, 4552-4557.

[12] Staton, S. J. R., Chen, K. P., Taylor, T. J., Pacheco, J. R., Hayes, M. A., *Electrophoresis* 2010, *31*, 3634-3641.

[13] Jones, P. V., Staton, S. J. R., Hayes, M. A., *Analytical and Bioanalytical Chemistry* 2011, *401*, 2103-2111.

[14] Staton, S. J. R., Jones, P. V., Ku, G., Gilman, S. D., Kheterpal, I., Hayes, M. A., *Analyst* 2012, *137*, 3227-3229.

[15] Jones, P. V., DeMichele, A. F., Kemp, L., Hayes, M. A., *Analytical and Bioanalytical Chemistry* 2014, *406*, 183-192.

[16] Jones, T. B., *Electromechanics of Particles*, Cambridge University Press 2005.

[17] Weiss, N. G., Jones, P. V., Mahanti, P., Chen, K. P., Taylor, T. J., Hayes, M. A., *Electrophoresis* 2011, *32*, 2292-2297.

[18] Giddings, J. C., *Unified Separation Science*, John Wiley and Sons, New York 1991.

[19] Giddings, J. C., *Dynamics of Chromatography*, M. Dekker, New York 1965.

[20] Jacobson, S. C., Culbertson, C. T., Daler, J. E., Ramsey, J. M., *Anal. Chem.* 1998, *70*, 3476-3480.

[21] Kang, K. H., Xuan, X. C., Kang, Y. J., Li, D. Q., *Journal Of Applied Physics* 2006, *99*, art. numb. 064702.

[22] Tolley, H. D., Wang, Q. G., LeFebre, D. A., Lee, M. L., *Analytical Chemistry* 2002, *74*, 4456-4463.

[23] Shannon, C. E., *Proceedings of the Institute of Radio Engineers* 1949, *37*, 10-21.

[24] Kenyon, S. M., Keebaugh, M. W., Hayes, M. A., *Electrophoresis* 2014, *35*, 2551-2559.

[25] LaLonde, A., Gencoglu, A., Romero-Creel, M. F., Koppula, K. S., Lapizco-Encinas, B. H., *Journal Of Chromatography A* 2014, *1344*, 99-108.

[26] Liao, K. T., Tsegaye, M., Chaurey, V., Chou, C. F., Swami, N. S., *Electrophoresis* 2012, *33*, 1958-1966.

[27] Braff, W. A., Willner, D., Hugenholtz, P., Rabaey, K., Buie, C. R., *Plos One* 2013, *8*, art. numb. e76751.

CHAPTER 6

[1] Giddings, J. C., Dahlgren, K., *Separation Science* 1971, *6*, 345-356.

[2] Giddings, J. C., *Unified Separation Science*, Wiley-Interscience 1991.

[3] Jones, P. V., Hayes, M. A., *Electrophoresis* 2015, Accepted for publication.

[4] Chou, C., Tegenfeldt, J., Bakajin, O., Chan, S., Cox, E., Darnton, N., Duke, T., Austin, R., *Biophysical Journal* 2002, *83*, 2170-2179.

[5] Cummings, E., Singh, A., *Analytical Chemistry* 2003, *75*, 4724-4731.

[6] Chen, K. P., Pacheco, J. R., Hayes, M. A., Staton, S. J. R., *Electrophoresis* 2009, *30*, 1441-1448.

[7] Weiss, N. G., Jones, P. V., Mahanti, P., Chen, K. P., Taylor, T. J., Hayes, M. A., *Electrophoresis* 2011, n/a-n/a.

[8] Humble, P. H., Kelly, R. T., Woolley, A. T., Tolley, H. D., Lee, M. L., *Analytical Chemistry* 2004, *76*, 5641-5648.

[9] Jones, P. V., Staton, S. J. R., Hayes, M. A., *Analytical and Bioanalytical Chemistry* 2011, *401*, 2103-2111.

[10] Staton, S. J. R., Jones, P. V., Ku, G., Gilman, S. D., Kheterpal, I., Hayes, M. A., *Analyst* 2012, *137*, 3227.

[11] Jones, P. V., DeMichele, A. F., Kemp, L., Hayes, M. A., *Analytical and Bioanalytical Chemistry* 2014, *406*, 183-192.

CHAPTER 7

[1] Ochman, H., Lawrence, J. G., Groisman, E. A., *Nature* 2000, *405*, 299-304.

[2] Malachowa, N., DeLeo, F. R., *Cellular and molecular life sciences : CMLS* 2010, *67*, 3057-3071.

[3] Nelson, M. L., Dinardo, A., Hochberg, J., Armelagos, G. J., *American Journal of Physical Anthropology* 2010, *143*, 151-154.

[4] Abraham, E. P., Chain, E., *Nature* 1940, *146*, 837-837.

[5] Aminov, R. I., Mackie, R. I., *FEMS microbiology letters* 2007, *271*, 147-161.

[6] Cosgrove, S. E., *Clinical Infectious Diseases* 2006, *42*, S82-S89.

[7] Division of Healthcare Quality Promotion, National Center for HIV/AIDS Viral Hepatitis STD and TB Prevention, National Center for Immunization and Respiratory Diseases (NCIRD), Atlanta, GA 2013.

[8] Davies, J., Davies, D., *Microbiology and Molecular Biology Reviews* 2010, *74*, 417-433.

[9] Kloos, W. E., Musselwhite, M. S., *Applied Microbiology* 1975, *30*, 381-395.

[10] Grice, E. A., Segre, J. A., *Nature reviews. Microbiology* 2011, *9*, 244-253.

[11] Vuong, C., Otto, M., *Microbes and infection / Institut Pasteur* 2002, *4*, 481-489.

[12] Uçkay, I., Pittet, D., Vaudaux, P., Sax, H., Lew, D., Waldvogel, F., *Annals of Medicine* 2009, *41*, 109-119.

[13] Otto, M., *Nature reviews. Microbiology* 2009, *7*, 555-567.

[14] Wright, G. D., *Chemical communications (Cambridge, England)* 2011, *47*, 4055-4061.

[15] Miller, G. H., Sabatelli, F. J., Hare, R. S., Glupczynski, Y., Mackey, P., Shlaes, D., Shimizu, K., Shaw, K. J., Bauernfeind, A., Schweighart, S., Shannon, K., Patzer, J., Molinari, G., Schito, G. C., GomezLus, R., GomezLus, S., Ferreira, H., Sousa, J. C., Vaz, M., Collatz, E., Bismuth, R., Lambert, T., Courvalin, P., Minozzi, C., Klugman, K., Bilgeri, Y., Giamarellou, H., Petrikkos, G., Akalin, H., Gur, D., Woloj, M., Rossi, A., Casellas, J., Tokumoto, M., Couto, E., Juliet, C., Pinto, M. E., Zemelman, R., Pedreira, W., Fernandez, M., Leal, I., Guzman, M., Murillo, J., Isturiz, P., Merentes, A., Bremner, A., Ho, B., Mayer, K., Ellal, J., Fu, W., Zhu, D., Dornbusch, K., Goransson, E., *Clinical Infectious Diseases* 1997, *24*, S46-S62.

[16] Davison, J., *Plasmid* 1999, *42*, 73-91.

[17] Kruse, H., Sørum, H., *Applied and environmental microbiology* 1994, *60*, 4015-4021.

[18] Huang, L. R., Cox, E. C., Austin, R. H., Sturm, J. C., 2004, *304*, 987-990.

[19] Neirinck, B., Van der Biest, O., Vleugels, J., *Journal Of Physical Chemistry B* 2013, *117*, 1516-1526.

[20] Šalplachta, J., Kubesová, A., Horká, M., *Proteomics* 2012, *12*, 2927-2936.

[21] Gagnon, Z. R., *Electrophoresis* 2011, *32*, 2466-2487.

[22] Demircan, Y., Özgür, E., Külah, H., *Electrophoresis* 2013, *34*, 1008-1027.

[23] Çetin, B., Li, D., *Electrophoresis* 2011, *32*, 2410-2427.

[24] Yang, L., *Analytical Letters* 2012.

[25] Pysher, M. D., Hayes, M. A., *Analytical Chemistry* 2007, *79*, 4552-4557.

[26] Staton, S. J. R., Chen, K. P., Taylor, T. J., Pacheco, J. R., Hayes, M. A., *Electrophoresis* 2010, *31*, 3634-3641.

[27] Jones, P. V., Staton, S. J. R., Hayes, M. A., *Analytical and Bioanalytical Chemistry* 2011, *401*, 2103-2111.

[28] Staton, S. J. R., Jones, P. V., Ku, G., Gilman, S. D., Kheterpal, I., Hayes, M. A., *Analyst* 2012, *137*, 3227-3229.

[29] Jones, P. V., DeMichele, A. F., Kemp, L., Hayes, M. A., *Analytical and Bioanalytical Chemistry* 2014, *406*, 183-192.

[30] Jorgensen, J. H., Ferraro, M. J., *Clinical Infectious Diseases* 2009, *49*, 1749-1755.

[31] Ibrahim, E. H., Sherman, G., Ward, S., Fraser, V. J., Kollef, M. H., *Chest* 2000, *118*, 146-155.

[32] Iregui, M., Ward, S., Sherman, G., Fraser, V. J., Kollef, M. H., *Chest* 2002, *122*, 262-268.

[33] Lodise, T. P., McKinnon, P. S., Swiderski, L., Rybak, M. J., *Clinical Infectious Diseases* 2003, *36*, 1418-1423.

[34] Jones, P. V., Hayes, M. A., *Electrophoresis* 2015, Accepted for publication.

[35] Govindarajan, S., Nevo-Dinur, K., Amster-Choder, O., *FEMS microbiology reviews* 2012, *36*, 1005-1022.

[36] Sonohara, R., Muramatsu, N., Ohshima, H., Kondo, T., *Biophysical chemistry* 1995, *55*, 273-277.

[37] Le Goffic, F., Martel, A., Moreau, N., Capmau, M. L., Soussy, C. J., Duval, J., *Antimicrobial Agents and Chemotherapy* 1977, *12*, 26-30.

[38] Horká, M., Kubícek, O., Růzicka, F., Holá, V., Malinovská, I., Slais, K., *Journal of Chromatography A* 2007, *1155*, 164-171.

[39] Williams, J. W., Northrop, D. B., *Biochemistry* 1976, *15*, 125-131.

[40] Castellarnau, M., Errachid, A., Madrid, C., Juarez, A., Samitier, J., *Biophysical Journal* 2006, *91*, 3937-

APPENDIX A

MATHEMATICAL MODELING

Finite-element multiphysics simulation software (COMSOL Multiphyscis) was used to model electric field characteristics within g-iDEP microchannels. These models were used to create graphical representations of the distribution of the electric field both at individual gates and across larger channel segments, as shown in Chapters 3 and 6. In some cases, modeled numerical values were used to calculate analyte mobilities, as was done in Chapters 4 and 7. Centerline values of electric field parameters were also plotted as shown in Chapter 6. These values were used in efforts to refine the progression of gate pitch along a sawtooth g-iDEP microchannel.

In order to create a simulation, a properly-scaled version of 2D channel geometry was first created using AutoCAD software and exported as a Drawing Interchange File (DXF file format). This file was then imported into COMSOL. Using a 2D approximation simplifies the calculations and significantly reduces computation time. Since the channels are relatively shallow, compared to other dimensions, the electric potential is presumed to vary only slightly across the channel depth. The software contains drawing tools which can be used to adjust the geometry. Specifically, the *fillet* tool was used to slightly round the vertices of the sawtooth shapes, approximating the real-world shape of the PDMS casts.

A variety of modules are available for this specific software (COMSOL Multiphysics), each tailored for certain types of physics modeling. For the work described in this dissertation, the *Electric Currents* module was used. Within this module, geometric boundaries are set as insulators by default. This definition assumes that no current flows across the boundaries. The user may define boundary segments that act as conductors, and specify electric potential at these boundaries. Using the built-in materials

library, insulator boundaries were defined as silica glass. The boundaries at each end of the channel were set as copper metal, and the bounded domain was assigned as water. After making these assignments, the estimated conductivity and permittivity of the aqueous medium were entered to reflect the properties of the buffer used in experiments. Another input variable was the applied potential. The conductive boundary representing the inlet of the microchannel was assigned as ground. The potential of the opposite conductive boundary was set at -100 to -3000 V, reflecting a variety of experimental conditions.

This software uses the finite element method to solve the boundary value problem for the underlying physics. The domain is subdivided into simpler parts using mesh generation. User-adjustable parameters allow fine-tuning of the mesh characteristics, with the goal of minimizing error and reducing noise in the results. For this work, a *free triangular* mesh was used. Beginning with COMSOL's *fine* resolution preset, empirical adjustments were made to the mesh structure. Small elements are desirable for accurate modeling, especially within narrow channel segments and regions near gates. However, a large number of elements increases computation time.

Results were computed using a *stationary* (rather than time-dependent) solution. Using these results, *2D plots*, *line charts*, and *numerical values* were obtained using expressions for $\boldsymbol{E}$, $\boldsymbol{\nabla}|\boldsymbol{E}|^2$, and e_c, as discussed in Chapters 3 through 7. Trapping conditions were modeled using an expression derived from Eq. 19 in Chapter 2 of this dissertation. In this case, μ_{EK} was estimated from experimentally-determined values and μ_{DEP} was estimated based on known particle and medium properties.

APPENDIX B

PUBLISHED PORTIONS

Selected portions of this dissertation were published in the journals referenced below. These published materials were included with the permission of all co-authors.

Chapter 3

Jones, P. V., Staton, S. J. R., Hayes, M. A., *Analytical and Bioanalytical Chemistry* 2011, *401*, 2103-2111.

Chapter 4

Jones, P. V., DeMichele, A. F., Kemp, L., Hayes, M. A., *Analytical and Bioanalytical Chemistry* 2014, *406*, 183-192.

Chapter 5

Jones, P. V., Hayes, M. A., *Electrophoresis* 2015, Accepted for publication.